Effects of mechano-electrical feedback on cardiac dynamics: Pro- and anti-arrhythmic effects during alternans

by

Azzam Hazim

A thesis submitted in partial fulfillment of the requirements for the degree of

Doctor of Philosophy

Department of Biomedical Engineering

University of Alberta

Abstract

Contraction of the heart has been shown to affect the propagation of action potential (AP). In fact, the electrical waves of the heart propagate through the cardiac tissue and initiate its contraction via excitation-contraction coupling (ECC) while contraction of the heart causes deformations in the cardiac tissue that feedback on the process of wave propagation and affect electrophysiological properties through the mechanism of the so-called mechano-electrical feedback (MEF). The effects of MEF on cardiac electrophysiology may have both anti-arrhythmic and arrhythmogenic actions, however, the underlying mechanisms remain to be completely understood. Moreover, very little work has been done to study the effects of MEF on cardiac alternans. The later is a disturbance in heart rhythm, that manifests as a sequence of alternating long and short AP duration (APD). The APD alternans is linked to the onset of lethal cardiac arrhythmias.

The focus of this thesis is to conduct a study on the effects of MEF on cardiac wave dynamics, particularly its effects on the dynamics of alternans, and to develop control algorithms to suppress alternans via MEF in real size of cardiac tissue. Therefore, in this thesis, which is based on computational study, electromechanical (EM) models that couple the cardiac excitation with the mechanical properties of the heart are used to perform numerical and theoretical investigations. The thesis contributions can be summarized as follows:

First, we show that the critical basic cycle length (BCL) corresponding to the onset of alternans along a one-dimensional (1D) cable of cardiac cells may be decreased in the presence of MEF. This antiarrhythmic effect of MEF close to the alternans

bifurcation is due to the stretch-activated current (I_{sac}), which is the main effect of MEF, that can modulate APDs in response to stretching. When studying the effects of MEF on the onset of alternans a restriction is put on the strength of I_{sac}, so that its effects on the velocity of the pulse wave can be neglected, and only a certain range of BCLs, that are closed to the critical BCL, is chosen.

Second, we show that MEF may play a role in arrhythmogenesis when a 1D cable is paced at a BCL, that is not very close to the critical BCL. It is illustrated that I_{sac} can increase the dispersion of repolarization via its influence on the dispersion of conduction velocity. In particular, it is shown that MEF can convert a spatially concordant alternans (SCA), where APDs alternate in phase along the tissue, into a spatially discordant alternans (SDA), which is more arrhythmogenic, where APDs alternate out of phase in different regions of tissue. In addition, it is shown that for some values of the I_{sac} model parameters, I_{sac} gives rise to a large spatial dispersion of repolarization that can result in blocking AP propagation.

Third, a control algorithm that combines the electrical pacing with the mechanical perturbation methods is developed. In this algorithm, the electrical pacing is realized by shortening or lengthening the BCL at the pacing site, and the novel mechanical perturbation strategy is realized by perturbing a small region within the heart tissue.

Finally, a novel theoretical framework of 2D iterative maps, that incorporate the effects of MEF, and numerical simulations are presented to demonstrate successful suppression of alternans in cardiac tissue of relevant size using the proposed control algorithm and employing a simple EM model, namely the Nash-Panfilov model and two realistic EM models.

In summary, in this thesis, the pro- and anti-arrhythmic effects of MEF during alternans are described and discussed, and a novel method that can manipulate MEF in order to suppress alternans is proposed, thus overcoming the limitations of tissue size that earlier alternans control methods have.

Preface

For all of the papers published and submitted, I was responsible for performing the problem analysis, numerical simulation and manuscript composition. Dr. Y. Belhamadia and Dr. S. Dubljevic were the supervisory authors and were involved with concept formation and manuscript composition.

Chapter 2 of this thesis has been published as A. Hazim, Y. Belhamadia and S. Dubljevic, "Effects of mechano-electrical feedback on the onset of alternans: A computational study," Chaos 29, 063126 (2019).

Chapter 3 of this thesis has been submitted for publication as A. Hazim, Y. Belhamadia and S. Dubljevic, "A simulation study of the role of mechanical deformation in arrhythmogenesis during cardiac alternans".

Chapter 4 of this thesis has been published as A. Hazim, Y. Belhamadia and S. Dubljevic, "Control of cardiac alternans in an electromechanical model of cardiac tissue," Computers in Biology and Medicine 63, 108 (2015).

Chapter 5 of this thesis has been published as A. Hazim, Y. Belhamadia and S. Dubljevic, "Mechanical perturbation control of cardiac alternans," Physical Rev E 97, 052407 (2018).

Acknowledgements

I would like to express my thanks to my supervisors Dr. Youssef Belhamadia and Dr. Stevan Dubljevic for all their guidance, patience, support, and for giving me the freedom to explore different research topics during my PhD studies. The many inspiring discussions I had with them over the years played an important role in shaping this research.

Special thanks also go to my committee members and examiners for their participation on my thesis and exam committees. They provided me insightful comments and suggestions. I am also grateful to my fellow colleagues at distributed parameter systems lab for their friendships and encouragement.

I would also like to acknowledge the financial support from the Heart and Stroke Foundation (HSF) of Canada Grant-in-Aid (GIA) and the Natural Sciences and Engineering Research Council (NSERC) of Canada.

Words cannot express how grateful I am to my family for their unconditional love and support.

Contents

List of Tables

List of Figures

List of Abbreviations

1D	one-dimensional
2D	two-dimensional
AP	action potential
APD	action potential duration
ATD	action tension duration
ATP	active tension peak
AV	atrioventricular
BCL	basic cycle length
CB	conduction block
CEC	coupled electromechanical cell
CV	conduction velocity
DI	diastolic interval
ECC	excitation-contraction coupling
ECG	electrocardiogram
EM	electromechanical
EMC	electromechanically concordant
EMD	electromechanically discordant
FOXNHS	FOX Niederer–Hunter–Smith
LR1	Luo–Rudy I
LR1NHS	Luo–Rudy I Niederer–Hunter–Smith
MEF	mechano-electric feedback
MR	Mooney–Rivlin
NP	Nash-Panfilov
NHS	Niederer–Hunter–Smith
ODE	ordinary differential equation
PCL	pacing cycle length
PS	pacing site
SA	sinoatrial
SACs	stretch-activated channels
SCA	spatially concordant alternans
SCD	sudden cardiac death
SDA	spatially discordant alternans
SVNP	smooth variant of the Nash-Panfilov
TWA	T-wave alternans
VF	ventricular fibrillation

Chapter 1

Introduction

1.1 Motivation

Irregular electrical waves of excitation in the heart may result in cardiac arrhythmias. Ventricular fibrillation (VF) [1, 2] is the most dangerous form of arrhythmias and is recognized as a major cause of sudden cardiac death (SCD) in the industrialized world. Electrical alternans [3] which is characterized by a periodic alternations in the action potential duration (APD), is an electrical instability in the heart. The APD alternans is believed to precede VF. It can be clinically detected as T-wave alternans (TWA) using an electrocardiogram, and is associated with increased risk of SCD [4].

Mechanical deformation of cardiac tissue induced by the contraction of the heart is shown to influence electrical activity of the heart. In fact, electrical waves propagate through cardiac tissue and initiate mechanical contraction via the phenomenon of excitation-contraction coupling (ECC) [5]. On the other hand, the deformation caused by contraction affects the electrical waves via the phenomenon of mechano-electrical feedback (MEF) [6, 7, 8, 9]. It has been shown that MEF can have both anti-arrhythmic and pro-arrhythmic effects [10, 11], however, the underlying mechanisms remain to be fully elucidated. In particular, the effects of MEF on the alternans is little studied in the literature, despite the fact that alternans have been associated with the onset of VF.

The focus of this thesis is to conduct a full study of the effects of MEF on the electrical activity of the heart, particularly its effects on cardiac alternans. This will help to explore the possibility of suppressing alternans via MEF in relevantly sized cardiac tissues in order to prevent VF and SCD.

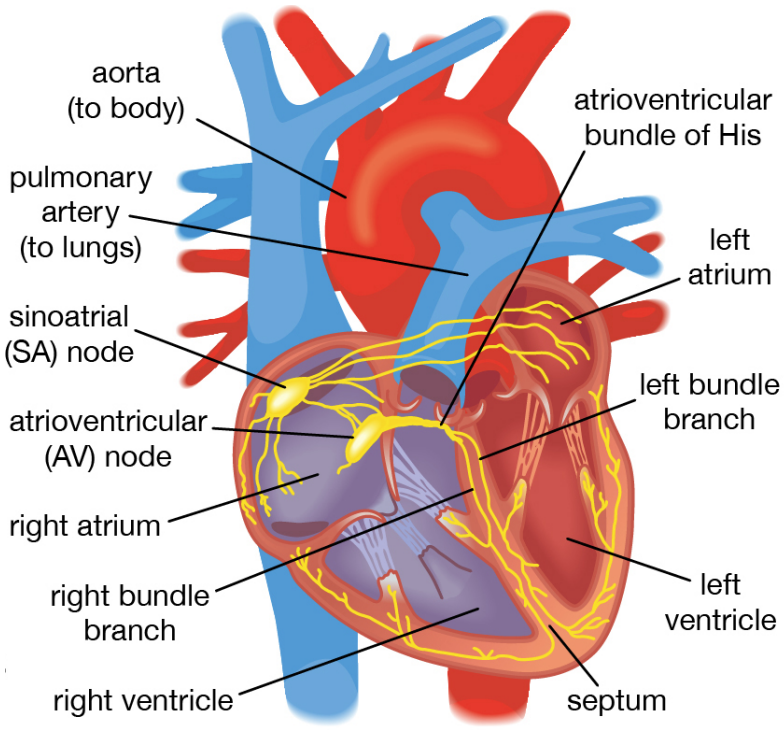

Figure 1.1: Electrical conduction system within the human heart. The elements of the conduction system that conduct the electrical wave, originating from AV node, and traveling through the tissue to the ventricles (from www.britannica.com/science/electrocardiography).

1.2 Background

In this chapter, we briefly discuss the anatomy and physiology of the heart, cardiac alternans, and at the end we describe mathematical equations that model the electrical excitation and mechanical contraction of the heart, used in this thesis.

1.2.1 The heart

The human heart is an organ which pumps blood throughout the body by rhythmic contractions of the muscles. Every day, the heart pumps approximately 7000 Litres of blood, and during a lifetime, the heart will contract over one billion times. The heart (Fig. 1.1) consists of two small, thin-walled upper chambers (left and right atria) divided by the interatrial septum, and two larger thick-walled lower chambers (the left and right ventricles) divided by the interventricular septum. The atria act as receiving chambers for blood entering the heart and contract to eject the blood

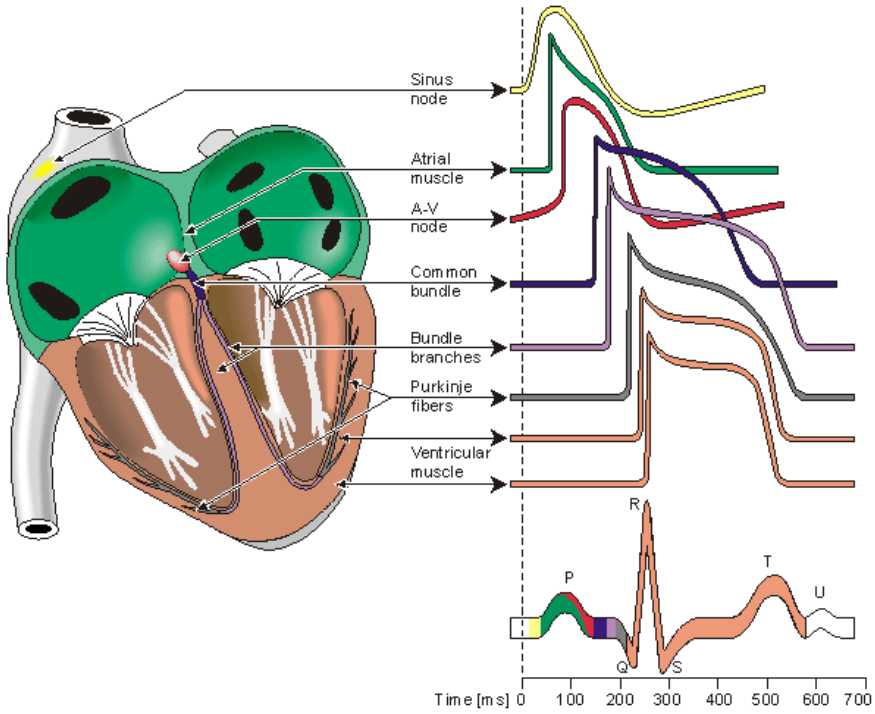

Figure 1.2: Schematic illustrations of action potentials measured at membrane of human myocytes. The action potentials vary in different regions as they move from the SA node, atrium, AV node, bundle of His, bundle branches, Purkinje fibers, to subendocardial and subepicardial ventricular myocardium (from http://www.bem.fi/book/index.htm).

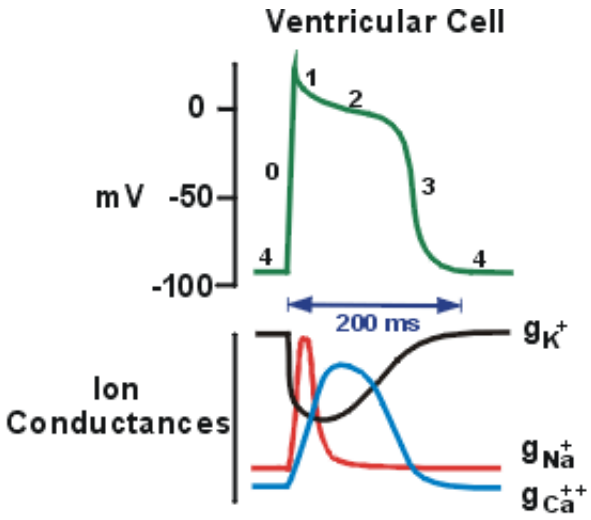

Figure 1.3: Ventricular action potential (top) and and the underlying ion conductances (bottom) (from www.cvpharmacology.com).

into the ventricles. The ventricles then pump the blood into the lungs or to the rest of the body.

The heart tissue is composed from excitable cardiac muscle cells which are connected electrically via gap junctions. The cardiomyocytes are excitable that cause the cells to contract after excitation. Normally, the electrical impulse begins in the sinoatrial (SA) node, which consists of a group of cells, located in the right atrium (Fig. 1.1) and is known as the pacemaker of the heart (see [12]). The impulse travels from the SA node and right atrium to the left atrium through the interatrial septum and then to the atrioventricular (AV) node in approximately 50 ms. From the AV node, the impulse propagates via the bundle of His and bundle branches to the Purkinje fibres. Finally, the electrical impulse spreads throughout ventricular myocardium via the Purkinje fibres. Propagation speed within the ventricular region is relatively high compared to velocity through the AV node. This causes the ventricles to contract in unison and pump the blood to the pulmonary and systemic circulations. The shape of the action potential (AP) depends on the cell type, and therefore, various APs are generated regionally (Fig. 1.2). The AP profile is governed by the complex interaction of ion fluxes through ion channels, some of which are voltage-gated. Along with Ions channels, pumps and exchangers also mediate the movement of ions across the cell membrane, see [37]. The ions are constantly moving into or out the cell mem-

brane, thus generating depolarizing and repolarizing currents. When an electrical stimulus, exceeding a certain threshold ($\approx$ 60 mV), is applied to the myocardium, a change in the transmembrane potential, which is the electrical potential difference between the inside and outside of the cell membrane, is observed (depolarized). This rapid depolarization, referred to as the phase 0 (Fig. 1.3), is caused by a rapid influx of positively charged sodium (Na^+) ions that raises the membrane potential to approximately +30 mV. This is followed by a brief transient increase in potassium (K^+) and a decrease of Na^+ ion conductances resulting in early rapid repolarization (Phase 1). Phase 2 which is the plateau phase of the cardiac AP comes next. In this phase, the transmembrane potential declines relatively slowly, and is characterized by a transient increase in inward Ca^{2+} ion conductance, along with an increase in outward K^+ ion conductance. Phase 2 is followed by the repolarization phase of the AP (Phase 3), in which the membrane potential drops to resting position (Phase 4), resulting from an increase in the outward K^+ accompanied by a decline in the inward Ca^{2+} ion conductances.

Electrical activity induces the mechanical activity through the mechanism of ECC (Fig. 1.4), and systole cycle occurs as a result. This event starts during depolarization (Phase 0) when an AP triggers the calcium-induced-calcium-release process that increases the concentration of Ca^{2+} ions. The Ca^{2+} concentration then binds to troponin C and initiates contraction through the development of tension that is generated through the action of actin and myosin cross-bridge cycling. Cardiac myocytes return to the resting membrane potential when the concentration of Ca^{2+} is back to its normal level, and diastole occurs [13].

Cardiac contraction which occurs as a response to ECC affects the electrical properties of the heart via the mechanism of MEF. It can affect the passive electrical properties of cardiac tissue. However, the main effects of MEF is delivered via the so-called stretch-activated ion channels and is caused by stretch-activated currents (I_{sac}). MEF affects the APD in a manner dependent on basic cycle length. I_{sac} is only activated when a cell is stretched. In response to stretching, different responses of I_{sac} on the AP are possible, which depend on its timing and magnitude. I_{sac} can modulate the APD if it is applied during the plateau phase. This means it will change the repolarization of AP, which leads to either lengthening (shortening) of the AP if

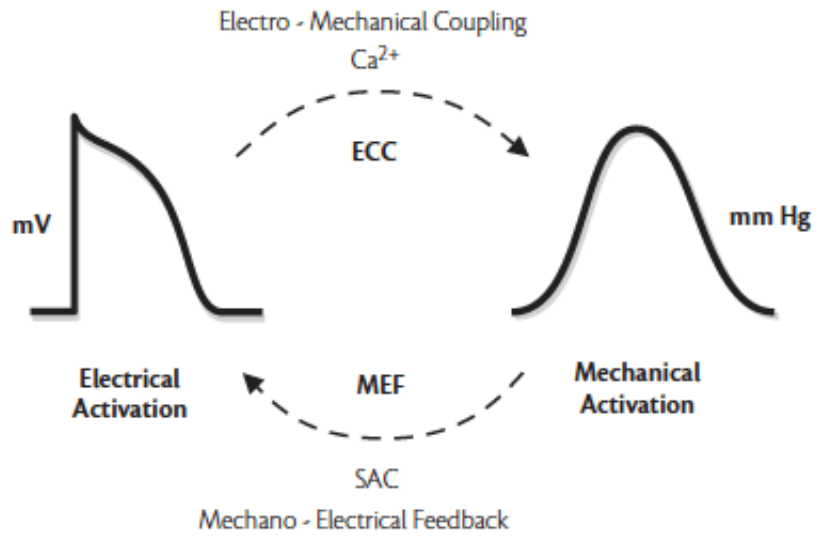

Figure 1.4: Schematic diagram of the coupling of the electrical and mechanical activities of the heart. The effects of Mechano-Electrical Feedback (MEF) is delivered via stretch-activated channels (SAC), and the effects of Excitation-Contraction Coupling (ECC) is delivered via the calcium ions (Ca^{2+}).

I_{sac} is inward (outward). The magnitude of the change in APD depends on the values of the I_{sac} models parameters (potential reversal and conductance). In addition, when I_{sac} is an inward current, it can depolarize the cell, and can even, if its strength is large, initiates an electrical impulse (called ectopic beat) when it is applied at the resting potential. MEF is believed to have pro-arrhythmic and anti-arrhythmic effects on cardiac electrophysiology, however its effects during alternans is very little studied in literature.

1.2.2 Cardiac alternans

Electrical alternans is a physiological phenomenon manifested as beat-to-beat oscillation (electric wave width alternation) of the cardiac Action Potential Duration (APD)[3]. Alternans has been shown to be a precursor to arrhythmias [1, 2] and sudden cardiac death (SCD), which is the most common cause of death in the industrialized world. Experimentally, APD alternans is typically observed during rapid pacing at a fixed pacing frequency so that beyond a critical pacing frequency the normally periodic response is replaced by a sequence of long and short APDs as

presented in Fig. 1.5. In this figure, APD is defined as the period of time during which the action potential exceeds the given threshold value, while the diastolic time interval (DI) is defined as the period of time during which the AP is below the threshold value. The basic cycle length (BCL) or simply the pacing period is held constant so that BCL = $APD_n + DI_n$. Clinically, the appearance of alternans is reflected in a beat-to-beat alternation of T-wave amplitude, known as T-wave alternans (TWA), on the electrocardiogram (ECG), and that the presence of TWA increases the risks of VF [4, 14]. At tissue levels, APD alternans can be either spatially concordant (SCA), where the APDs alternate in phase (whole tissue exhibits the same APD alternation) or spatially discordant (SDA), where the alternation of APD in different regions are out of phase. SDA is more arrhythmogenic than SCA since it can increase spatial dispersion of refractoriness, which can cause conduction block and can result in reentry and wavebreak [15].

Many control algorithms have been used in the literature for annihilation of the alternans. However, the majority of these algorithms [16, 17, 18, 19, 20, 21] that have been developed to date to suppress alternans in cardiac tissue are feedback controls that utilize the difference between the measurements of two most recent APDs to make small adjustments to the timing of the electrical stimuli. These algorithms are particular implementations of time-delay auto-synchronization [22] and extended time-delay auto-synchronization [23] feedback control techniques. Hall *et al.* [16] used this approach to successfully control cardiac arrhythmia called an alternans rhythm in vitro rabbit hearts. Similarly, Rappel *et al.* [17] suppress alternans in two geometrical models of both 1D and 2D tissues, and concluded that several control electrodes need to be placed on tissue in order to stabilize the normal heart rhythm. Control of atrioventricular-nodal conduction alternans has also been demonstrated in vivo human hearts [18] by stabilizing the underlying unstable steady-state conduction. The first experimental attempt to implement the electrical pacing interval technique is due to Hall and Gauthier [20], who succeeded in suppressing alternans in small pieces (< 1 cm) of bullfrog cardiac muscle. Echebarria and Karma [19] were the first to investigate theoretically this approach in a model of Purkinje fibers. They showed, using Noble model, that alternans in fibers no longer than ≈ 1 cm could be suppressed using a single electrode. Their theoretical results were experimentally

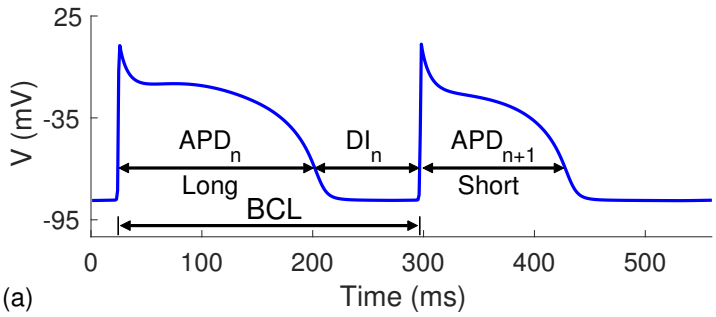

Figure 1.5: Time evolution of transmembrane potential in the phase one Luo-Rudy model.

verified by Christini *et al.* [21]. In addition, Dubljevic *et al.* [24] proved that, in this approach, failure to annihilate alternans completely in tissues exceeding 1 cm length is due to the lack of information of the spatial evolution of alternans away from the pacing site.

It has been shown theoretically and experimentally that the above mentioned control technique has a finite degree of controllability, such that alternans stabilization in cardiac tissues of length greater than 1 cm cannot be achieved [19, 21, 24, 25]. Although such algorithms have proved effectiveness for controlling electrical alternans in small tissues, several electrodes need to be implanted along the cardiac tissue's length ($\approx$ 6.25 cm) so that each pacing electrode can suppress alternans in a finite part of the tissue ($\approx$ 1 cm). In this thesis, we used computational models of cardiac electromechanics to study the effects of MEF on the electrical activity of the heart.

1.2.3 Models of cardiac electromechanics

Mathematical modelling is a powerful tool in cardiovascular research, and computational models of the heart have been used extensively to provide insight into the mechanisms underlying cardiac arrhythmias which is often difficult to do experimentally. From mathematical point of view, electromechanical (EM) models, that can be implemented in 1D, 2D, and 3D cardiac tissue, in which the electrical and mechanical activity of the heart are linked, are more suitable for our study.

In this section, we will introduce some basics about modelling of cardiac tissue, applied in the following chapters of this thesis. A variety of these models have been developed to investigate various physical phenomena and they can be mainly classified

into two categories. The weakly coupled EM models [26, 27, 28, 29] that account for the effects of electrical activity on the cardiac mechanics only, i.e., one way coupling, and the strongly coupled EM models [30, 31, 32, 33, 34] that account for the effects of electrical activity on the cardiac mechanics and the effect of mechanical deformation on electrical properties. For more details about the EM models, the reader is referred to [35, 36]. In general, a coupled EM model of cardiac tissue can be decomposed into four components, which are described below.

Cardiac excitation

The electrical activity of the heart can be described by the monodomain model [37] that includes only the effects of the intracellular space of the cell. The bidomain model [37] is an extension of the monodomain model including the effects of both the intracellular and extracellular space, which are separated by the cell membrane. The bidomain model, which is computationally very expensive, is the preferred model for simulating cardiac excitation when the main emphasis is how a voltage develops across the membrane. Many methods have been developed in the literature to reduce the computational challenges of these models [38, 39, 40, 41, 42, 43, 44]. A comparison between mondomain and bidomain models can be also found in [45]. In this thesis, a monodomain model is used to represent cardiac excitation, and is described by a parabolic partial differential, coupled with a nonlinear system of ODEs describing the ionic currents flowing across the cardiac membrane:

$$\begin{aligned} C_m \frac{\partial V}{\partial t} &= \frac{\partial}{\partial X_M}\left(D_{MN}\frac{\partial V}{\partial X_N}\right) - (I_{ion}(\mathbf{u}, V) + I_{stim}), \\ \frac{d\mathbf{u}}{dt} &= \mathbf{f}(\mathbf{u}, V), \end{aligned} \tag{1.1}$$

where V is the membrane voltage, D_{MN} is the diffusion tensor that accounts for electrical anisotropy of cardiac tissue, C_m is the membrane capacitance, I_{stim} is the externally electrical stimulus applied at the pacing site, $\mathbf{f}$ a general function representing the choice of a cell model, $\mathbf{u}$ is the vector of dependent states variables, and I_{ion} is the ionic membrane current describing the excitable behavior of cardiac cells.

The functions I_{ion} and $\mathbf{f}$ can be described using either simple or ionic models. The simple models, such as Aliev-Panfilov model [46], contain less than four ODEs and

can be used to explain basic properties of cardiac tissue. On the other hand, ionic models, which contain more ODEs, can accurately reproduce properties of cardiac cells, such as shape of AP. The voltage-gated ion channels of the ionic currents are often described using the Hodgkin-Huxley description [47]. A variety of cardiac ionic models of different complexity have been developed to represent properties of cardiac cells of different types and species. Over 100 ionic models can be found at CellML Model Repository (www.cellml.com).

In this thesis, Aliev-Panfilov model and two cardiac ionic models, namely, Fox *et al.* model [48] and modified Luo-Rudy 1 (LR1) model [49, 54], were used to represent electrophysiological properties of the heart. LR1 which is a mammalian ventricular cell model, consists of six individual currents, and of a system of 8 ODEs. On the other hand, Fox model was developed to reproduce the electrical behavior of a canine ventricular myocyte. This model uses 13 currents and consists of a system of 13 ODEs. The modified LR1 and Fox *et al.* models were chosen for several reasons. First, the two ionic models describe the electrophysiology of ventricular myocytes are widely used in the literature. Second, using these models, the APD alternans can be induced at sufficiently high pacing rates. Third, realistic formulations of most ionic currents are included in both models.

Cardiac mechanics

Many biological soft tissues, including cardiac tissue, possess anisotropic and inhomogeneous material properties. The large deformation elasticity theory is used to describe the mechanical deformation of the heart. The nonlinear elasticity theory [50] is a subregion of the theory of continuum mechanics that deals with the mechanical behavior of materials. This theory makes it possible to quantitatively describe large deformations of cardiac tissues that are under the influence of forces, such as the tension generated by contractile cells of the heart. In this work, X (material description) is used to denote the coordinates of a material particle with respect to the undeformed configuration, while x (spatial description) is used to denote the coordinates with respect to the deformed configuration. A material description refers to the behavior of a material particle, whereas a spatial description refers to the behavior at

a spatial position. In this work, deformation was expressed with respect to the initial undeformed configuration. Therefore, all equations were expressed in terms of X.

The equations governing the deformations are derived using Newton's laws of motion [30, 51] and are expressed as:

$$\frac{\partial}{\partial X_M}(S^{MN}F_{jN}) = 0, \quad M, N, j = 1, 2, 3, \tag{1.2}$$

where $F_{jN} = (\partial x_j/\partial X_M)$ is the deformation gradient tensor, X_M are the material (undeformed) coordinates, x_i are the spatial (undeformed) coordinates, the uppercase subscripts (M and N) and lowercase subscripts (i and j) correspond to the original and current configurations, respectively, and S^{MN} is the second Piola-Kirchhoff stress tensor.

Two approaches, namely active strain and active stress, have been proposed to model the active mechanical response of the myocardium. For the active strain model, a multiplicative decomposition [52] of the deformation gradient tensor into a passive and an active part is assumed. The second model, which is the most widely used and it is adopted in this work, is based on the concept of active stress [30]. In this approach, S^{MN} is split into a passive and an active stress component [30], and is given by:

$$S^{MN} = \frac{1}{2}\left(\frac{\partial W}{\partial C_{MN}} + \frac{\partial W}{\partial C_{NM}}\right) + T_a C^{-1}_{MN}, \tag{1.3}$$

where $C_{MN} = (\partial x_k/\partial X_M)(\partial x_k/\partial X_N)$ is the right Cauchy-Green deformation tensor, T_a is active tension generated by the Cardiac Excitation-Contraction Coupling, and $W(I_1, I_2)$ is the strain energy function, from which the stress-strain relationship is derived, modeling the myocardium.

The transversely isotropic, orthotropic, and isotropic constitutive models have been used to describe passive mechanical properties of the heart [53]. The isotropic Mooney-Rivlin constitutive model, which is used to describe passive mechanical properties of the heart [30, 51, 54], is adopted in the present study, where the strain energy W is given by:

$$W(I_1, I_2) = c_1(I_1 - 3) + c_2(I_2 - 3), \tag{1.4}$$

with $I_1(\boldsymbol{C}) = \mathrm{tr}(\boldsymbol{C})$ and $I_2(\boldsymbol{C}) = \frac{1}{2}(\mathrm{tr}(\boldsymbol{C}) - \mathrm{tr}(\boldsymbol{C}^2))$ are the first two principal invariants of $\boldsymbol{C}$, and $\mathrm{tr}(\boldsymbol{C})$ is the trace of $\boldsymbol{C}$, and c_1 and c_2 are material constants.

Cardiac Excitation-Contraction Coupling

As for models of cardiac cells, One can use simplified or detailed models for the descriptions of excitation-contraction coupling. Several ECC models have been developed [30, 51, 55, 56]. In this thesis, a simplified model, namely Nash-Panfilov, and a detailed model, namely Niederer-Hunter-Smith (NHS), are used for the active tension generations. The Nash-Panfilov model [30] consists of one ODE and takes voltage as an input. The Niederer-Hunter-Smith (NHS) model [56], which depends on quantities derived from both the cardiac mechanics and excitation models, consists of a system of 5 ODEs and describes the intracellular calcium dynamics and cross-bridge binding, and can be written in its general form as:

$$\begin{aligned} \frac{d\mathbf{w}}{dt} &= \mathbf{g}(\mathbf{w}, [\mathrm{Ca}^{2+}]_{\mathrm{i}}, \lambda, \frac{d\lambda}{dt}, T_a), \\ T_a &= h(\mathbf{w}), \end{aligned} \tag{1.5}$$

where $\mathbf{w}$ is a vector of internal state variables, $\mathbf{g}$ and h are prescribed nonlinear functions, $[\mathrm{Ca}^{2+}]_{\mathrm{i}}$ is generated by the ionic model, and λ is the stretch (extension ratio) along the fiber direction, given by:

$$\lambda = \sqrt{(\boldsymbol{n}^T \mathbf{C} \boldsymbol{n})}, \tag{1.6}$$

where $\boldsymbol{n}$ is the unit fiber direction in the undeformed configuration. Contraction of the heart results from the active tension, generated by electrical stimulation, and the S_a^{MN} (introduced previously) corresponding to T_a is given by:

$$S_a^{MN} = T_a C^{MN}, \tag{1.7}$$

where C^{MN} is the contravariant metric tensor.

Cardiac Mechano-Electrical Feedback

The main effect of mechano-electric feedback is delivered via the so-called stretch-activated ion channels and is caused by stretch-activated currents I_{sac} [7]. A linear voltage-current relationship has been found in experimental studies [57, 58, 59] and linear ionic models have been proposed [57, 60, 61, 62, 63, 64, 65, 66, 67] for I_{sac}. In this thesis I_{sac} as described in [67] is adopted, and is given as:

$$I_{sac} = G_s \frac{(\lambda - 1)}{(\lambda_{max} - 1)} (V - E_s), \tag{1.8}$$

where λ is the stretch, given in Eq. (1.8), along the fiber direction; and λ_{max} is the maximal stretch, which we set to λ_{max}=1.1 as in Ref. [67]. G_s and E_s are the conductance and reversal potential parameters, respectively. Following [67], the parameter G_s can take any value between 0 and 100 μS/μF [7, 68], and E_s in most biophysical models takes the value of $-20\ mV$ [7]. As shown in [67], cardiac cells are assumed to be stretched maximally between 5% and 10% of the resting position. The I_{sac} is active during stretch, i.e. it is only present when $\lambda > 1$, otherwise, $I_{sac} = 0$.

To take into account the effects of MEF on the electrophysiological properties of the heart, Eq. (1.1) is modified to obtain:

$$\begin{aligned} C_m \frac{\partial V}{\partial t} &= \frac{1}{\sqrt{C}} \frac{\partial}{\partial X_M} \left(\sqrt{C} D_{MN} C^{-1}_{MN} \frac{\partial V}{\partial X_N} \right) \\ &\quad - (I_{ion}(\mathbf{u}, V) + I_{sac}(\lambda, V) + I_{stim}), \\ \frac{d\mathbf{u}}{dt} &= \mathbf{f}(\mathbf{u}, V), \end{aligned} \tag{1.9}$$

where $C = \det(C_{MN})$ (determinant of tensor C_{MN}).

1.3 Thesis Outline

In this thesis, a full study of the effects of mechano-electrical feedback on the electrical activity in the heart, through detailed exploration of complex ionic models, was conducted with the aim of suppressing the electrical alternans via MEF.

In Chapter 2, an EM model of cardiac tissue is employed to investigate the effects of MEF on the APD at the cellular and tissue levels close to the onset of alternans. Phase one of the Luo-Rudy model is used to represent the electrophysiological properties of the heart. We provide numerical simulations for a certain range of BCLs, and illustrate the effects of MEF on the APD, showing its anti-arrhythmic effects close to the alternans bifurcation. In particular, we show that, depending on the strength of MEF, the critical BCL corresponding to the onset of alternans may be decreased. The effects of MEF on the alternans are investigated also theoretically using a theoretical framework of iterative maps. In this study, a restriction is put on some of the parameter values of the model so that the effects of MEF on the CV can be neglected.

The effects of MEF on the dynamics of alternans when no restrictions are imposed

on the model parameters and for a wide range of BCLs are addressed in Chapter 3. The same EM model used in the previous chapter, but with the exception that FOX model is used to represent the excitation properties, is employed in this study. We show that the I_{sac} which is the main effects of MEF can increase the dispersion of refractoriness via its effects on the CV. In particular, our numerical results show that the I_{sac} can induce the transition from spatially concordant alternans to spatially discordant alternans, and that the dispersion of refractoriness can be increased when the alternans is discordant. In addition, the role of I_{sac} in shifting the threshold of CB to a lower pacing rate is described and discussed.

In Chapter 4, a novel mechanical perturbation algorithm for alternans control is developed. The proposed control algorithm combines the electrical boundary pacing and a spatially distributed mechanical perturbation that is applied at one place over a small localized region within the one-dimensional (1D) cable of cardiac cells. The feasibility of suppressing cardiac alternans is explored using the Nash-Panfilov model. When activated, the mechanical perturbation control, which is based on perturbing cardiac tissue mechanics, alters the repolarization of the AP, via MEF, in order to suppress alternans. Numerical examples are provided to demonstrate successful suppression of alternans in a 6.25 cm cable of cardiac cells of the Nash-Panfilov model using the proposed algorithm.

This mechanical perturbation method is extended in Chapter 5 to be implementable in two EM models of cardiac tissue. The phase one Luo-Rudy and Fox models are used to represent the electrical proprieties. Two different mathematical implementations are used to implement the mechanical perturbation algorithm. For the NHS model, the algorithm is implemented in one of the ODEs, namely the ODE that describes the spatiotemporal dynamics of the Ca^{2+} binding to TnC. In addition, a novel mathematical framework of 2D iterative map of the heart beat-to-beat dynamics that couples the membrane voltage and active tension systems at the cellular level is introduced. Stability analysis of the system of coupled maps is performed in the presence of a discrete form of the proposed control algorithm. Numerical simulations are given to demonstrate successful suppression of cardiac alternans.

In chapter 6, we conclude the thesis and present the suggestions for future research directions.

Chapter 2

Effects of mechano-electrical feedback on the onset of alternans: A computational study

2.1 Introduction

Under normal conditions at normal pacing rates, the electrically induced APs of excitable cardiac cells have similar durations. However, when pacing at a sufficiently high rate, the APD alternates between long and short values [Fig. 2.1(a)]. In tissue, this alternation can either be in phase (concordant alternans) or have parts that are out of phase with other parts of the tissue (discordant alternans). The APD alternans, which is characterized by a period-doubling bifurcation, has been shown to be a precursor of cardiac arrhythmias, some of which, such as ventricular fibrillation (VF), can lead to sudden cardiac death (SCD). Clinically, alternans are manifested as beat-to-beat fluctuations of T-wave amplitude, called T-wave alternans, on the electrocardiogram; this is an indicator of VF [4, 14] and SCD risk. Therefore, prediction of the onset of period-doubling instability in cardiac tissue is of particular importance in detecting and preventing VF.

Mathematically, a one-dimensional (1D) iterated map [69, 70] is usually used to characterize the APD alternans:

$$\mathrm{APD_{n+1}} = f(\mathrm{DI_n}) \tag{2.1}$$

Equation (2.1), known as APD restitution, relates the APD at the $n+1$-th beat to the previous diastolic interval (DI) [Fig. 2.1(a)] (i.e., the time elapsed between the

end of one AP and the beginning of the following one), where the BCL or simply the pacing period is held constant so that $\mathrm{BCL} = \mathrm{APD_n} + \mathrm{DI_n}$. Nolasco and Dahlen [69] were the first to show that whenever the slope of the APD restitution curve is greater than 1 (restitution hypothesis), a transition from normal heartbeat (period-1 rhythm) to alternans (period-2 rhythm) occurs. This was later formalized mathematically by Guevarra *et al.* [70] to show that the onset of alternans can be described as a period-doubling bifurcation, where the slope of the restitution curve corresponds to a derivative of the map (i.e., df/dDI). Many theoretical and experimental studies have extended this theory using the iterated map approach and bifurcation theory to explain more complex phenomena, such as chaos [71], in AP dynamics.

Many alternans studies still use this basic map representation, which assumes that modifications in DIs produce changes in APDs and that df/dDI determines the extent to which modifications in DIs produce APD alternans. However, many experimental studies have shown that the onset of APD alternans cannot always be predicted from the slope of the APD restitution; for example, in Hall *et al.* [72], APD alternans was absent in frog heart muscle even though the restitution slope was significantly greater than 1. On the other hand, Dilly & Lab [73] observed alternans during ischemia, even though the slope was significantly less than 1. It can be concluded that the APD does not depend only on the previous DI, as described in Eq. (2.1), and that other factors influence the APD alternans. Important factors that have been extensively described in the literature include calcium cycling dynamics and cardiac memory. In cardiac myocytes, membrane voltage (V) and intracellular calcium concentration ($[\mathrm{Ca}^{2+}]_\mathrm{i}$) are bi-directionally coupled and, at the cellular level, alternans arises from an interplay of V and $[\mathrm{Ca}^{2+}]_\mathrm{i}$-cycling dynamics [74, 75, 76, 77]. Hence, when the APD alternates, $[\mathrm{Ca}^{2+}]_\mathrm{i}$ alternates secondarily [see Figs. 2.1(a), 2.1(b)] owing to voltage-dependent ionic currents (referred to as $\mathrm{V} \rightarrow \mathrm{Ca}^{2+}$ coupling). Conversely, an alternation in $[\mathrm{Ca}^{2+}]_\mathrm{i}$ induces an alternation in the APD through calcium-sensitive ionic currents (referred to as $\mathrm{Ca}^{2+} \rightarrow \mathrm{V}$ coupling). This latter coupling can be either positive (elevation in $[\mathrm{Ca}^{2+}]_\mathrm{i}$ lengthens the APD) or negative (elevation of $[\mathrm{Ca}^{2+}]_\mathrm{i}$ shortens the APD). Another factor with an important role is the pacing history of the cell; thus, the APD usually depends on the series of DIs preceding it, and not just the immediately preceding DI, i.e., $\mathrm{APD_{n+1}} = f(\mathrm{DI_n}, \mathrm{DI_{n-1}}, \mathrm{DI_{n-2}}...)$. This phenomenon, known

as cardiac memory [78, 79, 80, 81, 82], is an intrinsic property of cardiac tissues. According to the theory of dynamical systems, the onset of alternans can be predicted from the eigenvalues of the map, i.e., bifurcation occurs when a characteristic eigenvalue leaves the unit circle through 1 [16, 75].

In the heart, electrical waves propagate through cardiac tissue and initiate mechanical contraction. On the other hand, the deformations caused by contraction affect the electrical waves via the phenomenon of MEF [6, 7, 8, 9]. It has been shown clinically that MEF can have both anti-arrhythmic and pro-arrhythmic consequences [10, 11]. Theoretical and experimental studies [83, 84, 85, 86, 87, 88, 33, 89, 90, 91] have been performed to uncover the mechanisms of MEF and its effects on cardiac electrical activity. The results suggest that MEF may play an important part in arrhythmogenesis [92, 93]. For instance, regions of substantial stretching induce large inward currents through stretch-activated channels (SAC) that can lead to conduction blocks, causing scroll wave breakup in these regions [91]. Conduction blocks can result in the initiation of reentry and fibrillation (see Refs. [94, 95]). Recent studies have shown that MEF may play a part in the restoration of normal cardiac electrophysiology [96, 97, 51, 54]. In Opthof *et al.* [96] the effect of the physiological left ventricular pressure pulse on ventricular repolarization was investigated using a Langendorff-perfused pig heart. It was demonstrated that with varying of the load in the left ventricle and the activation site, the normal ventricular pressure pulse tends to synchronize repolarization and therefore reduces susceptibility to ventricular arrhythmias. Also, a mechanical perturbation algorithm for controlling alternans via MEF has been presented [97, 51, 54]. It has been suggested that the amplitude of stretch-activated currents (I_{sac}) along a cable of 7 cm is modulated and applied during the repolarization of APs (between two predefined thresholds), when the control is activated, in order to suppress alternans.

One of the main effects of MEF results from I_{sac} (defined in Eq. (2.10)), which when activated can alter the electrical properties of the myocardium via SAC [7]. Studies have investigated the effects of SAC during different phases of the AP, and the responses vary depending on the timing of the mechanical stretch and the magnitude of I_{sac} [84, 10]. This will result in delays after depolarizations or an AP (when the magnitude of I_{sac} is above the threshold) [83, 62, 61, 98, 99, 89], if stretching

is applied during diastole. On the other hand, if stretching is applied during the plateau phase, it will alter repolarization of the AP [57, 100, 101, 102, 11, 99], leading to either shortening or lengthening of the AP; this change in the APD depends on the reversal potential [58] of the SAC, and the degree of shortening or lengthening of the APD is affected by the maximal conductance [58]. For instance, a mechanical induction occurring during the rat plateau, where the reversal potential of the SAC is near 0 mV, resulted in a prolonged APD [57], while in guinea pig cells, with a high plateau and a lower reversal potential, a shortening of the APD was observed [100]. In addition, the stretch-induced changes in the APD and the degree of modulation are dependent on cycle length [103, 104]; at long (short) cycle lengths, the APD is shortened (lengthened) under left ventricular loading by aortic occlusion. However, the mechanisms underlying the cycle-length-dependent effects of I_{sac} on the APD remain to be elucidated.

In this work, we study the effects of MEF on the onset of alternans, illustrating the cycle length dependency of the stretch response and the effects of MEF on the APD, using a 1D electromechanical model of the heart. In particular, we show that MEF, depending on the strength of I_{sac}, may decrease the critical BCL ($\mathrm{BCL_{crit}}$), which is the maximum BCL at which alternans occurs for this model when MEF is not present. Therefore, the influence of I_{sac} on the APD at different BCL values is analyzed and discussed. To this end, we use a strongly coupled biophysically detailed electromechanical model of the heart, named the LR1NHS model, that accounts for the effects of electrical activity on the contraction and the effects of MEF on cardiac excitation. Phase one of the Luo–Rudy [49] model is used to represent the electrophysiological properties, while the mechanical properties of the passive myocardium are described using the Mooney–Rivlin material model [54, 30]. The active tension (T_a) that couples the electrophysiological model to the cardiac mechanics model is generated using the Niederer–Hunter–Smith (NHS) [56] model. In addition, a 2D iterative map [54] that couples the AP and T_a at the cellular level is utilized to illustrate the effects of MEF on the bifurcation point.

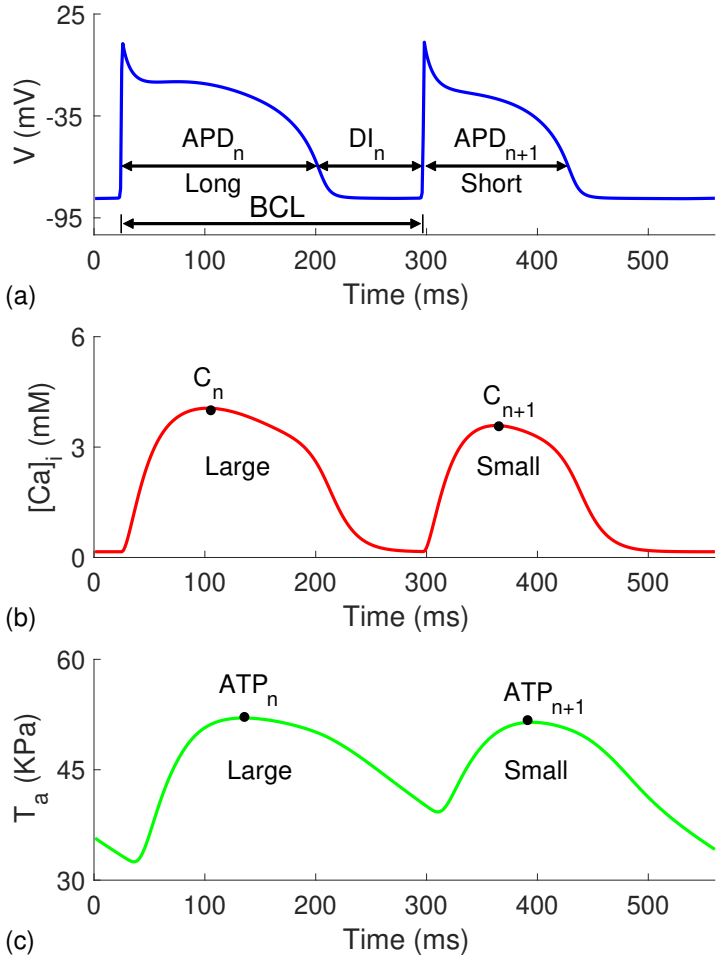

Figure 2.1: Time evolution of voltage (V) (a), intracellular calcium concentration ($[Ca^{2+}]_i$) (b), and active tension (T_a) (c) of the cell in the middle of a cable of length $L = 7$ cm in LR1NHS model, when it is paced at the boundary with basic cycle length (BCL) = 272 ms and a steady state is reached.

2.2 Methods

2.2.1 The cardiac electro-mechanical model

A strongly coupled electromechanical model of cardiac tissue can be decomposed into four components, which are described in the following subsections.

Mechanics model

Finite deformation theory is used to describe the mechanical deformation of cardiac tissue [50, 30]. If a quasi-static equilibrium is assumed, deformation is described by the following equation:

$$\frac{\partial}{\partial X_M}(S^{MN}F_{jN}) = 0, \quad M, N, j = 1, 2, 3, \tag{2.2}$$

where $F_{jN} = (\partial x_i/\partial X_N)$ is the deformation gradient tensor ($\mathbf{F}$), with lower case and upper case indices corresponding to spatial (deformed) and material (undeformed) coordinates, respectively; and S^{MN} is the second Piola–Kirchhoff stress tensor.

Myocardial properties include passive and active components. In this study, the active stress approach [30] is used to describe the active behavior of the myocardium. Therefore, S^{MN} is given by:

$$S^{MN} = S_p^{MN} + S_a^{MN}, \tag{2.3}$$

where S_a^{MN} is the active stress generated by the electrical stimulations as described in Eq. (2.9), and S_p^{MN} is the passive stress given by:

$$S_p^{MN} = \frac{1}{2}\left(\frac{\partial W}{\partial C_{MN}} + \frac{\partial W}{\partial C_{NM}}\right), \tag{2.4}$$

where $C_{MN} = (\partial x_k/\partial X_M)(\partial x_k/\partial X_N)$ is the right Cauchy–Green deformation tensor ($\mathbf{C} = \mathbf{F}^T \cdot \mathbf{F}$). $W(I_1, I_2)$ is the strain energy function modeling the myocardium as a Mooney–Rivlin hyperelastic material [54, 30], and is given by:

$$W(I_1, I_2) = c_1(I_1 - 3) + c_2(I_2 - 3), \tag{2.5}$$

where $I_1(\mathbf{C}) = \mathrm{tr}(\mathbf{C})$ and $I_2(\mathbf{C}) = \frac{1}{2}(\mathrm{tr}(\mathbf{C}) - \mathrm{tr}(\mathbf{C}^2))$ are the first two principal invariants of $\mathbf{C}$, $\mathrm{tr}(\mathbf{C})$ is the trace of $\mathbf{C}$, and c_1 and c_2 are material constants.

Electrophysiology model

The electrical activity in cardiac tissue is described by the monodomain model, which consists of a system of reaction-diffusion equations [37]. A modified version of this model [54, 67] that takes into account the effects of MEF can be written as:

$$\begin{aligned} C_m \frac{\partial V}{\partial t} &= \frac{1}{\sqrt{C}} \frac{\partial}{\partial X_M} \left(\sqrt{C} D_{MN} C^{NL} \frac{\partial V}{\partial X_L} \right) \\ &\quad - (I_{ion}(\mathbf{u}, V) + I_{sac}(\lambda, V) + I_{stim}), \\ \frac{d\mathbf{u}}{dt} &= \mathbf{f}(\mathbf{u}, V), \end{aligned} \tag{2.6}$$

where V is the membrane voltage, C_m is the membrane capacitance, $C = \det(C_{MN})$ (determinant of tensor C_{MN}), t is time, D_{MN} are the components of the diffusion tensor, C^{NL} are the components of the contravariant metric tensor (in an orthogonal material system, we have $C^{NL} = C_{NL}^{-1}$), I_{ion} represents the ionic membrane currents, $\mathbf{f}$ is a prescribed vector-valued function, $\mathbf{u}$ is a vector of dependent states variable describing membrane gates and ionic concentrations ($[\mathrm{Ca}^{2+}]_\mathrm{i}$ is one component of $\mathbf{u}$), λ is the stretch (given in Eq. (2.8)), and I_{stim} is the external stimulus current.

Active tension model

The active tension, generated by the electrical activity and coupled to nonlinear elasticity equations describing deformation of the myocardium, is described by the NHS model [56]. This model, consisting of a nonlinear ordinary differential equation (ODE) system and describing the intracellular calcium dynamics and cross-bridge binding, can be written in its general form as:

$$\begin{aligned} \frac{d\mathbf{w}}{dt} &= \mathbf{g}(\mathbf{w}, [\mathrm{Ca}^{2+}]_\mathrm{i}, \lambda, \frac{d\lambda}{dt}, T_a), \\ T_a &= h(\mathbf{w}), \end{aligned} \tag{2.7}$$

where $\mathbf{w}$ is a vector of internal state variables, $\mathbf{g}$ and h are prescribed nonlinear functions (the precise form of $\mathbf{w}$, $\mathbf{g}$, and h are given in the supplementary material), $[\mathrm{Ca}^{2+}]_\mathrm{i}$ is generated by the ionic model (given in the next section), and λ is the stretch (extension ratio) along the fiber direction, given by:

$$\lambda = \sqrt{(\boldsymbol{n}^T \mathbf{C} \boldsymbol{n})}, \tag{2.8}$$

where $\boldsymbol{n}$ is the unit fiber direction in the undeformed configuration. Contraction of the heart results from the active tension, generated by electrical stimulation, and the S_a^{MN} (introduced previously) corresponding to T_a is given by:

$$S_a^{MN} = T_a C^{MN}, \tag{2.9}$$

where C^{MN} is the contravariant metric tensor.

Ionic membrane model and stretch-activated currents

The functions $I_{ion}(\mathbf{u}, V)$ and $\mathbf{f}(\mathbf{u}, V)$ in the monodomain model (Eq. (2.6)) are given by the Luo–Rudy I (LR1) membrane model [49]. The LR1 model describes the electrophysiology of a ventricular cell from guinea pig and consists of six ionic currents and a system of eight ODEs including $[Ca^{2+}]_i$. The AP properties, including the APD alternans, of LR1 are mediated exclusively by V, since $[Ca^{2+}]_i$ passively follows the voltage. We modified the maximum conductance of the time-dependent potassium current to GK = 0.432 mS/cm^2, that of the sodium current to GNa = 16.0 mS/cm^2, and that of the slow inward current to Gsi = 0.06 mS/cm^2 in order to reduce the APD [105, 106], which was relatively large with the original parameter values, and to develop alternans at a shorter BCL.

Experimental studies [57, 58, 59] conducted on SAC have shown that I_{sac} (in the monodomain model (Eq. (2.6))) is induced when SAC are activated by mechanical stimulation, and that the current-voltage relationship is almost linear. Therefore, linear models have been proposed [60, 57, 61, 62, 63, 64, 65, 66] for I_{sac} and have been used to study the effects of stretching on cardiac dynamics. Following these studies, I_{sac} is modeled as in Ref. [67] and is given by:

$$I_{sac} = G_s \frac{(\lambda - 1)}{(\lambda_{max} - 1)}(V - E_s), \tag{2.10}$$

where λ is the stretch, given in Eq. (2.8), along the fiber direction; and λ_{max} is the maximal stretch, which we set to λ_{max}=1.1 as in Ref. [67]. G_s is the maximal conductance and E_s is the reversal potential. The value of G_s is within the range 0–100 μS/μF [7, 68]. For E_s, a range between -90 and 0 mV has been reported [7, 107, 91]. I_{sac} is only present during stretching (i.e., when $\lambda > 1$), otherwise $I_{sac} = 0$.

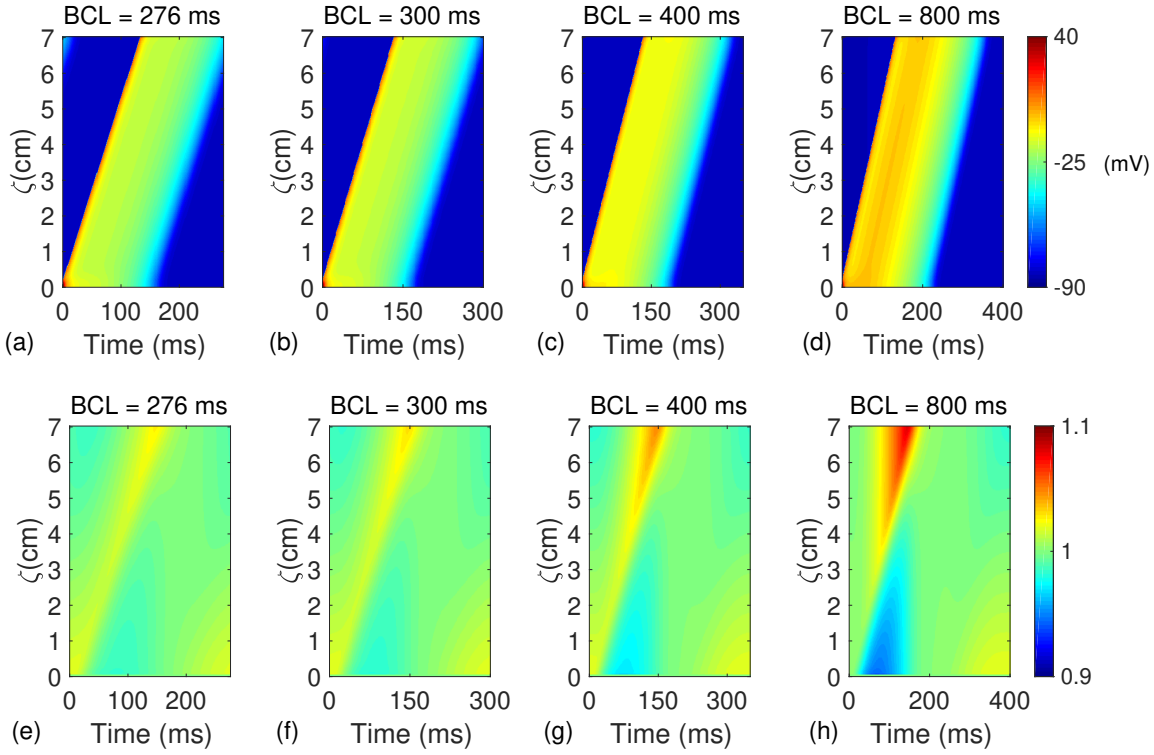

Figure 2.2: (Top and Bottom) Spatiotemporal evolution of V and λ in LR1NHS model during one beat at steady state when a 7 cm cable of cardiac cells is paced at the boundary (first five cells) with four values of BCL ((a,e) BCL = 276 ms, (b,f) BCL = 300 ms, (c,g) BCL = 400 ms, and (d,h) BCL = 800 ms), where BCL = 276 ms corresponds to the onset of alternans when MEF is not present.

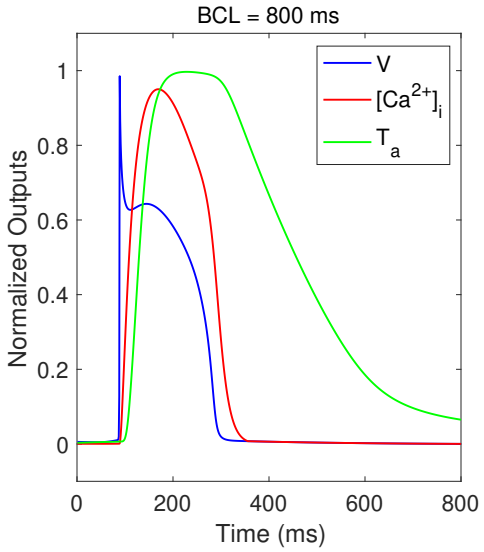

Figure 2.3: Time evolution of normalized V and $[Ca^{2+}]_i$ from LR1 model, and T_a from NHS model. The normalized outputs are given for the center cell in a 7 cm cable paced in the middle at BCL = 800 ms. As can be seen in this figure, there is a delay between the peak of the T_a and the peak of the V, since $[Ca^{2+}]_i$ has to increase to a certain value before it can trigger the initiation of T_a.

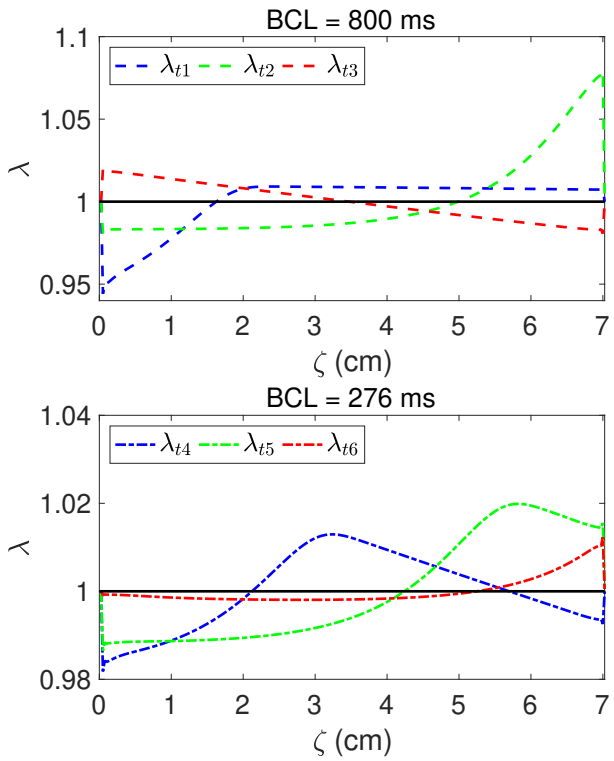

Figure 2.4: Stretch distribution at three different times for LR1NHS model at steady state when a 7 cm cable of cardiac cells, with both ends fixed, is paced at the boundary at BCL = 800 ms (top) and at BCL = 276 ms (bottom). λ_{t_1} (blue dashed line), λ_{t_2} (green dashed line), and λ_{t_3} (red dashed line) are the stretches at times $t_1 = 110$ ms after the last electrical stimulus, $t_2 = (t_1+100)$ ms, and $t_3 = (t_1+350)$ ms respectively when BCL = 800 ms. λ_{t_4} (blue dashed-dot line), λ_{t_5} (green dashed-dot line), and λ_{t_6} (red dashed-dot line) are the stretches at times $t_4 = 160$ ms, $t_5 = (t_4 + 50)$ ms, and $t_6 = (t_4 + 100)$ ms respectively when BCL = 276 ms.

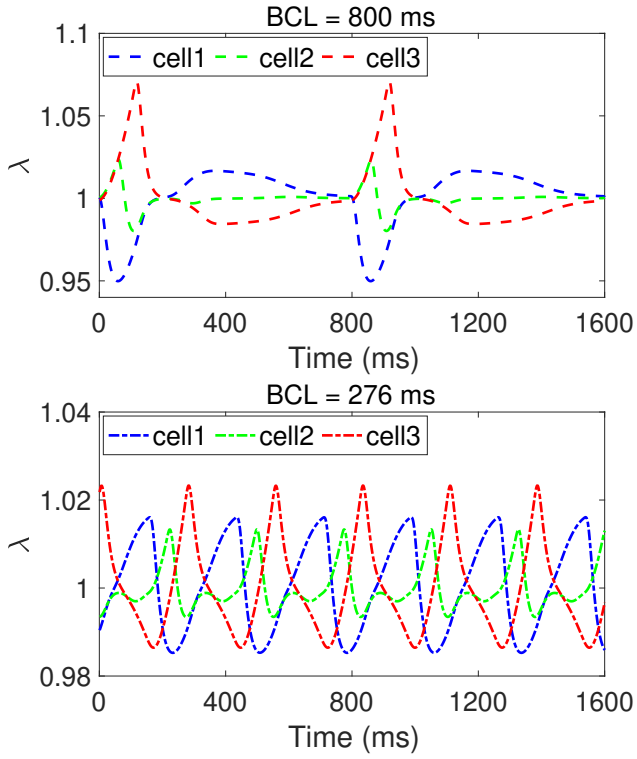

Figure 2.5: Variation of stretch at three different cells for LR1NHS model at steady state when a 7 cm cable of cardiac cells, with both ends fixed, is paced at the boundary at BCL = 800 ms (top) and at BCL = 276 ms (bottom). cell1, cell2, and cell3 are cells in the cable located at distance 0.5 cm, 3.5 cm, and 6.5 cm respectively from the pacing site (PS). Note that the time = 0 ms, which indicates the instant at which the recording begins in the top plot of this figure, corresponds to 40 ms after the last electrical stimulus for the three cells (dashed lines) while time = 0 ms in the bottom plot for the three cells (dashed-dot lines) corresponds to 135 ms after the last electrical stimulus.

Table 2.1: Parameter values used for the simulations of the LR1NHS model

Description	Parameter	Value
Membrane capacitance	C_m	1 μF cm^{-2}
Diffusion coefficient	D	0.001 cm^2 ms^{-1}
Mooney–Rivlin constant	c_1	0.1 MPa
Mooney–Rivlin constant	c_2	0.05 MPa
Maximal stretch	λ_{max}	1.1

2.2.2 1D mathematical model and numerical experiment setup

In this work, deformation was expressed with respect to the initial undeformed state. Therefore, all equations were expressed in terms of X (material coordinates). In the 1D setting, F_{11} (see Ref. [51]) is given by:

$$F_{11} = F = \partial x/\partial X, \tag{2.11}$$

where x and X are spatial and material coordinates, respectively. Let $x = X + u_d(X)$, where $u_d(X)$ is the displacement of a material point. Then we can write F as:

$$F = \partial x/\partial X = 1 + \frac{\partial u_d(X)}{\partial X}. \tag{2.12}$$

Assuming that the cardiac fibers are parallel to the X-direction of the undeformed configuration, λ (Eq. (2.8)) can be written as:

$$\lambda = \sqrt{C_{11}} = F. \tag{2.13}$$

In one dimension, the equations that govern both the electrical and mechanical behavior of the heart muscle can be written as:

$$\begin{aligned} C_m \frac{\partial V}{\partial t} &= D\frac{\partial^2 V}{\partial X^2} - (I_{ion}(\mathbf{u}, V) + I_{sac}(\lambda, V) \\ &\quad + I_{stim}), \end{aligned} \tag{2.14}$$

$$\frac{d\mathbf{u}}{dt} = \mathbf{f}(\mathbf{u}, V), \tag{2.15}$$

$$\frac{d\mathbf{w}}{dt} = \mathbf{g}(\mathbf{w}, [\mathrm{Ca}^{2+}]_\mathrm{i}, \lambda, \frac{d\lambda}{dt}, T_a), \tag{2.16}$$

$$T_a = h(\mathbf{w}), \tag{2.17}$$

$$\frac{\partial}{\partial X}\left(\frac{T_a}{1 + \dfrac{\partial u_d(X)}{\partial X}} + 2(c_1 + 2c_2)\,\frac{\partial u_d}{\partial X}\right) = 0, \tag{2.18}$$

$$\lambda = F = 1 + \frac{\partial u_d(X)}{\partial X}, \tag{2.19}$$

$$I_{sac} = G_s \frac{(\lambda - 1)}{(\lambda_{max} - 1)}(V - E_s). \tag{2.20}$$

The electrophysiology model is given by Eqs. (2.14) and (2.15), where $D = D_{11}$ is the diffusion coefficient, the functions $I_{ion}(\mathbf{u}, V)$ and $\mathbf{f}(\mathbf{u}, V)$ are given by the LR1 model described in the previous section, and I_{sac} is given by Eq. (2.20). The governing equations for the mechanical component are given by Eq. (2.18) (see Ref. [51] for derivation details), and those describing the excitation-contraction coupling (ECC) are given by Eqs. (2.16) and (2.17), where the functions $\mathbf{g}$ and h are given by the NHS model. The electrophysiology equations (Eqs. (2.14) and (2.15)) are supplemented by no-flux boundary conditions corresponding to the assumption that the heart is electrically insulated. For the mechanical boundary conditions, we assume that both ends of the cable are fixed in space, modeling an isometric contraction regime, and therefore Eq. (2.18) is supplemented with zero displacement boundary conditions. Note that the dependence of the electrical conductivity (i.e., the diffusion tensor) on the mechanical deformation was not incorporated into the 1D model (see limitations section for details).

In all cardiac electromechanical simulations, a cable of length $L = 7$ cm, fixed at its end points, is considered. The numerical schemes used to solve Eqs. (2.14)–(2.20) can be described as follows: (1) The derivatives were approximated with a semi implicit finite difference method. The temporal derivative was replaced with forward difference scheme and the first and second spatial derivatives were replaced with the central difference and standard second-order central difference schemes respectively. (2) The method of successive substitutions was used to transform the nonlinear boundary value problem (Eq. (2.18)) into a sequence of linear elliptic PDEs. We imposed no-flux boundary conditions for Eq. (2.14) ($\partial V/\partial X = 0$) and zero displacement boundary conditions at the fixed end points for Eq. (2.18) ($u_d(0) = 0$ and $u_d(L) = 0$). An electrical and mechanical step size of $\Delta x = 0.025$ cm and electrical time step of $\Delta t = 0.01$ ms were employed in all simulations. The electrical stimulus was applied as square wave pulses with a magnitude of 80 μA/μF and a duration of 1 ms. The parameters of the active tension model (Eqs. (2.16) and (2.17)) are given in Ref. [56], and those used in Eqs. (2.14), (2.18), and (2.20) are given in Table 2.1. Unless

otherwise stated, we used values of G_s = 15 μS/μF and E_s = -10 mV, and varied them to investigate the effects of these parameters on the APD and alternans.

The magnitude of the amplitude of the alternans is defined by:

$$|a_n(\zeta)| = |APD_n(\zeta) - APD_{n-1}(\zeta)|, \tag{2.21}$$

where n and ζ represent the beat number and space, respectively. The objective of this paper was to study the influence of MEF on the onset of alternans. Therefore, the set of Eqs. (2.14)–(2.20) that, together with the boundary conditions, constitute the LR1NHS model were solved numerically when the cable was paced at one end or in the middle with different BCLs, and when MEF was applied or not (setting G_s to zero in Eq. (2.20)). The solution's behavior and $|a_n(\zeta)|$ are analyzed and discussed.

2.3 Results and Discussion

2.3.1 Stretch distribution and its dependence on BCL

If a cable is paced (the first five cells are electrically stimulated) at one end with constant BCL, an electrical wave represented by V propagates [Figs. 2.2(a)–2.2(d)] and generates T_a, which is triggered by an increase in the $[Ca^{2+}]_i$ from the electrical model, see Figs. 2.1 and 2.3. As can be seen in Fig. 2.1, when BCL = 272 ms was less than BCL_{crit} = 276 ms (BCL_{crit} is defined as the maximum BCL at which alternans occurs in the LR1NHS model when MEF is not present), an alternation in the APD occurred and induced an alternation in $[Ca^{2+}]_i$ through the mechanism of ECC, which in turn induced an alternation in the active tension peaks (ATPs) (defined as the highest value of T_a within a beat [Fig. 2.1(c)]); therefore, a long (short) APD corresponds to a large (small) ATP. As the wave propagated from the pacing site (PS) to the other end of the cable, the generated T_a caused deformation of tissue; as a result, a stretch developed in the cable [Figs. 2.2(e)–2.2(h)]. As can be seen from this figure and Fig. 2.4, if at any given time some cells of the 1D cardiac cable are stretching ($\lambda > 1$), other cells are contracting ($\lambda < 1$), since, in an isometric setting, the cable's length remains fixed during mechanical contraction, meaning that the sum of λ for all cells is equal to the length of the cable ($\int_0^L \lambda \, dX = L$). Moreover, the maximal values of stretch developed in the cable at different BCLs are not equal

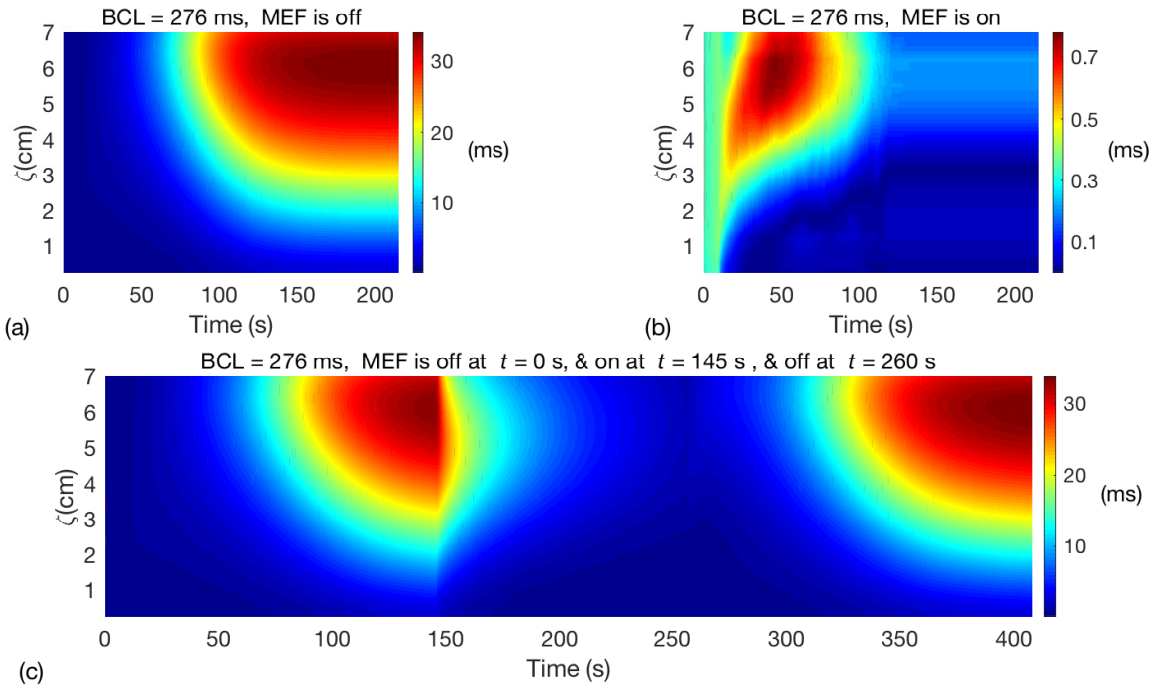

Figure 2.6: Magnitude of the amplitude of the alternans (Eq. (2.21) where the APD was measured at 90% repolarization (APD90)), for LR1NHS model without (a) and with (b) the presence of MEF, when a 7 cm cable of cardiac cells (the first five cells close to the PS which corresponds to $\zeta = 0$ cm) is paced at BCL = 400 ms and decreased gradually to $\text{BCL}_{\text{crit}} = 276$ ms, which corresponds to the onset of alternans in (a) but not in (b). (c) Similarly to (a), when MEF is turned off, alternans occurs when the cable is paced at $\text{BCL}_{\text{crit}} = 276$ ms, but when MEF is turned on at time = 145 s, the APD alternans is suppressed and then starts to regrow again when MEF is turned off at 260 s.

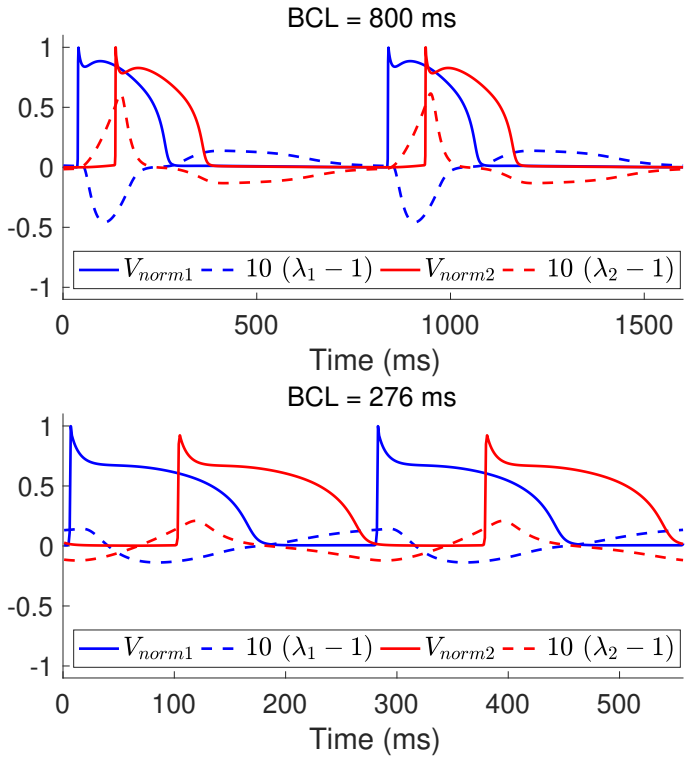

Figure 2.7: Time evolution of normalized V and 10 $(\lambda - 1)$ for two cells (cell1 and cell2) of LR1NHS model at steady state when a 7 cm cable of cardiac cells is paced at BCL = 800 ms (top) or at BCL_{crit} = 276 ms (bottom) in the presence of MEF. cell1 (blue dashed line) and cell2 (red dashed line) are located at 1 cm and 6 cm, respectively, from the PS.

and decrease with BCL, see Figs. 2.2(e)-2.2(h) and 2.5. As can be seen in Fig. 2.2, the maximal value of stretch (λ_{maxvs}) decreases when BCL decreases from BCL = 800 ms to BCL = 276 (that corresponds to the onset of alternans when MEF is not present); the relation between BCL and λ_{maxvs} is linear between BCL = 276 ms and BCL = 500 ms (see Fig. S.1 in the supplementary material). This is because when BCL is decreased, the APD and, consequently, ATP decrease with BCL. Note that λ depends on the T_a (Eqs. (2.18) and (2.19)); therefore, the magnitude, shape, and timing of deformation along 1D tissue depend on the magnitude, shape, and time of activation and relaxation of mechanical contraction activity. In turn, T_a depends mainly on the shape, activation, and relaxation time of the $[Ca^{2+}]_i$ of the ionic model used to represent the electrical activity of the cardiac cell. As can be seen in Figs. 2.2(e)–2.2(h) and 2.5, the stretch varies over time and its distribution along the cable is not symmetric if the cable is paced at the boundary ($x = 0$), see Figs. 2.2(e) and 2.2(g). In these figures, the cells that are closer to the other ends exhibit higher levels of stretch induced in the cable as a result of wave propagation, especially when BCL $\gg$ BCL_{crit}, compared with cells that are closer to the PS. One can conclude that stretching is not uniform along the cable and that it varies with BCL, with its magnitude decreasing when BCL decreases from 800 ms to BCL_{crit} = 276 ms.

2.3.2 Effects of MEF on the APD and alternans

I_{sac}, which is a function of λ and V (Eq. (2.20)), is considered to be the main effect of cardiac deformation on electrical activity. Therefore, the behavior of λ, which depends heavily on BCL, as discussed in the previous section, has a major role in determining the effects of I_{sac} on the APD and alternans.

We start by illustrating the effect of MEF on the onset of alternans. To this end, APD alternans was induced in a 1D cable (the five leftmost cells were paced periodically with period BCL_{crit} until a steady state was reached) under two conditions: with and without the presence of MEF. Therefore, two simulations were performed. In the first, G_s was set to zero in Eq. (2.20), corresponding to one-way coupling (in which there is no influence of cardiac deformation on electrical activity); in the second, $G_s = 15$ μS/μF, corresponding to two-way coupling (in which the influence of cardiac deformation on electrical activity is taken into account). In both simula-

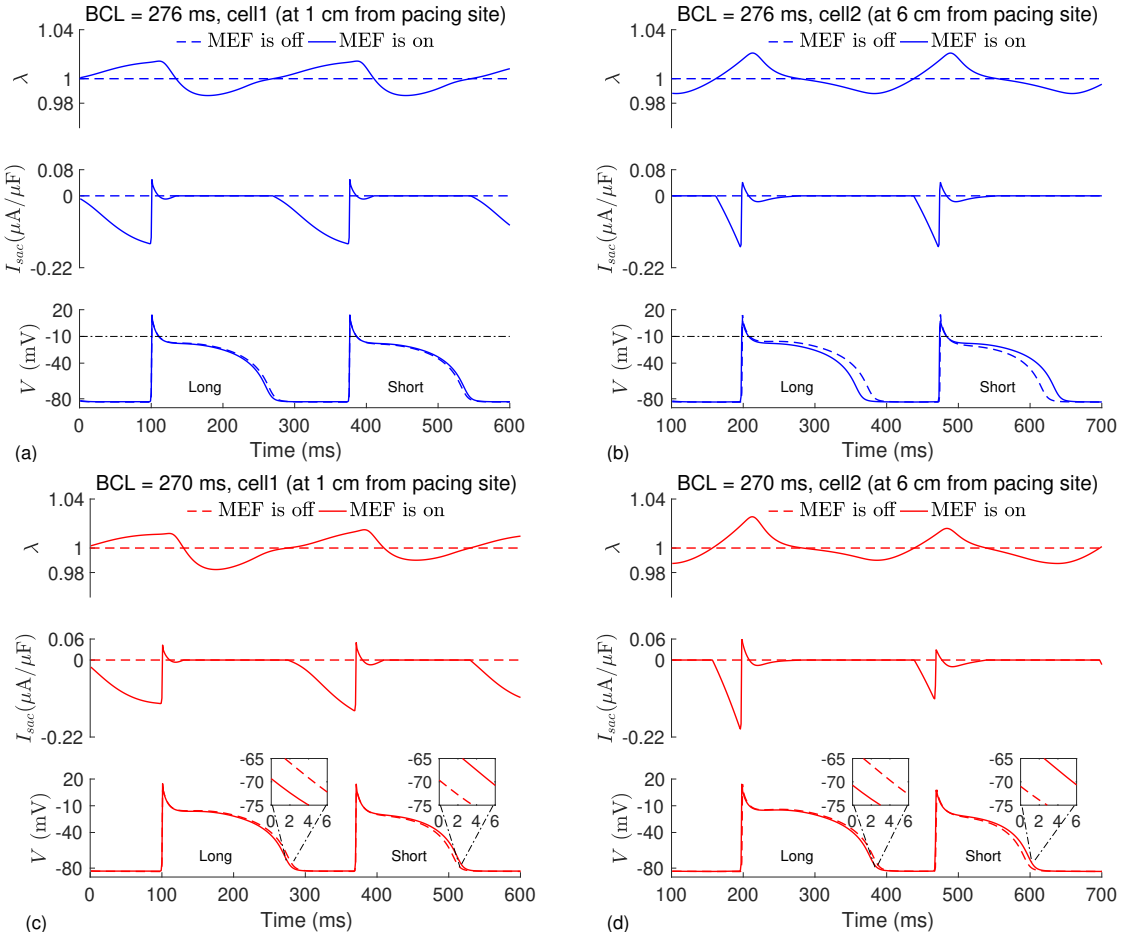

Figure 2.8: (Left and right) Time evolution of λ (top), I_{sac} (middle), and V (bottom) for the cells positioned 1 cm (left) and 6 cm (right) from the PS, of the LR1NHS model, when a 7 cm cable is paced at the boundary with 400 ms and decreased gradually to either 276 ms or 270 ms, and then paced periodically with $\mathrm{BCL_{crit}} = 276$ ms (a,b) or BCL = 270 ms (c,d) until a steady state is reached.

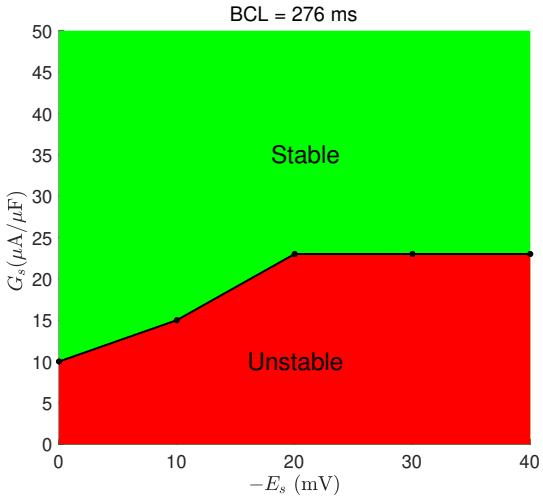

Figure 2.9: Plot showing the stable and unstable regions of the (G_s, E_s) plane. The green region corresponds to the values of the parameters of I_{sac} that suppress spatiotemporal alternans when a 7 cm cable is paced at the boundary with $\text{BCL}_{\text{crit}} =$ 276 ms and a steady state is reached.

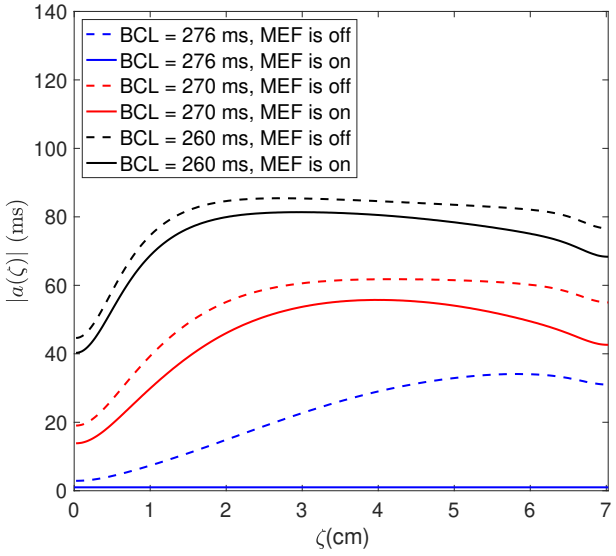

Figure 2.10: Magnitude of the amplitude of alternans for LR1NHS model at steady states, without MEF (dashed lines) and with MEF (solid lines), for four different BCLs, when a 7 cm cable is paced at the boundary with 400 ms and decreased gradually to BCL = 276 ms, 270 ms, or 260 ms, and then paced for 600 beats to its steady state. APD_{90} (APD at 90% repolarization) was adopted as a measure of APD.

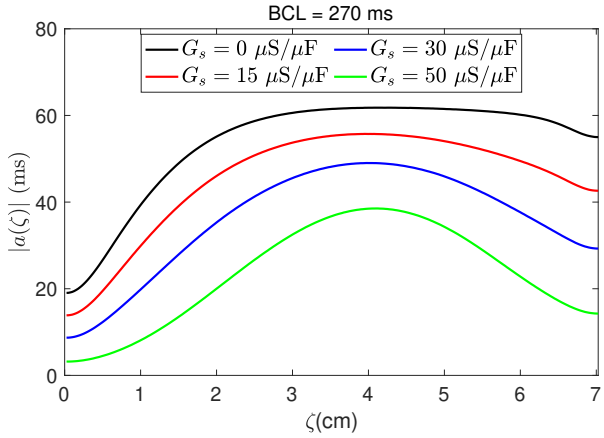

Figure 2.11: Magnitude of the amplitude of alternans for LR1NHS model at steady states for four different values of G_s, when a 7 cm cable is paced at the boundary with 400 ms and decreased gradually to 270 ms, and then paced periodically with BCL = 270 ms for 600 beats to its steady state. APD_{90} (APD at 90% repolarization) was adopted as a measure of APD.

tions, we set E_s = -10 mV. For the first condition (MEF off), the cable was paced at the leftmost boundary, starting at BCL = 400 ms and gradually decreasing to BCL = BCL_{crit} (i.e., for the onset of alternans). As can be seen in Fig. 2.6(a), APD alternans occurred when pacing with period BCL = 276 ms, which is the maximum BCL that allows alternans when MEF is off (BCL_{crit} = BCL = 276 ms). When similar actions were performed in the presence of MEF (MEF on), no alternans occurred at BCL_{crit} [Fig. 2.6(b)], and APD alternans occurred at BCL = 275 ms (simulation not shown). One can conclude that MEF has the effect of suppressing the APD alternans for a certain range of BCLs close to the BCL_{crit}. Note that the magnitude of alternans along the length of the cable was not uniform and it reached its minimum at the PS. Another numerical simulation that better illustrates the effects of MEF on the onset of alternans is shown in Fig. 2.6(c). This simulation was performed by excluding/including the MEF effects at specific times. As can be seen in Fig. 2.6(c), the alternans grew when MEF was not included and was suppressed by the inclusion of MEF, after which it regrew following the exclusion of MEF.

Before we could describe the influence of I_{sac} on the APD, it was necessary to illustrate how λ varies during repolarization when BCL is changed. Therefore, we plotted λ and V on the same figure for two BCLs (BCL = 800 ms and BCL = 276

ms). As can be seen in Fig. 2.7, the cells close to PS were mainly contracting during repolarization and stretching at the resting potential with BCL = 800 ms, while at BCL = 276 ms, they were stretching during early repolarization and early plateau phase and contracting afterward, then again stretching at the resting potential. On the other hand, cells that were close to the other cable end stretched during early repolarization and part of the plateau phase and contracted during late repolarization and at the resting potential with BCL = 800 ms, while at BCL = 276 ms they exhibited similar behavior to those with BCL = 800 ms, except that the magnitudes of the stretch were smaller, as discussed in the previous section. This has an important implication for the APD, as is discussed next.

We now investigate the effects of I_{sac} on the APD for different BCLs. We start with the case of BCL = $\mathrm{BCL_{crit}}$; therefore, λ, I_{sac}, and V for BCL = 276 ms at steady state were plotted in Figs. 2.8(a) and 2.8(b) for two cells located at different positions. One cell (cell1; $\zeta = 1$ cm) was located close to the PS and the other (cell2; $\zeta = 6$ cm) close to the other cable end. Also, we assumed that the APD was measured using a voltage threshold corresponding to 90 ($\mathrm{APD_{90}}$, i.e., the APD at 90% repolarization). As shown in Figs. 2.8(a) and 2.8(b), during early repolarization I_{sac} was an outward current and became an inward current when V was below -10 mV. The I_{sac} remained inward during the early plateau phase before reaching zero in the remaining part of the plateau phase and at late repolarization. Therefore, during early repolarization, I_{sac} produces a hyperpolarizing effect facilitating repolarization (i.e., accelerates the rate of early repolarization), then it produces a depolarizing effect delaying repolarization (i.e., slows the rate of repolarization); it has the same effect at the beginning part of the plateau phase, but no effect in the remaining part of the plateau phase or at late repolarization. This has the net effect of prolonging the short APD, and shortening the large APD, since the slowing process, which starts before the plateau phase, has enough time to increase the short but not the large. The reason is that, the plateau phase of the short APD is lower and shorter when compared with the large APD. Therefore, the relative time that I_{sac} remains inward during the plateau phase of the short APD is greater than the one of the large APD. The restoration of normal APDs was mainly due to the effect of the inward current (the net effect of I_{sac} on the large APD is small), which increased the short APD and caused, according

to the restitution relation, a decrease in the large APD. The inward current in the case of cell2 [Fig. 2.8(b)] was more significant when compared to the one in cell1 [Fig. 2.8(a)]. Therefore, the increase (decrease) in the short (long) APD was larger in cell2 than in cell1. When E_s = -30 mV, I_{sac} was always an outward current during repolarization and could not suppress alternans with the same value of G_s (Fig. 2.9); for E_s = 0 mV, I_{sac} during repolarization was almost entirely an inward current, which suppressed alternans for a smaller value of G_s (Fig. 2.9). Note that when I_{sac} is entirely an outward current during repolarization (the case where $E_s < -20$ mV), the suppression of alternans is feasible if the amplitude of I_{sac} is large enough to decrease the large APD and then increase (according to the restitution relation) the short APD. When BCL is greater than $\mathrm{BCL_{crit}}$, MEF has the effect of slightly shortening the APDs, and the mechanism of the effect of I_{sac} on the APD is similar to the case of the large APD described earlier. When BCL is lower than $\mathrm{BCL_{crit}}$, resulting in beat-to-beat alternation in the APD, the mechanism of the effects of I_{sac} on the small and large APDs are similar to those when BCL = $\mathrm{BCL_{crit}}$, which means it prolongs (shortens) the small (large) APD, see Figs. 2.8(c) and 2.8(d). As shown in Fig. 2.8(d) (at BCL = 270 ms and for the cell2), the large APD decreased by approximately 4.5 ms and the small APD increased by approximately 6 ms. As can be seen in Fig. 2.8, a large (small) APD corresponds to a large (small) amplitude of I_{sac}, since an alternation in the APD induces an alternation in the ATP through the mechanism of ECC; therefore, a large (small) APD corresponds to a large (small) ATP, which in turn induces an alternation in λ (large-small λ) for the same cell in the cable. Although alternans could not be suppressed at BCL = 270 ms when MEF was applied, the magnitude of its amplitude was decreased (see Fig. 2.10). This was because $|a_n(\zeta)|$ for the region close to PS when BCL = 270 ms was higher than that when $\mathrm{BCL_{crit}}$ = 276 ms, and the strength of the I_{sac} was not enough to account for the larger and smaller APDs. Moreover, the degree of alternation in stretching increased with BCL, and therefore the strength of I_{sac} increased (decreased) with increasing (decreasing) λ (Fig. 2.8); consequently, the effects of I_{sac} on the small APD decreased and its effects on the large APD increased slightly. In this way, the efficiency of I_{sac} decreases with BCL and restoring normal APDs cannot be achieved unless I_{sac} is modulated (see Ref. [54]). As can be seen in Fig. 2.10, the effect of

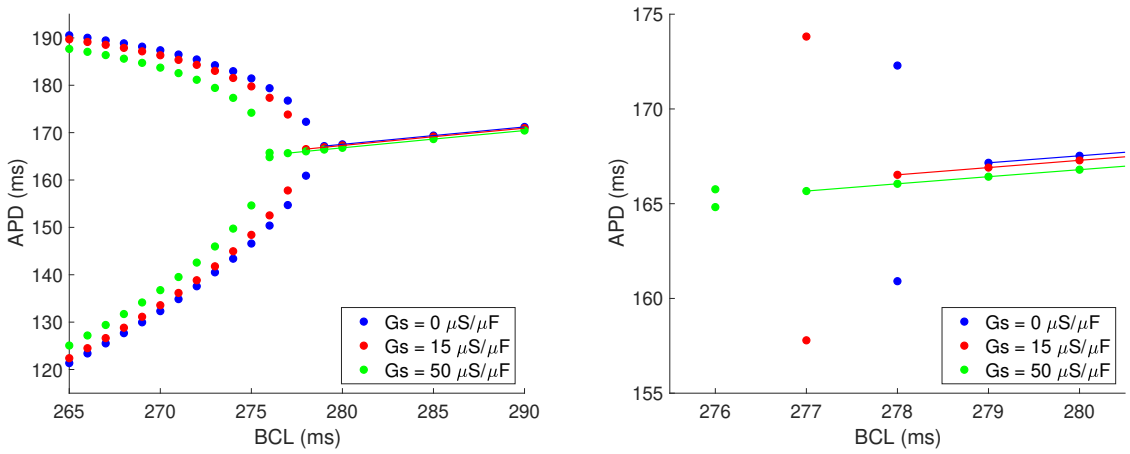

Figure 2.12: Bifurcation diagrams showing APD versus BCL for different values of G_s of LR1NHS model (left panel), and a zoomed-in version of it (right panel). The cell in the middle of a 7 cm cable is paced with a periodic current wave form with a magnitude of 86 μA/μF and a duration of 1 ms for different BCLs, starting at BCL = 350 ms and decreasing by 1 ms, after a steady state is reached for each BCL, until BCL is equal to BCL = 260 ms. This procedure was repeated for three values of G_s and the simulation values of the APD at steady state are plotted versus BCL. APD at 90% repolarization was adopted as a measure of APD.

MEF on the APD and consequently on $|a_n(\zeta)|$ decreased as the BCL decreased, with a tendency to become arrhythmic at lower BCLs (see limitations section). Note that the effects of I_{sac} on APDs were not equal for all cardiac cells along the cable, since λ was not uniform along the cable length and also varied with BCL.

Two parameters of the I_{sac} that have been shown to have important roles in the degree of lengthening and shortening of APDs are G_s and E_s (maximal conductance and reversal potential of I_{sac} (Eq. (2.20))). The effects of E_s on the onset of alternans (BCL = BCL_{crit}) are illustrated in Fig. 2.9. As can be seen in this figure, the efficiency of MEF decreased when $|E_s|$ increased (up to 20 mV), since, as stated before, the I_{sac} changes during repolarization from almost inward at $E_s = 0$ mV to an outward current at $E_s = -20$ mV. On the other hand, if we change the value G_s, this will change the magnitude of I_{sac} and its effects on APDs, which means that if G_s is increased the I_{sac} strength is increased, causing a decrease (increase) in the large (small) APD and thereby decreasing the $|a_n(\zeta)|$ (Fig. 2.11).

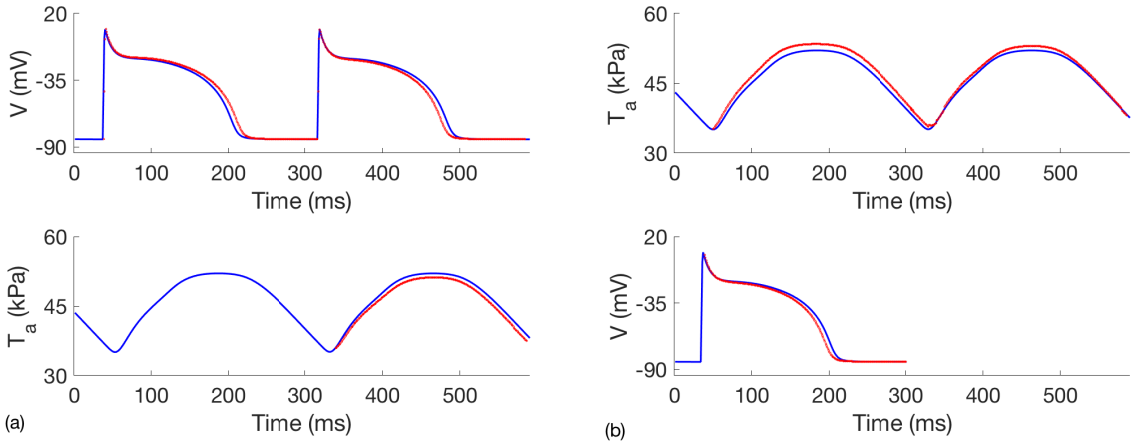

Figure 2.13: Evaluations of the terms R, A, B, and c at the fixed point of the map (Eq. (2.23)). To this end, the cell in the middle of a cable of length $L = 7$ cm is paced at BCL = 279 ms until steady state is reached (blue line). (a) $R = \partial APD_n/\partial APD_{n-1} = -\partial APD_n/\partial DI_{n-1}$ (restitution relation) and $A = \partial ATP_n/\partial APD_{n-1}$ ($V \to T_a$ coupling between the APD at a given beat and the ATP on the next beat) were evaluated as follows: a slight increase of the APD (red line) at a given beat from its steady state position (blue line) leads to a decrease in APD (red line), and ATP (red line) at the next beat (due to a shortening of the DI). R and A were evaluated by dividing the resulting decreases of APD and ATP respectively by the size of the initial increase of APD ($R \approx -1$ and $A \approx -0.13$). (b) $B = \partial ATP_n/\partial ATP_{n-1}$ and $c = \partial APD_n/\partial ATP_n$ ($T_a \to V$ coupling between the ATP and the APD at a given beat) were evaluated as follows: a slight increase of the ATP (red line) at a given beat from its steady state position (blue line) leads to an increase in ATP (red line) at the next beat, and to a decrease in APD (red line) at the same beat (the $T_a \to V$ coupling is negative in this model). B was evaluated by dividing the resulting increase in ATP by the size of the initial increase in ATP ($B \approx 0.02$), and c, which depends on the value of G_s chosen, is plotted versus G_s in Fig. 2.14.

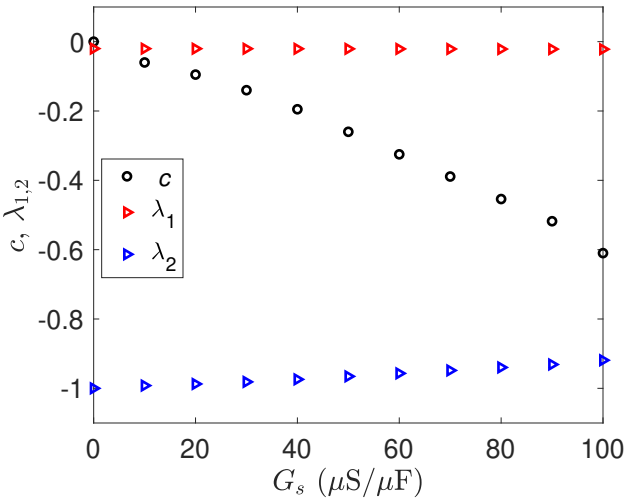

Figure 2.14: The strength of the MEF coupling effects (c) and eigenvalues ($\lambda_{1,2}$) (Eq. (2.27)) of J (Eq. (2.26)) are plotted versus G_s. $\lambda_{1,2}$ are plotted versus G_s since they are functions of c, which in turn is a function of G_s. Increasing G_s increases the magnitude of the strength of c, and the largest eigenvalue in absolute value ($|\lambda_2|$; blue triangle) decreases from $|\lambda_2| = 1$ when $G_s = 0$ μS/μF to $|\lambda_2| \approx 0.9$ when $G_s = 100$ μS/μF.

2.3.3 Effects of MEF on period doubling bifurcations

This section presents bifurcation diagrams obtained by numerical simulations for a single cardiac cell of the LR1NHS model that illustrate the effects of MEF on period doubling bifurcation. A theoretical framework of iterative maps is also presented and used to analyze the simulation results.

Bifurcation diagrams for varying strengths of MEF

In order to examine the effects of MEF on the period doubling bifurcation, we plotted APD versus BCL (bifurcation diagram) for a cell-based LR1NHS model and for different strengths of I_{sac}. To this end, the cell in the middle of a 7 cm cable, which was selected to minimize the electronic and boundary (electrical and mechanical) effects, was paced at different BCLs, ranging from 350 ms to 260 ms, for three different values of G_s (to regulate the strength of I_{sac}). Bifurcation diagrams (APD versus BCL) are given in Fig. 2.12. Note that, if the five cells in the middle of a 7 cm cable are paced with electrical stimulus of a magnitude of 80 μA/μF, the onset of alternans when MEF is not present corresponds to BCL = 276 ms (results not shown). The plot on

the right-hand side of Fig. 2.12 is a zoomed-in version of the bifurcation diagrams that include the BCLs close to bifurcation points corresponding to the three values of G_s. As can be seen in this figure, for $G_s = 0$ μS/μF (no MEF is applied), the bifurcation point corresponds to BCL = $\text{BCL}_{\text{crit}} \approx 279$ ms, while for $G_s = 15$ μS/μF, and 50 μS/μF, the new bifurcation points correspond to BCL ≈ 278 ms, and BCL $\approx$ 276 ms, respectively. Therefore, with increasing G_s, the bifurcation point moves left, which means that APD alternans can be induced at higher pacing rates (lower BCLs) when G_s is larger. Moreover, for all BCLs close to bifurcation points, corresponding to the three values of G_s, the $|a_n(\zeta)|$ are attenuated, and the attenuations decrease as BCL decreases. However, when pacing at BCL less than 240 ms, no effect of MEF on the $|a_n(\zeta)|$ was observed (bifurcation diagrams are shown in Fig. 2.12, for BCLs greater or equal to 265 ms, and Fig. S.2 in the supplementary material, for BCLs between 240 ms and 265 ms), and the MEF effect became pro-arrhythmic when pacing at BCL $\ll \text{BCL}_{\text{crit}}$.

Linear stability analysis

The effects of the MEF on the onset of instability is examined here using linear stability analysis. In our previous study [54], we developed a 2D iterated map that couples the AP and T_a at the cell level to incorporate the effects of MEF on the AP properties. In the development of this 2D map model, an approximation of λ ([54]) when $\lambda \leq 1.05$ is used, given by:

$$\lambda \approx 1 + \frac{T_b - T_a(X)}{\tilde{c} - T_a(X)},$$
$$\text{with } T_b \approx \frac{\int_0^L \frac{T_a(X)}{\tilde{c} - T_a(X)} dX}{\int_0^L \frac{1}{\tilde{c} - T_a(X)} dX}. \tag{2.22}$$

Hence, the I_{sac}, which is a function of λ and V, is expressed instead in terms of V and T_a so that a bidirectional coupling between the V and T_a at the cellular level exists, and a 2D iterative map can be introduced (see Ref. [54]). A slightly modified version of the 2D iterative map, which describes the beat-to-beat dynamics between the peak T_a and the APD at beat n to that at beat $n-1$, is given by:

$$APD_n = F_1(APD_{n-1}, ATP_n),$$

$$ATP_n = F_2(APD_{n-1}, ATP_{n-1}), \tag{2.23}$$

where ATP_n [Fig. 2.1(c)] is the ATP at beat n, measured from zero to the highest point in T_a, and APD_n [Fig. 2.1(a)] is the width of V at beat n, measured from the instant when V crosses the threshold value on the wave front until the instant it falls below this value on the wave back. In Eq. (2.23), the APD at beat n (APD_n) depends on the concurrent ATP (ATP_n) to express the effects of I_{sac} on the repolarization of membrane voltage during a beat. The 2D iterated map will be used to study the stability of a fixed point $X_* = (APD_*, ATP_*)$ of the map, close to the alternans bifurcation at the cellular level for the cell-based model of LR1NHS (LR1NHSC). Note that, as described previously, λ decreases from around 1 when a 7 cm cable of cardiac cells is paced at BCL = 800 ms, to less than 0.05 when it is paced with BCL close to $\mathrm{BCL_{crit}}$.

The stability of a fixed point X_* can be obtained from linearization of the nonlinear map (Eq. (2.23)) in the vicinity of X_* (see Ref. [54] for a detailed derivation).

$$\delta X_n \approx J\ \delta X_{n-1} \tag{2.24}$$

where $\delta X_{n-1} = X_{n-1} - X_*$ is a small perturbation from the fixed point, and $J = J(X_*)$ is the Jacobian matrix evaluated at X_*, given by:

$$J = \begin{pmatrix} \frac{\partial APD_n}{\partial APD_{n-1}} + \frac{\partial APD_n}{\partial ATP_n}\frac{\partial ATP_n}{\partial APD_{n-1}} & \frac{\partial APD_n}{\partial ATP_n}\frac{\partial ATP_n}{\partial ATP_{n-1}} \\ \\ \frac{\partial ATP_n}{\partial APD_{n-1}} & \frac{\partial ATP_n}{\partial ATP_{n-1}} \end{pmatrix} \tag{2.25}$$

The eigenvalues of J determine the stability of X_* to small perturbations. If all the eigenvalues of J have magnitude less than 1, the fixed point X_* is stable and the onset of instability corresponds to the largest absolute value of the eigenvalues passing through the unit circle. This instability gives rise to a period double bifurcation corresponding to alternans. To calculate the eigenvalues of J, we need first to evaluate the terms of the Jacobian matrix at the fixed point of the map, which corresponds to a period-1 rhythm, close to the alternans bifurcation. We start by rewriting the matrix J as:

$$J = \begin{pmatrix} R + c\ A & c\ B \\ \\ A & B \end{pmatrix}, \tag{2.26}$$

where $R = \frac{\partial APD_n}{\partial APD_{n-1}}$, $A = \frac{\partial ATP_n}{\partial APD_{n-1}}$, $B = \frac{\partial ATP_n}{\partial ATP_{n-1}}$, and $c = \frac{\partial APD_n}{\partial ATP_n}$. The term c, which measures the dependence of the voltage on the active tension, can also be considered a measure of the MEF coupling effects, since in the LR1NHSC model, I_{sac} is a function of V and λ, which in turn is a function of T_a (Eq. (2.22)); therefore, the effects of I_{sac} on the APD depend explicitly on ATP. In order to evaluate c, G_s was varied between 0 and 100 μS/μF to account for the strength of the I_{sac}. The evaluations of the terms R, A, B, and c at the fixed point of the map (Eq. (2.23)) are given in Figs. (2.13)–(2.14). The BCL was chosen so that, when MEF was not applied, the cell, which was paced at BCL, exhibited period-1 dynamics but very close to the bifurcation point ($R \approx -1$). For the case of $G_s = 0$, we have $c = 0$, which corresponds to $I_{sac} = 0$ (MEF off), and the eigenvalues of the matrix J are B and R, and, since $|R| = 1$, the fixed point X_* undergoes a period doubling bifurcation. For the general case when c is not zero (MEF on and its strength depends on the value of G_s), the stability of the system (Eq. (2.23)) is governed by the eigenvalues of the matrix J, which are given by:

$$\lambda_1 = \frac{1}{2}\left(R + c\ A + B + \sqrt{(R + c\ A + B)^2 - 4\ R\ B}\right),$$
$$\lambda_2 = \frac{1}{2}\left(R + c\ A + B - \sqrt{(R + c\ A + B)^2 - 4\ R\ B}\right). \tag{2.27}$$

The values of c when G_s is within the range of 0–100 μS/μF, and the eigenvalues $\lambda_{1,2}$ varying with G_s are sketched in Fig. 2.14. As can be seen in the figure, the magnitude of c (magnitude of the strength of MEF coupling effects) increased when G_s increased. Figure 2.14 shows that $|\lambda_2|$ (the absolute value of the largest eigenvalue of J) decreased when G_s increased. Therefore, as G_s increases, the strength of the I_{sac} increases and the period-doubling bifurcation point moves further right, effectively stabilizing the branch of unstable fixed points located close to the bifurcation point in the region of period-2 rhythm.

2.4 Limitations

All numerical simulations were performed under the assumption that the alternans was voltage driven (caused by voltage instability). Although this has been widely assumed in the literature, APD alternans can also be induced by calcium-driven

instability (caused by the instability of intracellular calcium cycling). Complex behaviors are possible in the latter case, depending on the strength of the calcium-driven instability and the nature of $Ca^{2+} \rightarrow V$ coupling [74, 75, 76].

In this work, we only considered isometric conditions (where both ends of the cable are fixed in space). This affects the distribution of stretching along the cable, as if muscle fibers are stretched in some regions of the cable, the fibers will be compressed in other regions, so that the length of the cable remains constant. For the isotonic case (boundary loading conditions), no constraint is imposed on the cable length; therefore, a change in the stretch distribution may occur. This may change how I_{sac} affects the APD and, consequently, its effects on the onset of alternans.

Conduction velocity (CV) restitution, which refers to the dependence of the CV of the AP on the preceding DI, along with the APD restitution curves, has been shown to have an effect on alternans [15]. Similar to other studies [91, 108], we found that the influence of MEF on the CV depends on BCL, G_s, and E_s, although it can be neglected for the values used in the LR1NHS model. However, for large values of G_s ($G_s > 50$ μS/μF), the myocardial stretch increased the CV, which, along with APD restitutions and lower BCL (BCL $\ll$ BCL_{crit}), has a critical role in discordant alternans (see Fig. S.3 in the supplementary material). On the other hand, the dependence of conductivity on mechanical stretching was not included in this study. A change in the conductivity could modify the CV, which plays a part in the development of alternans. However, with or without the inclusion of the effects of stretching on diffusion, the onset of alternans can be shifted to lower BCLs with an appropriate selection of the parameters of I_{sac} (G_s and E_s).

2.5 Conclusions and Future Works

This study investigated numerically and theoretically the effects of MEF on the onset of alternans. The numerical results were obtained using a 1D biophysically detailed electromechanical model of cardiac tissue. As demonstrated in this work, the distribution of stretching along the cable is not uniform and the stretch magnitude, which varies with BCL, is larger at BCL $\gg$ BCL_{crit}. Therefore, the stretch behavior along with the parameters G_s and E_s determine the effect of I_{sac} on the APD. In addi-

tion, a theoretical framework of 2D iterative maps that incorporate the effects of I_{sac} was used to demonstrate the MEF effects on the period-doubling bifurcation, corresponding to the onset of alternans in a single cardiac cell. In particular, we showed that $\mathrm{BCL_{crit}}$ can be shifted to lower values, where the degree of this shift depends on the strength of I_{sac}. The anti-arrhythmic effects of MEF was demonstrated using the LR1 model representing electrophysiological properties with the NHS model for active tension generation. Calcium sensitive currents, such as the L-type calcium current (I_{CaL}) and sodium-calcium exchange current (I_{NaCa}), are not included in LR1 model. However, we believe that if the alternans is voltage-driven, the presence of these currents will not reverse the effects of I_{sac}, which is also a calcium dependent current, on the APD. For example, in FOX model [48], these currents are included in this model, the alternans was suppressed when a modulated I_{sac} was applied [54]. But, if the APD alternans is calcium-driven, the situation is complex since the I_{CaL} and I_{NaCa}, which can prolong or shorten the APD, can have opposite effects and the net effect depends on the relative contributions of these currents to the APD [74, 75]. We expect the effectiveness and efficiency of MEF on the onset of alternans, that mainly depend on the AP and $[\mathrm{Ca}^{2+}]_{\mathrm{i}}$ dynamics, to vary among cell species. For example, myocytes of larger mammals, including humans, have longer APs than ones observed in smaller mammals such as rat and mouse. The AP and $[\mathrm{Ca}^{2+}]_{\mathrm{i}}$ dynamics affect the profile of T_a and consequently the distribution of mechanical stretch which plays the main role in APD changes.

The interaction between the mechanical and electrical events in the heart can be depicted as a simple closed-loop feedback control system, where the mechanical stretch can stabilize the electrical activity of the heart via MEF and in the vicinity of the alternans bifurcation. However, a potential role of MEF in arrhythmogenesis can be shown if a 7 cm cable of cardiac cells of LR1NHS model (but with larger magnitude values of G_s and E_s) is paced at lower BCLs ($\mathrm{BCL} \ll \mathrm{BCL_{crit}}$). This is because the non-uniform distribution of stretching produces, via SAC, a spatial dispersion in electrophysiological properties by converting an existing state of concordant alternans to discordant alternans. The latter state is considered to be very arrhythmogenic, since it increases the dispersion of repolarization and can result in a localized block [109, 110]. The results are beyond the scope of this paper but will be the subject of

future work.

SUPPLEMENTARY MATERIAL

See the supplementary material for a summary of the equations of NHS model (the NHS model is used to generate active tensions) and Figs. S.1-S.3, which show the variation of the maximal values of stretch versus BCL (Fig. S.1), bifurcation diagrams showing APD versus BCL for different values of G_s of LR1NHS model when BCL varies between 240 ms and 265 ms (Fig. S.2), and spatiotemporal evolution of V in LR1NHS model with $G_s = 0$ μS/μF (top), and with $G_s = 52$ μS/μF and E_s = -20 mV (bottom), with BCL = 210 ms (Fig. S.3).

Chapter 3

A simulation study of the role of mechanical deformation in arrhythmogenesis during cardiac alternans

3.1 Introduction

Irregular excitation waves in the heart may result in cardiac arrhythmias. Ventricular fibrillation (VF) [1, 2], which is the most dangerous form of arrhythmias, causes the contraction of the ventricles to become rapid and uncoordinated and can lead to sudden cardiac death if not treated within minutes. VF is recognized as one of the major causes of death in the industrialized world. Cardiac alternans which is characterized by a periodic alternations in the action potential (AP) duration (APD), is believed to precede VF, and can be clinically detected as T-wave alternans (TWA) using an electrocardiogram, and is associated with increased risk of cardiac arrhythmogenesis in many cardiac diseases [111, 112]. In a single cell, the genesis of alternans can be described based on APD restitution [69, 70]. This relation relates the current excited APD, and the previous diastolic interval (DI), which is the time between the end of the previous excitation and the current one. The APD restitution curve can be experimentally determined using a pacing protocol, such as the standard and dynamic restitution protocols [113, 114]. The standard restitution protocol [113], known as S1-S2 restitution protocol, which involves pacing the cell at a fixed cycle length S1 for a set number of beats, and then a premature stimulus at a variable cycle length

S2 is applied to elicit an extra beat, while the dynamic restitution protocol [114] involves delivering a number of stimuli at a constant BCL and progressively reducing the BCL. The transition from normal heartbeat to APD alternans occurs when the slope of the APD restitution curve is greater than 1 (known as restitution hypothesis). Although more complex effects, such as calcium handling dynamics, cardiac memory, and mechano-electric feedback, have been shown to influence the APD and consequently the condition for the appearance of alternans [74, 75, 81, 82, 97, 51, 54, 115], many studies still use this basic relation when studying cardiac alternans. In cardiac tissue, APD alternans can be spatially concordant (SCA), where alternation of APD are in phase (whole tissue exhibits the same APD alternation) or discordant (SDA), where the alternation of APD in different regions are out of phase. These discordant regions are separated by a nodal line in which no alternans is present. SDA is considered to be very arrhythmogenic [116, 14], since it increases the dispersion of repolarization that can result in blocking AP propagation and initiate reentrant waves. A number of mechanisms have been proposed to explain the production of SDA. Preexisting spatial heterogeneities has been identified first as being responsible for the production of SDA [14]. However, afterwards it has been found that SDA can also be formed in homogenous tissue [15, 117] when pacing at a sufficiently high rate so that conduction velocity (CV) restitution (dependency of the speed of the wavefront on the preceding DI) is engaged. Also, a number of dynamic factors, such as cardiac memory and calcium cycling dynamics, were found to be responsible for the transition from concordant to discordant alternans, see a brief review given in [118]. In the human heart, electrical waves propagate through the cardiac tissue and induce contraction of the heart. On the other hand, cardiac deformation affects the process of wave propagation via stretch-activated channels (SACs) [6, 7, 8, 9]. This mechanism which is known as mechano-electrical feedback (MEF) may have both antiarrhythmic and arrhythmogenic effects [10, 11, 119, 64], and has been studied for a long time [8]. For example, mechanical stretch has been shown to alter the electrical activity of the heart and play an important role during arrhythmias as in [91, 67], and on the other hand, it can suppress cardiac alternans as in [96, 115]. The time of application and strength of mechanical stretch relative to the different phases of AP can produce different responses. Application of stretch during plateau phase can

lead either to shortening or prolongation of AP [100, 57, 101, 102, 11, 99] depending on the reversal potential of the SACs [58]. If stretching is applied during diastole it can depolarize the resting membrane [84, 108]. Using a 1D biophysically detailed electromechanical model of cardiac tissue, it has been shown in [115] that the critical basic cycle length ($\mathrm{BCL_{crit}}$), that corresponds to the onset of alternans when MEF is not present, can be shifted to lower values, where the degree of this shift depends on the strength of the stretch-activated current (I_{sac}) which is the direct physiological influence of MEF. However, in that work, only a certain range of BCLs, that are closed to the $\mathrm{BCL_{crit}}$, were considered, and a restriction was put on the value of the I_{sac} conductance parameter so that the effects of MEF on the conduction velocity (CV) restitution can be neglected. In this work, we study the effects of MEF on the dynamics of alternans when no restrictions is imposed on the model parameter conductance value and the whole range of pacing periods that correspond to alternans is considered. In particular, we illustrate the role of I_{sac} in the transition from SCA to SDA, and in the increase of the dispersion of repolarizations when the alternans is discordant. In addition, we show that for some values of I_{sac} model parameters, the onset of conduction block can be shifted to a lower pacing rate. Therefore, the effects of I_{sac} on APD and CV restitution properties will also be studied and elucidated. To this end, a one dimensional (1D) biophysically detailed electromechanical of cardiac tissue is employed. Fox *et al.* model [48] which is an ionic cell model of the canine ventricular myocyte is used to represent the excitation properties. The active tension (T_a) model that couples the excitation model to the cardiac mechanics model is generated using the Niederer-Hunter-Smith (NHS) model [56]. The myocardium passive behavior is described using the Mooney-Rivlin (MR) material model [30, 54, 54]. In the following sections we denote this detailed electromechanical model by FOXNHS.

3.2 Methods

3.2.1 Electromechanical model of cardiac tissue

The effects of MEF on the dynamics of alternans were studied using a computational model of cardiac electromechanics. Mathematically, cardiac excitation and mechanics are described by coupled reaction-diffusion-mechanics equations, see [115] for a

detailed description. Fox model is used to represent electrical activity in heart tissue, while the passive mechanical behavior of the myocardium is described by the MR material response. Active tension which couples detailed biophysical model for cardiac excitation to cardiac mechanics model is generated using the NHS model. In one dimension, the whole set of equations that govern both the electrical and mechanical behavior of the heart muscle can be written as

$$C_m \frac{\partial V}{\partial t} = \frac{D}{F}\frac{\partial}{\partial X}\left(\frac{1}{F}\frac{\partial V}{\partial X}\right) - (I_{ion}(\mathbf{u}, V) + I_{sac}(\lambda, V) + I_{stim}), \tag{3.1}$$

$$\frac{d\mathbf{u}}{dt} = \mathbf{f}(\mathbf{u}, V), \tag{3.2}$$

$$\frac{d\mathbf{w}}{dt} = \mathbf{g}(\mathbf{w}, [\mathrm{Ca}^{2+}]_{\mathrm{i}}, \lambda, \frac{d\lambda}{dt}, T_a), \tag{3.3}$$

$$T_a = h(\mathbf{w}), \tag{3.4}$$

$$\frac{\partial}{\partial X}\left(\frac{T_a}{1 + \dfrac{\partial u_d(X)}{\partial X}} + 2(c_1 + 2c_2)\,\frac{\partial u_d}{\partial X}\right) = 0, \tag{3.5}$$

$$\lambda = F = 1 + \frac{\partial u_d(X)}{\partial X}, \tag{3.6}$$

$$I_{sac} = G_s \frac{(\lambda - 1)}{(\lambda_{max} - 1)}(V - E_s). \tag{3.7}$$

Where $D = D_{11}$ is the diffusion coefficient, $I_{ion}(\mathbf{u}, V)$ and $\mathbf{f}(\mathbf{u}, V)$ are given by the Fox model, I_{sac} is given by Eq. (3.7), and I_{stim} is the electrical stimulus. Eqs. (3.1) and (3.2) describe the electrophysiology model, while the governing equations for the cardiac mechanics are given by Eq. (3.5). The excitation-contraction coupling are described by Eqs. (3.3) and (3.4), where the functions $\mathbf{g}$ and h are given by the NHS model. Eqs. (3.1) and (3.2) are supplemented by no-flux boundary conditions, and Eq. (3.5) is supplemented with zero displacement boundary conditions modeling an isometric contraction regime. The parameters used in Eqs. (3.1), (3.5), and (3.7) are given in Table 3.1.

The objective of the paper is to study the influence of MEF on the dynamics of alternans in FOXNHS model. Therefore, the set of Eqs. (3.1)-(3.7) are solved numerically when the cable is paced at one end or in the middle with different BCL, and when MEF is applied or not (set $\lambda = 1$ in Eqs. (3.1), (3.3), and (3.7)) and the solution's behavior will be analyzed and discussed. In all simulations, a 7 cm

cable of cardiac cells, with both ends fixed, of the FOXNHS model is considered. Numerical schemes used for solving electromechanical equations in [54] are also used in this work to solve Eqs. (3.1)-(3.7). The no-flux boundary conditions and zero displacement boundary conditions are imposed for Eqs. (3.1) and (3.5) respectively. The step size $\Delta x = 0.02$ cm and step time $\Delta t = 1$ ms were used in all simulations. I_{stim} is applied as square wave pulses with a magnitude of 80 μA/μF and a duration of 1 ms. Unless otherwise stated, we use values of $G_s = 30$ μS/μF and E_s = -10 mV, and vary these parameters to investigate their effects on the alternans. In this work, the amplitude of the alternans is also plotted and is given by:

$$a_n(\zeta) = [APD_n(\zeta) - APD_{n-1}(\zeta)](-1)^n, \tag{3.8}$$

where n and ζ represent the beat number and space, respectively.

Table 3.1: Parameter values used for the simulations of the FOXNHS model

Description	Parameter	Value
Membrane capacitance	C_m	1 μF cm^{-2}
Diffusion	D	0.001 cm^2 ms^{-1}
Mooney-Rivlin constant	c_1	0.05 MPa
Mooney-Rivlin constant	c_2	0.025 MPa
Maximal stretch	λ_{max}	1.1

3.3 Results and Discussion

The effects of MEF on the APD and CV restitution properties, and its roles on transition from concordant to discordant alternans, discordant alternans, and on conduction block are described in the sections III A–III D.

3.3.1 Effects of MEF on the APD and CV restitution properties

We applied our FOXNHS model to study the effects of MEF on APD and CV restitution curves. APD restitution is determined using a dynamic pacing protocol, which increases the pacing rate by progressively reducing the BCL. Therefore, the cable was paced in the middle for 400 beats until a steady state is reached, starting at BCL = 600 ms and gradually decreasing to BCL = 190 ms. Figure 3.1 shows the APD dynamic restitution curve for FOXNHS model for different values of G_s. The APD was

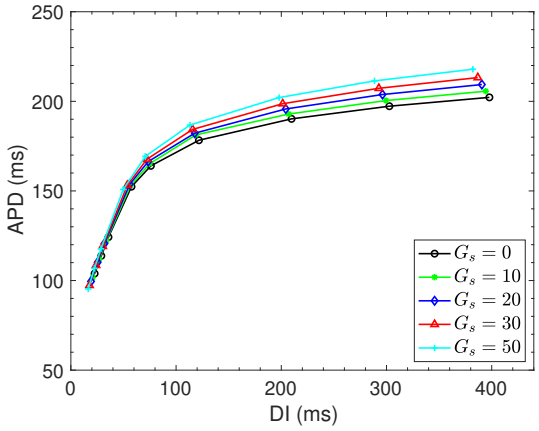

Figure 3.1: Dynamic restitution curves plotting APD_{90} against the preceding DI for the middle cell in FOXNHS model for different values of G_s. The 7 cm cable was paced at the middle at an initial BCL of 600 ms for a period of 300 beats. BCL was then reduced by 100 ms and cable was paced for a further 300 beats. This process was repeated but each time BCL is reduced by 100 ms if it is greater than 300 ms, by 10 ms if it is greater than 250 ms, and by 1 ms if it is greater than 210 ms.

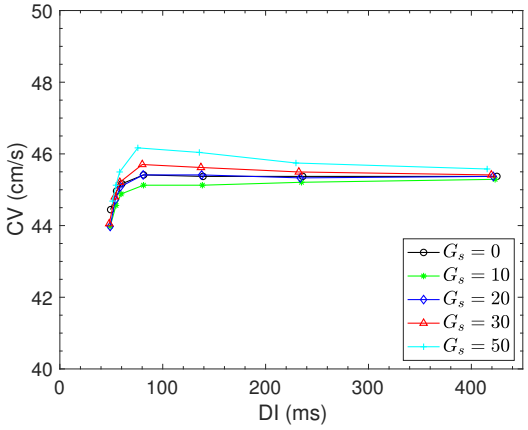

Figure 3.2: The CV restitution curves of the FOXNHS model for different values of G_s using a dynamic pacing protocol. CV was measured from the difference in front arrival times between two nodes, one is located at 0.5 cm from the PS, and the other at 1 cm further in propagation direction of a cable of length $L = 7$ cm.

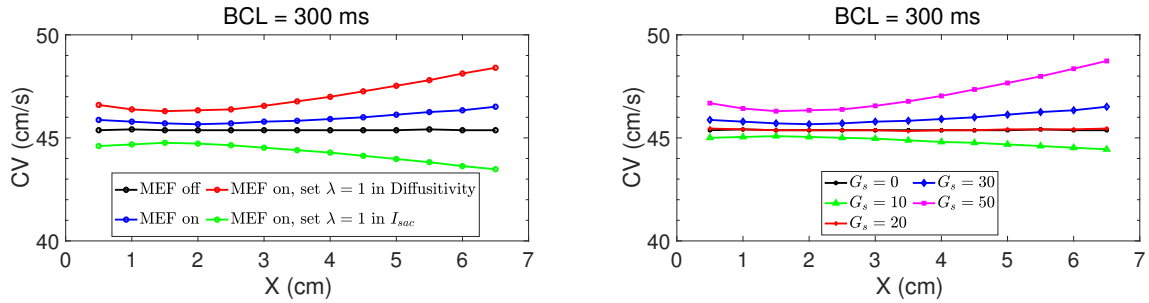

Figure 3.3: CV vs X (distance) along a 7 cm cable of the FOXNHS model, calculated for a BCL of 300 ms under four situations of MEF (left) and for different values of G_s (right).

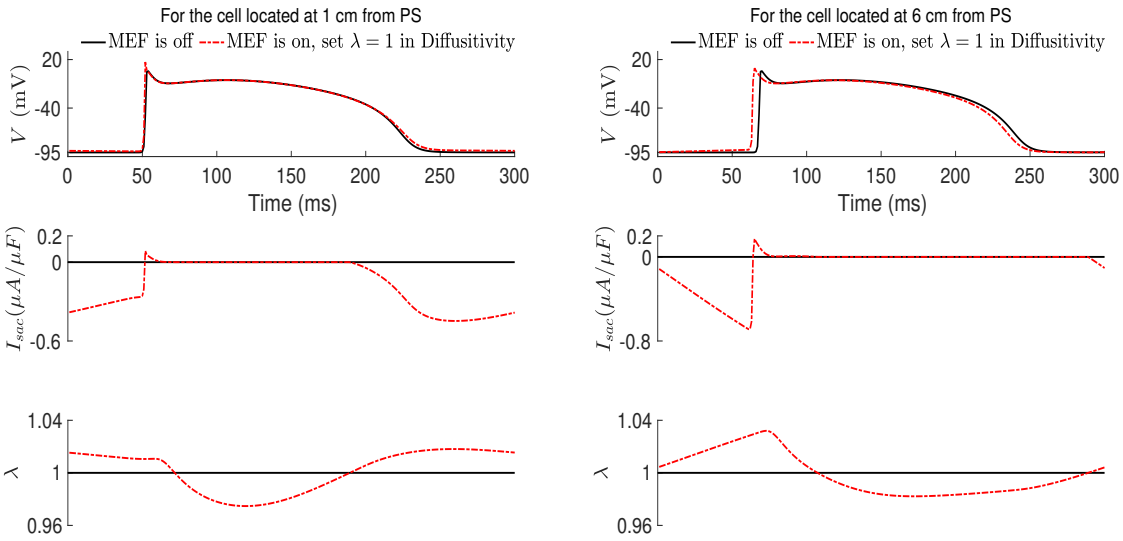

Figure 3.4: Time evolution of V (top), I_{sac} (middle), and λ (bottom) for the cells positioned 1 cm (left) and 6 cm (right) from the PS, of the FOXNHS model when MEF is off (black solid lines) and when MEF is on, and $F = 1$ in the stretch-dependent conduction in Eq. (3.1) (red dashed-dotted lines), and for $G_s = 50$ μS/μF, when a 7 cm cable is paced at the boundary with BCL = 400 ms and decreased gradually to BCL = 300 ms, and then paced periodically with BCL = 300 ms until a steady state is reached.

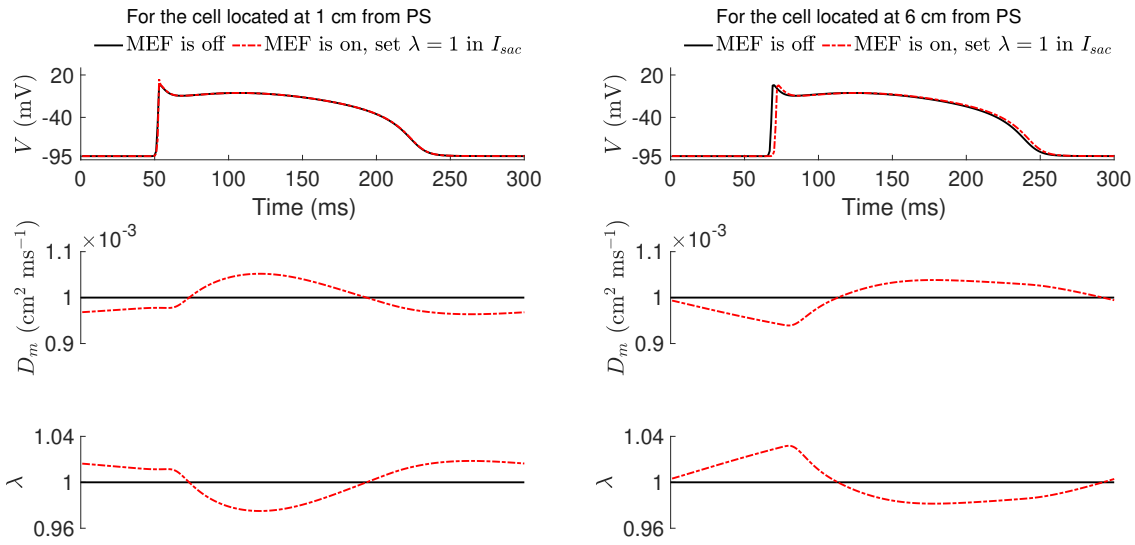

Figure 3.5: Time evolution of V (top), D_m (middle), and λ (bottom) for the cells positioned 1 cm (left) and 6 cm (right) from the PS, of the FOXNHS model when MEF is off (black solid lines) and when MEF is on, and $\lambda = 1$ in I_{sac} (Eq. (3.7)) (red dashed-dotted lines) when a 7 cm cable is paced at the boundary with BCL = 400 ms and decreased gradually to BCL = 300 ms, and then paced periodically with BCL = 300 ms until a steady state is reached.

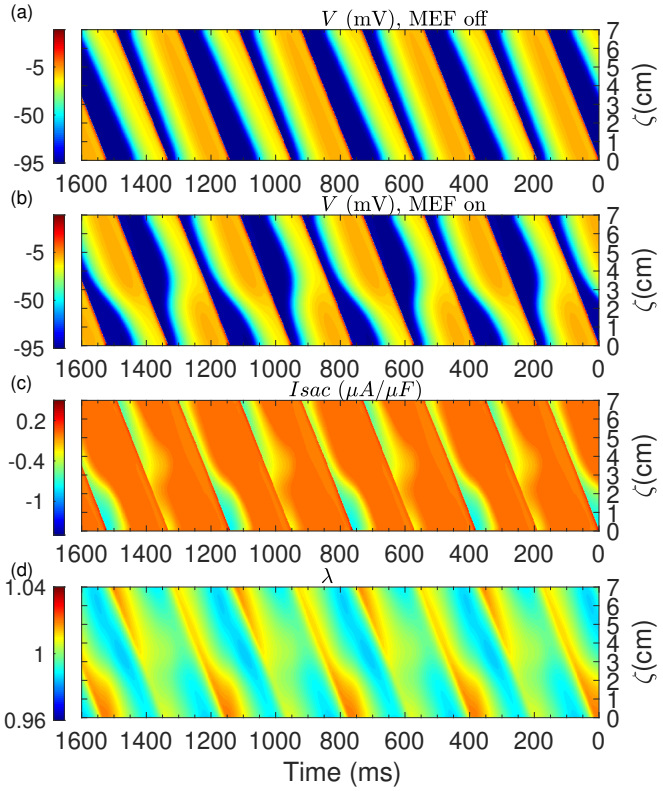

Figure 3.6: Spatiotemporal evolution of V when MEF is off (a), and on (set G_s = 50 μS/μF) (b), I_{sac} (c), and λ(d) in the FOXNHS model for several beats at steady state when a 7 cm cable of cardiac cells is paced at the boundary with BCL = 190 ms (starting at BCL = 400 ms, and decreased gradually to BCL = 190 ms).

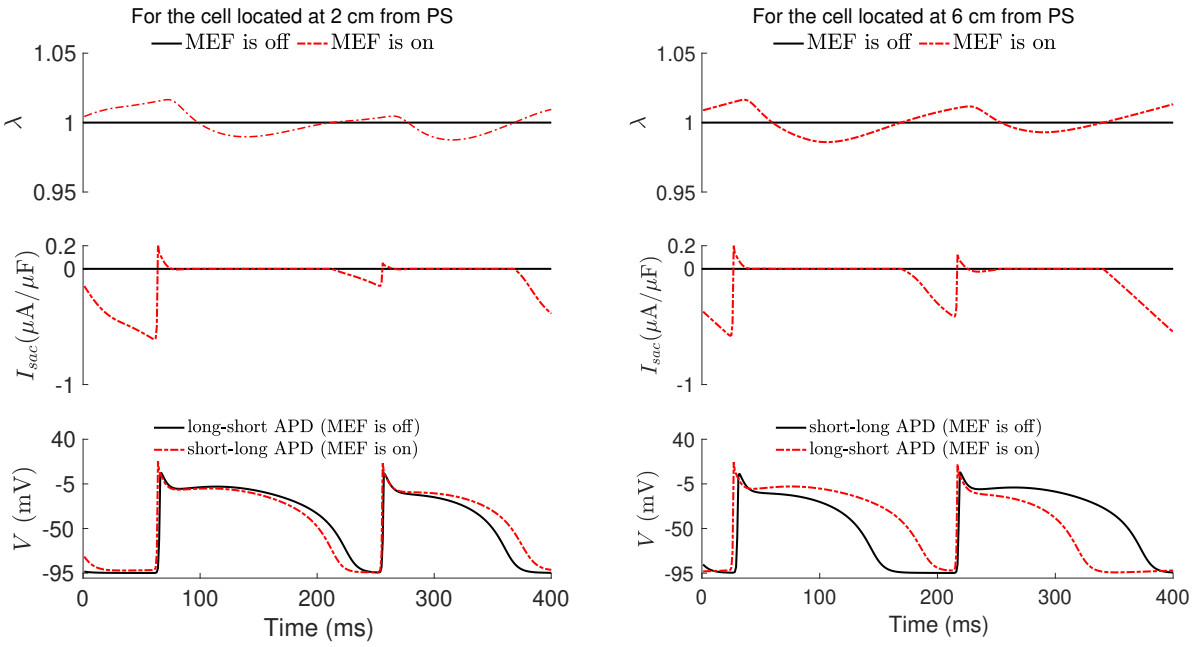

Figure 3.7: Time evolution of V (bottom), I_{sac} (middle), and λ (top) for the cells positioned 2 cm (left) and 6 cm (right) from the PS, of the FOXNHS model for $G_s = 0$ μS/μF (MEF is off; black solid line) and for $G_s = 50$ μS/μF (MEF is on; red dashed-dotted line), when a 7 cm cable is paced at the boundary with BCL = 400 ms and decreased gradually to BCL = 190 ms, and then paced periodically with BCL = 190 ms until a steady state is reached.

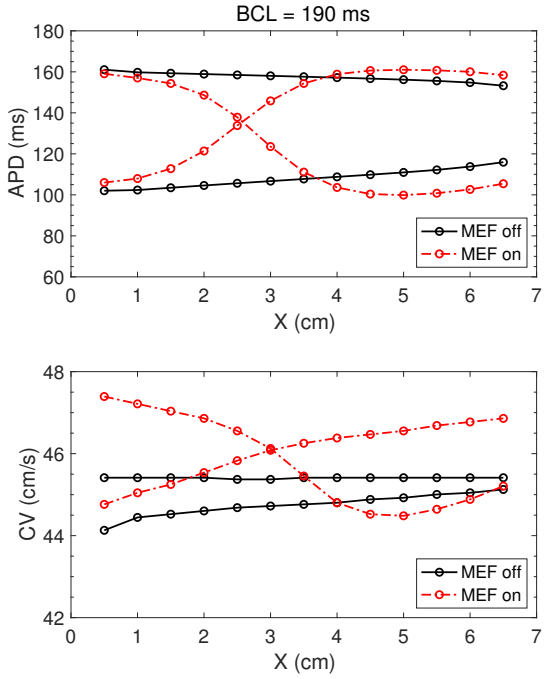

Figure 3.8: APDs (top) and CVs (bottom) vs X (distance) along a 7 cm cable of the FOXNHS model, for the same two consecutive beats at steady state, calculated for a BCL of 190 ms and when MEF is off (black solid lines) and MEF is on (red dashed-dotted lines).

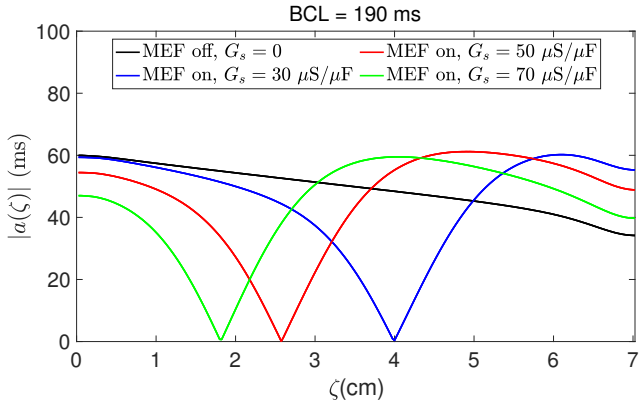

Figure 3.9: Magnitude of the amplitude of alternans for the FOXNHS model for different values of G_s, when a 7 cm cable is paced at the boundary with BCL = 400 ms and decreased gradually to BCL = 190 ms, and then paced periodically with BCL = 190 ms until a steady state is reached. APD90 (APD at 90 % repolarization) was adopted as a measure of APD.

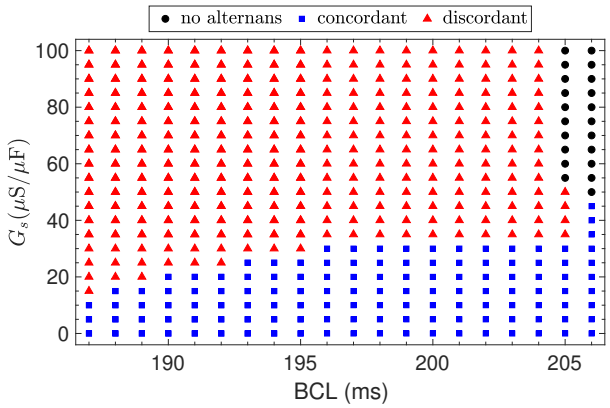

Figure 3.10: Plot showing the different patterns of alternans that are formed due to the I_{sac} in the plane of G_s and BCL, when a 7 cm cable is paced at the boundary with BCL = 400 ms and decreased gradually to a BCL in the range of 187-206 ms (which correspond to concordant alternans when no MEF is present) until a steady state is reached. As shown, the formed patterns are no alternans (black circles), concordant alternans (blue squares), and discordant alternans (red triangles).

measured at 90 % repolarization (APD_{90}) and the APD restitution curve was obtained by plotting the values of APD_{90} against the variant values of DI at steady states for the cell in the middle of the cable. As can be seen in this figure, MEF changes the APD restitution curve when BCL is greater than 210 ms, which corresponds to DI close to 60 ms. APD is increasing continuously for longer BCL, however, after BCL = 210 ms the increase is higher for larger value of G_s. On the other hand, and for the same values of BCL and G_s, APD decreases when $|E_s|$ is increased, and no effect of MEF on the APD restitution (results not shown) is observed for $|E_s| >= 20$ mV. Note that the effect of MEF on the APD restitution depends on the cell's position within the 1D tissue, since the stretching is not uniform along the cable (see [115]) and therefore, the effects of MEF on the onset of alternans in the 1D tissue may also depend on the location of the pacing domain (which means it depends on whether the cable is paced in the middle or at the boundary). For the FOXNHS model the onset of alternans occurs when the 1D cable is paced, at the leftmost boundary, at BCL = BCL_{crit} = 206 ms (BCL_{crit} is the maximum BCL at which alternans occurs when MEF is not present) if the cable is paced at the boundary and when MEF is not present. However, in the presence of MEF, and for a certain range of G_s, the BCL that corresponds to the onset of alternans can be decreased, as described in Sec. III

B.

To study the influence of MEF on the CV restitution, we determine the CV for various values of G_s using a similar dynamic pacing protocol. To this end, the cable was paced at its boundary for 400 beats until its steady state is reached. The CV was measured at steady state for each BCL as the distance between two points, positioned at 0.5 cm and 1 cm from the pacing site to avoid boundary effects [120, 121], divided by the front arrival times between these points. The effect of MEF on the CV restitution for different values of G_s is given in Fig. 3.2. We see from this figure, that CV is monotonically increasing with DI for G_s less than 20 μS/μF, but it exhibits a biphasic shape when G_s is greater than 20 μS/μF, increasing with BCL till BCL = 300 ms, which corresponds to DI close to 80 ms, then decreasing afterwards. However, since the stretch distribution is not uniform along the cable and that it varies with BCL [115], therefore, the effects of MEF on CV restitution depends on the position of the two points in the 1D cable where CV is measured, and thus we calculated the CV along the cable for the FOXNHS model, without and with the presence of MEF, for BCL = 300 ms. Thus, four different situations of MEF were considered: (1) stretch-dependent conduction is only present (i.e. set $\lambda = 1$ in I_{sac} (Eq. (3.7))), (2) stretch-activated current is only present (i.e. set $F = 1$ in the stretch-dependent conduction in Eq. (3.1)), (3) in the presence of both stretch-activated current and stretch-dependent conduction, and (4) in the absence of both stretch-activated current and stretch-dependent conduction (i.e. set $F = 1$ in the stretch-dependent conduction in Eq. (3.1) and set $\lambda = 1$ in I_{sac} (Eq. (3.7))). To this end, we divided the cable, between the positions X = 0.25 cm and X = 6.75 cm, into 13 segments of equal sizes, then we computed CV between the endpoints of each segment, and the measured CV is plotted versus the midpoint of each segment (left of Fig. 3.3). As one can see, the change on diffusivity (due to stretch; situation (1)), when comparing with the situation (4) (i.e. when MEF is off), is decreasing the velocity of propagation of the wave along the cable. However, in situation (2) (only I_{sac} is present), the velocity of propagation of the wave is increased along the cable, although the increase is not monotonic: there is a minimum around X = 1.5 cm. In the presence of both I_{sac} and stretch-dependent conduction, the velocity along the cable is increasing, since the increase on CV, due to I_{sac}, is greater than the decrease on CV, due to stretch-

dependent conduction. To measure the effect of the strength of the I_{sac} on CV, we repeated the situation (3) for different values of the conductance parameter G_s (right of Fig. 3.3). As can be seen in this figure, CV is decreased, when comparing with situation (4), when $G_s < 20$ μS/μF and increased when $G_s >= 20$ μS/μF since, as described earlier, the effect of I_{sac} on CV becomes more dominant than the effect of stretch-dependent conduction on CV.

In the following, we describe the effects of the stretch-dependent conduction on CV that corresponds to situation (1) and the effects of the I_{sac} on CV that corresponds to situation (2). For simplicity, we approximate the diffusion rates of the V (Eq. (3.1)) by moving the term $1/F$ outside the derivative operator so that the effects of deformation on the conductivity and the corresponding diffusion coefficient D can be expressed by $D_m(\lambda) = D/F^2 = D/\lambda^2$. This means that a change of the conductivity, due to λ, is assumed to be caused by a dependence of the new diffusion variable D_m on the stretch ($D_m(\lambda)$). To describe the effects of I_{sac} and D_m on CV, (λ, I_{sac}, V) and (λ, D_m, V) were plotted simultaneously at steady state for BCL = 300 ms in Figs. 3.4 and 3.5 for two cells located at different positions, one located at 1 cm from the PS (left of Figs. 3.4 and 3.5) and the other one located at 6 cm from the PS (right of Figs. 3.4 and 3.5). We first investigate the effects of I_{sac} on CV. As shown in Fig. 3.4(left), the I_{sac} increases the CV, since at resting potential and just before the depolarization, the I_{sac}, which is an inward current, increases slightly the resting potential and this causes a stronger depolarization effect. At late repolarization, the I_{sac}, which is also here an inward current, produces a depolarizing effect delaying slightly the repolarization process. The strength of I_{sac} for the cell2 (right of Fig. 3.4), is larger than the one of the cell1 (left of Fig. 3.4), and therefore the depolarizing effect of the I_{sac} on the AP of the cell2 is stronger than the depolarizing effect of the I_{sac} on the AP of the cell1. At late repolarization for the case of cell2, I_{sac} is null since λ is contracting ($\lambda < 1$), and therefore, the I_{sac} has no effect on the AP. Note that, the increase in CV as shown in Fig. 3.4(right) is not only due to I_{sac} of the cell2, but we need also to account for the increase of the CV that occurred when the wave propagates a 6 cm along the cable, from the PS to cell2. We now investigate the effects of $D_m(\lambda)$ on CV. It is known that a change of the Diffusivity, modifies the CV of propagation of the wave. As shown in left and right of Fig. 3.5, and at

depolarization phase of the AP, λ is stretching ($\lambda > 1$), which gives us $D_m(\lambda) < D$, this causes a decrease in the velocity of the wave. On the other hand, the stretching of cell2 at the depolarization phase of the AP is higher than the stretching of cell1, therefore the decrease in the velocity of the wave at cell2 (right of Fig. 3.5) is higher than the decrease in the velocity of the wave at cell1 (left of Fig. 3.5). Also here, we need to take into account the decrease of the CV that occurred when the wave propagated from the PS to cell2.

3.3.2 Role of MEF on the transition from concordant to discordant alternans

For the FOXNHS model, the APD alternans can be induced in the 1D cable, when it is paced at the boundary with BCL <= BCL_{crit} = 206 ms. Moreover, when MEF is not present, the SCA occurs in the FOXNHS model, when it is paced at any BCL between 187 ms and 206 ms, and the SDA occurs when BCL is less than 187 ms. To illustrate the effect of MEF on the SCA, two conditions were considered: without and with the presence of MEF. For the first condition, a 7 cm cable of cardiac cells of the FOXNHS model was paced at the leftmost boundary, starting at BCL = 400 ms and gradually decreasing to BCL = 190 ms until a steady state is reached. The excited APs travel along the 1D cable in the space-time domain (Fig. 3.6(a); space goes from the bottom to the top and in time from the right to the left). As shown in this figure, a large AP is being followed by a small one showing SCA. However, in the presence of MEF (G_s is set to 50 μS/μF) and when similar actions were performed, the SDA arises (Fig. 3.6(b)), where tissue region close to the PS, up to approximately 2.6 cm, showing a pattern of large-short for APDs while the other parts (after 2.6 cm) showing a pattern of short-large. Figs. 3.6(c) and 3.6(d) shows the spatio-temporal of I_{sac} and λ respectively, under the second condition (i.e. when MEF is present). One can conclude that MEF has a role in converting the SCA into SDA. To investigate the role of I_{sac} in this conversion, λ, I_{sac}, and V were plotted simultaneously in Fig. 3.7, for two cells, namely cell1 and cell2, in the cable (cell1 is located at 2 cm from the PS, and cell2 is located at 6 cm from the PS). As shown in Fig. 3.7, an alternation in the APD induces an alternation in λ (large-small) and consequently an alternation in I_{sac} for the same cell in the cable. Therefore, the depolarizing effect of the I_{sac} on

the AP is stronger when λ is large, and for the case of cell1 (left of Fig. 3.7), the increase in the CV for the long APD is greater than for the short APD, however, for the case of cell2 (right of Fig. 3.7), the increase in the CV for the short APD is greater than for the long APD. Note that although I_{sac} has a slight depolarizing effect on the late repolarization for the long APDs of both cells, the dominant factor is its depolarizing effect at the depolarization phase, and that an increase in the short APD causes, according to the restitution relation, a decrease in the long APD and vice versa. Since the distribution of λ is not uniform along the cable length (Fig. 3.6(d)), the effects of I_{sac} (Fig. 3.6(c)), which depends on λ and V, on CVs were not equal for all cardiac cells along the cable. To illustrate the variation of CV in the cable and its influence on APD, the CVs and APDs for two consecutive beats at steady state were plotted simultaneously in Fig. 3.8. When MEF is not present, a SCA is formed, which corresponds to an oscillation of large and short APDs that are correlated respectively with greater and smaller CVs. However, when MEF is present, a transition from SCA to SDA is induced, which is mainly due to the effect of I_{sac} via its influence on the CV. As shown in Fig. 3.8(top), when the two dot-dashed lines intersect at a point (called nodal point and is located at approximately 2.6 cm from the PS), the long and short APDs become equal, and this marks the division of two out-of-phase regions. The position of the nodal point depends on the strength of I_{sac}, which can be regulated by the value of G_s, and its effects on CVs. Fig. 3.9 illustrates the effects of the strength of I_{sac} on the position of the nodal point, which moves towards the PS when G_s is increased. Depending on the BCL applied, the strength of I_{sac} that is required to cause a transition from SCA to SDA varies, see Fig. 3.10. As shown in this figure, G_s is decreased when BCL is decreased for the transition from SCA to SDA to occur.

3.3.3 Role of MEF on discordant alternans

The effect of MEF on SCA is illustrated here with the same conditions considered in the previous section. We start by inducing discordant alternans in the FOXNHS model when MEF is not present, therefore, a 7 cm cable of cardiac cells was paced at the leftmost boundary, starting at BCL = 400 ms and gradually decreasing to BCL = 180 ms until a steady state is reached. When MEF is not present, the SDA can be

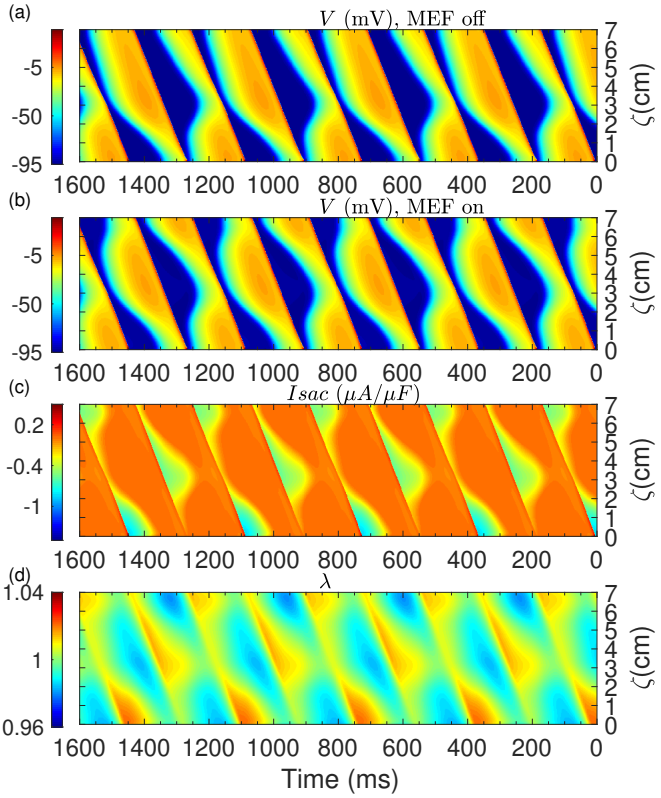

Figure 3.11: Spatiotemporal evolution of V when MEF is off (a), and on (b), I_{sac} (c), and λ (d) in the FOXNHS model for $G_s = 50$ μS/μF and for several beats at steady state when a 7 cm cable of cardiac cells is paced at the boundary with BCL = 180 ms (starting at BCL = 400 ms, and decreased gradually to BCL = 180 ms).

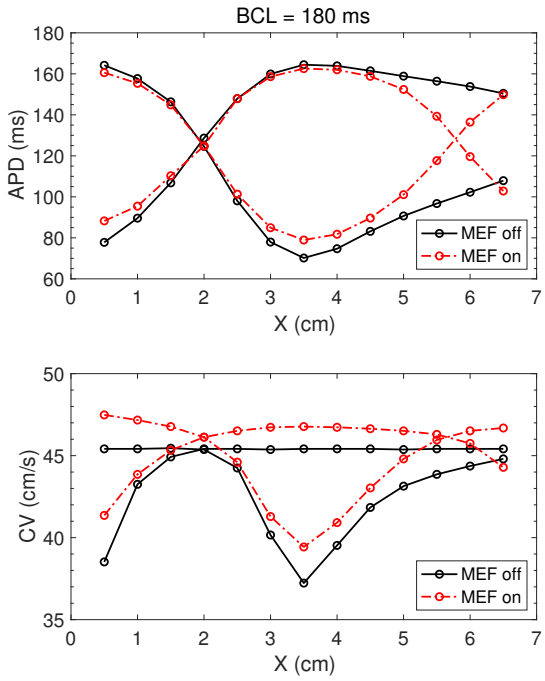

Figure 3.12: APDs (top) and CVs (bottom) vs X (distance) along a 7 cm cable of the FOXNHS model, for the same two consecutive beats at steady state, calculated for a BCL of 180 ms and when MEF is off (black solid lines) and MEF is on (red dashed-dotted lines)

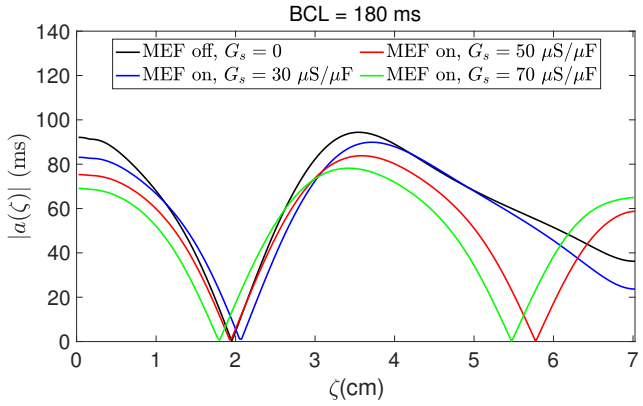

Figure 3.13: Magnitude of the amplitude of alternans for the FOXNHS model for different values of G_s, when a 7 cm cable is paced at the boundary with BCL = 400 ms and decreased gradually to BCL = 180 ms, and then paced periodically with BCL = 180 ms until a steady state is reached. APD90 (APD at 90 % repolarization) was adopted as a measure of APD.

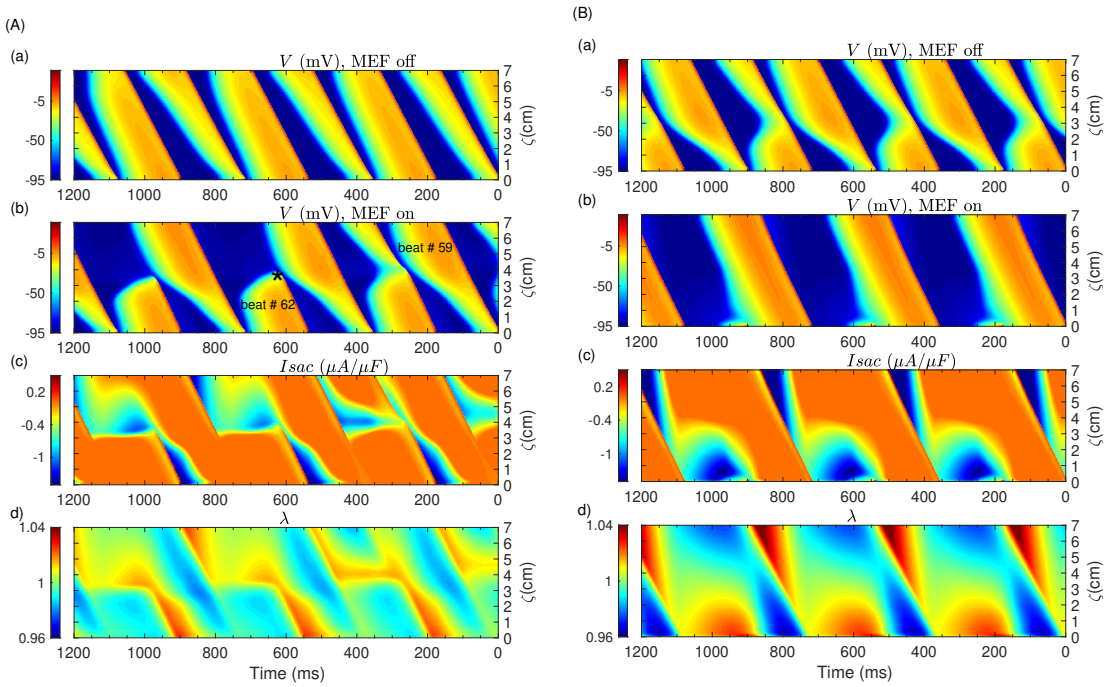

Figure 3.14: Spatiotemporal evolution of V when MEF is off (a), and on (b), I_{sac} (c), λ in the FOXNHS model for $E_s = 0$ ms and $G_s = 80$ μS/μF and for several beats at steady state when a 7 cm cable of cardiac cells is paced at the boundary with BCL = 180 ms (starting at BCL = 400 ms, and decreased gradually to BCL = 180 ms). Plots were generated at time $t_1 = 19060$ ms, which corresponds to beat number 62 (A), and at steady state (B).

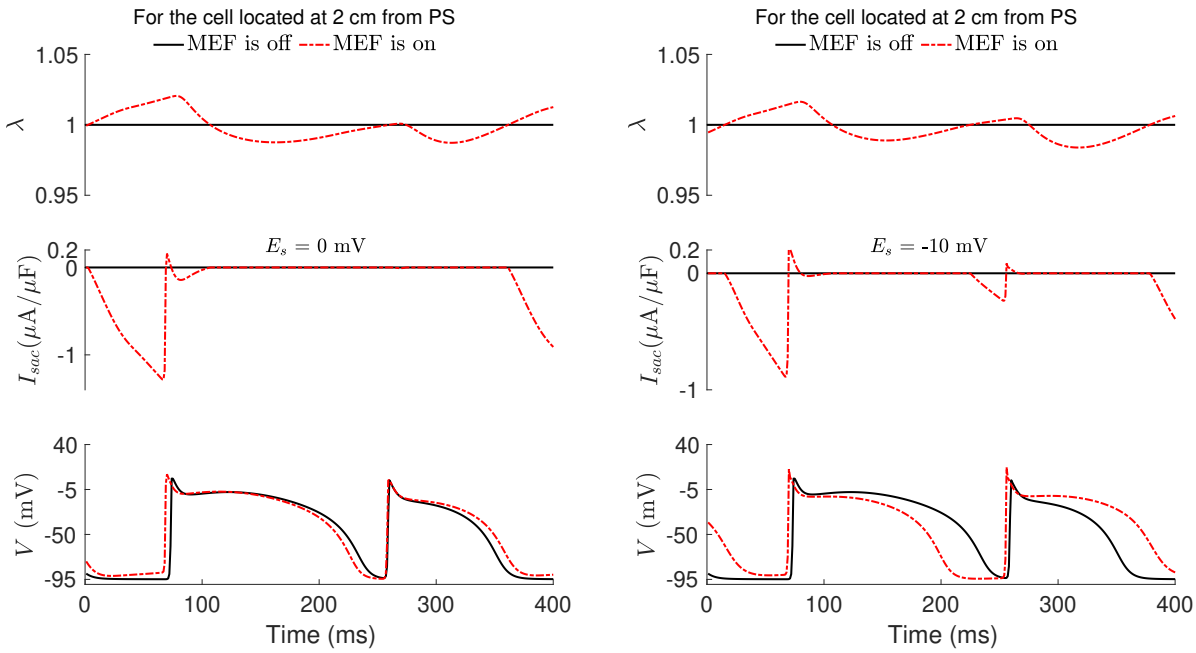

Figure 3.15: Time evolution of V (bottom), I_{sac} (middle), and λ (top) for the cell positioned 2 cm from the PS, of the FOXNHS model for $G_s = 80$ μS/μF and $E_s = 0$ mV (left) and E_s = -10 mV (right), when a 7 cm cable is paced at the boundary with BCL = 400 ms and decreased gradually to BCL = 180 ms. Only, the corresponding V, I_{sac}, and λ for the beats 60-61 are illustrated.

induced in the FOXNHS model when pacing at any BCL between 186 ms and 178 ms. The FOXNHS model was paced again using the same pacing protocol but this time in the presence of MEF (G_s is set to 50 μS/μF). The V, λ, and I_{sac} at steady state and under the two conditions (without and with the presence of MEF) were plotted simultaneously in Fig. 3.11. As shown in Fig. 3.11(b), the spatial dispersion of repolarization was increased in the presence of MEF when compared to alternans repolarization without the presence of MEF (Fig. 3.11(a)). As shown in this figure, the SDA has a nodal point formed at approximately 2 cm from the PS, where the alternation of APDs in the region of the cable from the PS to this nodal point is manifested as long-short, while the alternation of the APDs in the region after this point is manifested as short-long pattern. One can also see that in the presence of MEF, the number of nodal points (two nodes were formed) was increased where the second node was formed at approximately 5.8 cm from the PS. In Fig. 3.11(b), the APDs alternate as a pattern of short-long in the region between the two nodes and as a pattern of long-short in other regions (one from the PS up to approximately 2 cm and the other from approximately 5.8 cm to the end of the cable). Figure 3.12 illustrates the variation of the CV and its influence on APD along the cable, with and without the presence of MEF, for two consecutive beats at steady state. As shown in this figure, the CV was increased globally, when compared with the one without MEF, for both short and long APDs along the cable up to approximately 5.4 cm from the PS. Due to I_{sac}, the CV of large (small) APD is decreasing (increasing) in the cable from the PS up to the first node located at approximately 2 cm from the PS. This node almost coincide with the one that is formed when MEF is not present. The previously long (short) APD becomes short (long) APD in the cable between the first and the second node located at approximately 5.8 cm from the PS. Between these nodes, the CV of long (short) is increasing (decreasing) till approximately the middle of the cable, then decreasing (increasing) till the second node. The CV of the small APD starts to increase significantly after the AP travels 5 cm from the PS. Consequently, the small APD starts to increase significantly and causes the long APD to decrease according to the restitution relation until the second node is formed at approximately 5.8 cm from the PS. Varying the G_s, which regulates the strength of I_{sac}, affects the formation of the nodes and their positions (Fig. 3.13). As shown in this figure, for

$G_s = 30$ μS/μF, no additional nodes are formed to the already existing node when MEF is not present. However for the values of G_s equal to 50 μS/μF or 70 μS/μF a second node is formed closer to the other end of the cable, and moves more towards the pacing site when G_s is greater. Although the degree of APD oscillation is greater when MEF is applied, the magnitude of the amplitude of alternans is decreased. Note that, it is shown in Fig. 3.13 that the additional node is formed at approximately 5.8 cm from the PS, however in Fig. 3.12, it is shown that is formed at approximately 5.6 cm. This difference is due to the accumulation of errors accrued along all segments in which the CVs were computed, because, the distance between the two points of a segment in which the CV was computed is not small enough so that the local error remains small.

3.3.4 Role of MEF on conduction block

To investigate the role of MEF on the threshold of conduction block (CB), we performed the following steps. First, we determined the CB threshold without the presence of MEF. Therefore, a 7 cm cable of cardiac cells of the FOXNHS model, when MEF is off, was paced at the leftmost boundary, starting at BCL = 400 ms and gradually decreasing to BCL = 200 ms until a steady state is reached. If CB did not occur, the same operation was repeated but every time BCL was decreased 1 ms until CB occurred. The CB was observed when BCL = $\text{BCL}_{\text{thresMEFoff}}$ = 177 ms, where $\text{BCL}_{\text{thresMEFoff}}$ is the smallest BCL under which CB occurred for this model when MEF was not present. In the presence of MEF, the same steps were repeated for three different setting of E_s (namely $E_s = 0$ mV, -10 mV, and -20 mV) of the I_{sac} model. For every setting of E_s, different values of G_s between 0 and 100 μS/μF were also considered. We observed that only when $E_s = 0$ mV and for $G_s >= 80$ μS/μF, the threshold of CB was shifted 3 ms to higher BCLs, this means that BCL = $\text{BCL}_{\text{thresMEFon}}$ = 180 ms, where $\text{BCL}_{\text{thresMEFon}}$ is the smallest BCL under which CB occurred for this model when MEF was present. As shown in Fig. 3.14(A), CB occurred when beat number = 62 and kept occurring till a steady state was reached at beat number = 400 (Fig. 3.14(B)). In one direction, changing E_s can modify the magnitude and sign (inward or outward) of I_{sac}, which can have an effect on the APDs. In the other direction, variations in the APDs can change the mechanical stretch, and this in turn can mod-

ify the magnitude of the I_{sac}. For example for the node located at 2 cm from the PS, the variations of mechanical stretch are not identical for the two values of E_s (Fig. 3.15). In addition, the magnitude and sign of I_{sac} are also not the same. For the case of E_s = 0 mV (left of Fig. 3.15) and at the beat number 60, the magnitude of the I_{sac}, which is an inward current before the depolarization phase, is larger than the one shown in Fig. 3.15(right) (the case of E_s = -10 mV), and at early repolarization, I_{sac} was an outward current and became an inward for the case of E_s = 0 mV, while for the case of E_s = -10 mV, it became zero. We previously showed that the I_{sac} magnitude, sign, and timing play a significant role in the dispersion of repolarization via its influence on the CV dispersion. Figure 3.16 illustrates the effects of E_s on the dispersion of CV. As seen in this figure, for E_s = 0 mV the CV along the cable was changed, when compared with E_s = 0 mV, for beats 5, 40, and 52 which correspond to BCL = 390 ms (no alternans), BCL = 197 ms (concordant alternans) and BCL = 185 ms (discordant alternans). At beats 60 and 61 which correspond to BCL = 180 ms, E_s = 0 mV the dispersion of CV was increased significantly and resulted in CB at beat 62.

3.4 Conclusions

In this work, we studied the effects of MEF on the dynamics of alternans using a 1D biophysically detailed electromechanical model of cardiac tissue. Numerical simulations were performed for a range of BCLs and for different values of the I_{sac} model parameters, namely G_s and E_s, where I_{sac} is the main effects of MEF on excitation. We found that MEF may play a role in arrhythmogenesis. We showed that MEF, depending on the strength of I_{sac}, can increase the dispersion of repolarization via its influence on the dispersion of CV. In particular, it was illustrated that I_{sac} can induce the transition from spatially concordant alternans to spatially discordant alternans when the strength of I_{sac} is sufficiently large, and that the dispersion of refractoriness is increased, if the existing state of alternans is discordant, when G_s is increased. This is mainly due to the effects of I_{sac} on CV of the electrical wave, where the spatial variations in CV is increased with the increase of G_s. We also found that the onset of CB can be shifted to a lower pacing rate for some setting

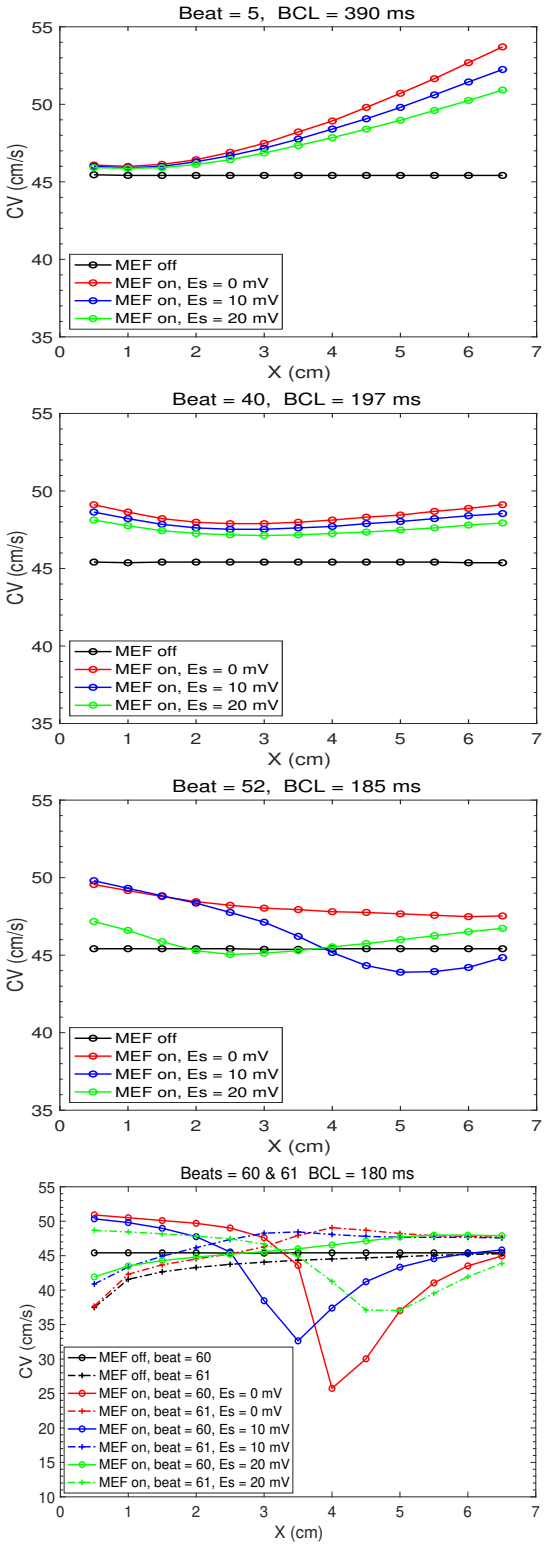

Figure 3.16: CV vs X along a 7 cm cable of the FOXNHS model when MEF is off and MEF is on (with $G_s = 80$ μS/μF, and for three different values of E_s, which are 0, -10, and -20 mV), calculated at beats 5 (top left), 40 (top right), 52 (bottom left), and 60-61 (bottom right).

of the parameters of the I_{sac} model. This is the case when $E_s = 0$ mV and for $G_s \geq 80$ μS/μF, the threshold of CB can be shifted up to 3 ms. This is because, for these given values, the contribution of I_{sac} in the dispersion of CV is significant that can result in localized block.

Chapter 4

Control of cardiac alternans in an electromechanical model of cardiac tissue

4.1 Introduction

Electrical alternans is a physiological phenomenon manifested as beat-to-beat oscillation (electric wave width alternation) of the cardiac Action Potential Duration (APD) [3]. Alternans has been shown to be a precursor to arrhythmias [2, 122] and sudden cardiac death (SCD), which is the most common cause of death in the industrialized world. Experimentally, APD alternans is observed during pacing at high rates so that beyond a critical pacing value a sequence of long and short APDs emerges [123] as presented in Fig. 4.1. In this figure, APD is defined as the period of time during which the action potential exceeds the given threshold value, while a diastolic time interval (DI) is defined as the period of time during which the action potential is below the threshold value.

The majority of feedback control algorithms [16, 17, 18, 19, 20, 21] that have been developed until now to suppress alternans in cardiac tissue utilize the difference between the measurements of the two most recent APDs to make small adjustments to the timing of electrical stimuli. These algorithms are specific implementations of time-delay auto-synchronization [22] and extended time-delay auto-synchronization [23] feedback control techniques. Hall *et al.* [16] used this approach to successfully control cardiac arrhythmia called an alternans rhythm in an *in vitro* rabbit heart. Similarly, Rappel *et al.* [17] suppressed alternans in two geometrical models of both

1D and 2D tissues, to conclude that several control electrodes need to be placed on the tissue in order to stabilize normal heart rhythm. Control of atrioventricular-nodal conduction alternans has also been demonstrated *in vivo* human hearts [18] by stabilizing the underlying unstable steady-state conduction. The first experimental attempt to implement the electrical pacing interval technique is due to Hall and Gauthier [20], who succeeded in suppressing alternans in small pieces (< 1 cm) of a bullfrog cardiac muscle. Echebarria and Karma [19] were the first to investigate this approach theoretically in a model of Purkinje fibers. They showed, by using Noble model, that alternans in fibers no longer than ≈ 1 cm could be suppressed using single electrode. Their theoretical results were experimentally verified by Christini *et al.* [21]. In addition, Dubljevic *et al.* [24] proved regarding the stated approach, that the failure to suppress alternans completely in tissues exceeding 1 cm in length is due to the lack of information of the spatial evolution of alternans away from the pacing site, and due to finite controllability of actuation at the pacing site.

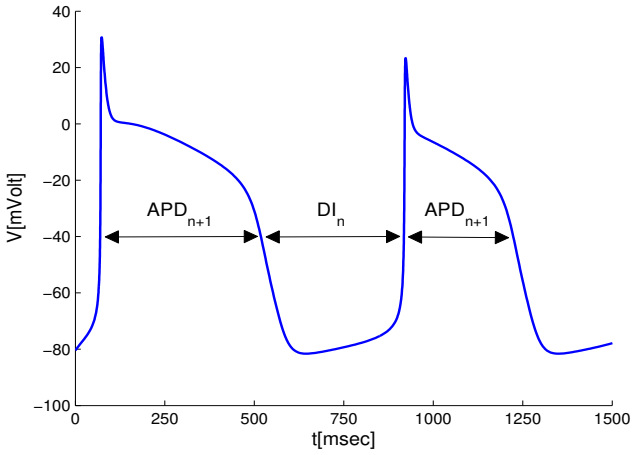

Figure 4.1: Time evolution of transmembrane potential in the Noble cardiac cell model.

It has been shown theoretically and experimentally that the above mentioned control technique has a finite degree of controllability, such that alternans stabilization in cardiac tissues of the length above 1 cm cannot be achieved [19, 21, 24, 25]. Although such algorithms have proved effectiveness of controlling electrical alternans in small tissues, several electrodes need to be implanted along the length of cardiac

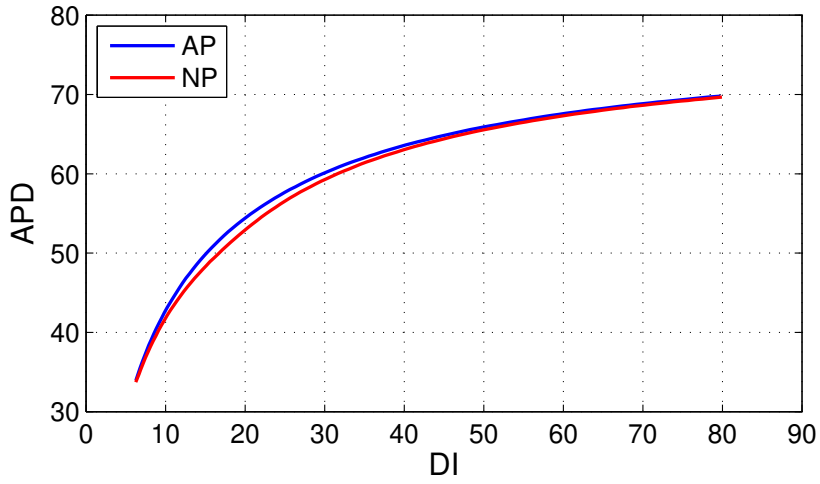

Figure 4.2: The dynamic APD restitution curves for the AP and NP models.

tissue ($\approx$ 6.25 cm), so that each pacing electrode can suppress alternans in a finite part of the tissue ($\approx$ 1 cm). In addition, to the authors' best knowledge, all the electric-based realization algorithms have not take into account mechanical properties of cardiac tissue, despite the fact that mechanical deformation is shown to influence electrical activity of the heart tissue, and consequently the cardiac alternans. In fact, cardiac electrical waves propagate through cardiac tissue and initiate its contraction via excitation-contraction coupling (ECC), while contraction of the heart causes cardiac tissue deformation which in turn feeds back on the wave propagation and affects electrophysiological properties via mechanoelectrical feedback (MEF) [124, 6, 7, 125].

Many studies have shown the importance of the MEF and, for instance, that

Table 4.1: Parameter values for the electromechanical model employed for small deformation

$k = 8$	$a = 0.05$	$\varepsilon = 0.1$	$\mu_1 = 0.12$
$\mu_2 = 0.3$	$k_{Ta} = 0.01$kPa	$\tilde{c} = 16$kPa	$G_s = 1.6$

mechanical impact on the chest, in the area directly over the heart, can either cause Commotio Cordis, when the chest receives a blow [126, 127], or terminate cardiac

arrhythmia by striking a blow of the fist to the chest in a precordial thump [128, 129]. Therefore, in this paper, we explore the feasibility of controlling electrical alternans by manipulating mechanical properties of the cardiac tissue. From mathematical point of view, electromechanical models where the coupling between electrical and mechanical activity of the heart are more suitable for our study. A variety of these models has been developed to investigate various physical phenomena and they can be mainly classified into two categories. The weakly coupled electromechanical models [26, 27, 28, 29] that account only for the effects of electrical activity on the cardiac mechanics, i.e., one way coupling, and the strongly coupled electromechanical models [30, 31, 32, 33, 34] that account for the effects of electrical activity on the cardiac mechanics and the effect of mechanical deformation on electrical properties. For more details about the electromechanical models, the reader is referred to [35, 36]. In this work, we will use Nash-Panfilov (NP) model [30, 31], which is a strongly coupled electromechanical model. This model includes an additional variable to link the electrophysiological properties of the heart tissue which is modelled with the well-known Aliev-Panfilov (AP) model [46], with cardiac tissue's mechanical properties. It has been shown in [123] that APD alternans occurs when the slope of the dynamic APD restitution curve is greater than one. Therefore, for the NP model, APD alternans can be induced by pacing cardiac tissue at a rapid rate as the slope of the dynamic restitution curve (Fig. 4.2) at high frequencies is greater than one. The dynamic restitution curve, which describes the relationship between action potential duration (APD) and preceding diastolic interval (DI), was constructed using a dynamic pacing protocol [123] and determined by plotting each action potential duration at 90% repolarization against the preceding diastolic interval at incremental pacing rates. The dynamic restitution curve of the NP model is the dynamic restitution curve of the AP when coupled with cardiac contraction. As the NP model is dimensionless, units are not used, refer to section 4 for details, and the models' parameters used are given in Table 4.1.

The main goal of this paper is to show that the control of cardiac alternans along a 7 cm cable of cardiac cells can be achieved by control algorithms that use the mechanical perturbation approach. In particular, we consider several electrical pacing and mechanical perturbation strategies with two relevant mechanical deformations

being considered. The first one is in small deformation, and therefore the model is governed by the equations of the linear elasticity theory [50, 130]. Since the cardiac cells change length by up to 20%, which occurs as a result of cardiac contraction during a normal heart beat [27, 30, 131, 132], the second strategy is therefore when the deformation is large. The model in this case is however governed by nonlinear equations of the finite deformation elasticity theory [50, 130, 133].

It will be demonstrated that in small deformation, one can suppress alternans along the whole cable of cardiac cells by using mechanical perturbation strategy. The control algorithm proposed for the large deformation, which is an extension of the one used for small deformation, combines electrical boundary pacing and mechanical perturbation strategy. In all proposed algorithms, the electrical pacing is applied at the tissue boundary while the mechanical perturbation control is applied at one place over a small localized region within the cable length of 7 cm. Recently, mechanics-based devices have been developed that can be attached to the membrane of the heart to treat cardiac diseases [134]. The proposed control algorithm is a promising approach that can be possibly incorporated into mechanical-based devices that can be equipped with mechanical patch to apply mechanical perturbation over a small localized region of the heart tissue in order to suppress alternans. Applying this control strategy to control cardiac alternans can potentially improve therapy since it requires that one mechanical patch, in a one-dimensional model, to be placed over a small region (≤ 1 cm), to suppress alternans, while the existing electrical pacing control requires several electrodes to be implanted in the ventricles, which is very difficult to be realized, so that each pacing electrode should be able to suppress alternans over a finite area of cardiac tissue.

To the authors' best knowledge, these methods of control of alternans have not been explored in previous studies. Only Yapari *et al.* [97] used mechanical perturbation approach in their control algorithm to suppress electrical alternans under condition of small deformation, where the deformation gradient is simply approximated, and their proposed algorithm cannot be extended to higher spatial dimensions. To show the performance and efficiency of our methodology in suppressing alternans in the whole cable of cardiac cells for small and large deformations, numerical simulations will be presented.

4.2 Mathematical Model

Due to the fact that cardiac cells change length by up to 20% during a normal heart beat, the mechanical analysis in the NP model is based on the finite deformation elasticity theory for large deformation. However, for small deformation, the mathematical model of deformation can be reduced to a simplified one governed by the equations of the linear elasticity theory. The reader can refer to [50, 130, 133] for more details on linear and nonlinear elasticity theories.

4.2.1 NP Model

Nash-Panfilov model that couples cardiac excitation using a two variable Reaction-diffusion model with the equations that model the deformation of cardiac tissue is given by:

$$\frac{\partial V}{\partial t} = \bar{D}\frac{\partial}{\partial X_M}\left(\sqrt{C}C^{-1}_{MN}\frac{\partial V}{\partial X_N}\right) + f(V,r) \tag{4.1}$$

$$\frac{\partial r}{\partial t} = \left(\varepsilon + \frac{\mu_1 r}{\mu_2 + V}\right)(-r - KV(V-b-1)) \tag{4.2}$$

$$\frac{\partial T_a}{\partial t} = \epsilon(V)(k_{T_a}V - T_a) \tag{4.3}$$

$$\frac{\partial}{\partial X_M}(S^{MN}F_{jN}) = 0 \tag{4.4}$$

Where $f(V,r) = KV(V-a)(1-V) - rV - I_g$. All parameters and variables are dimensionless. V is the membrane potential, r is the recovery variable, and a is the threshold parameter. $\bar{D} = 1$ is the diffusion constant, X_M are the reference (undeformed) coordinates, x_i are the material (deformed) coordinates, $F_{jN} = (\partial x_j/\partial X_M)$ is the deformation gradient tensor, $C_{MN} = (\partial x_k/\partial X_M)(\partial x_k/\partial X_N)$ is the right Cauchy-Green deformation tensor, S^{MN} is the second Piola-Kirchhoff stress tensor, and $C = \det(C_{MN})$. The active tension T_a, increases with V, with a delay fixed by $\epsilon(V)$, given by 0.1 for $V > a$ and 1.0 for $V < a$, k_{Ta} is a parameter that controls the amplitude of T_a, the parameters ε, k, μ_1 and μ_2 have no clear physiological meaning, but are fitted to reproduce the key characteristics of cardiac tissue [30]. The mechanoelectric feedback is provided by stretch-activated currents (SACs),

$$I_g = G_s(V-1)(\sqrt{C}-1), \tag{4.5}$$

where G_s is the maximal conductance. The current, as defined in (4.5), is only present during stretch (i.e. when $\sqrt{C} > 1$).

Due to active tension, described by T_a, cardiac tissue will deform until a new equilibrium state is reached. The equilibrium equations (4.4), derived using Newton's laws of motion, and boundary constraints are imposed on the model and solved numerically to determine the mechanical deformation.

Cardiac tissues are anisotropic, inhomogeneous, and exhibit nonlinear stress-strain relation called constitutive law [27]. A hyperelastic material model is a type of constitutive model to describe material, mainly elastic material, for which the stress-strain relationship derives from a strain energy density function. The hyperelastic Mooney-Rivlin material model has been used to model the nonlinear mechanical behavior of the myocardium [30, 31, 132, 135], as this model provides a close fit to the stress-strain curve of cardiac tissue. In this work, this model is chosen to describe the passive mechanical properties of cardiac tissue. An isotropic model, which exhibits identical mechanical properties in all directions, such as Mooney-Rivlin model, is a simplified description of the passive mechanical properties. But, since we restrict ourselves to study a one-dimensional model, this simplification is justified. Mechanical stresses in tissue are modeled as the summation of a passive and an active stress component [30].

$$S^{MN} = \frac{1}{2}\left(\frac{\partial W}{\partial C_{MN}} + \frac{\partial W}{\partial C_{NM}}\right) + T_a C^{-1}_{MN}, \tag{4.6}$$

where $W(I_1, I_2)$ is the strain energy function for the Mooney-Rivlin model [130]. It is given by:

$$W(I_1, I_2) = c_1(I_1 - 3) + c_2(I_2 - 3), \tag{4.7}$$

with $I_1(\boldsymbol{C}) = \mathrm{tr}(\boldsymbol{C})$ and $I_2(\boldsymbol{C}) = \frac{1}{2}(\mathrm{tr}(\boldsymbol{C}) - \mathrm{tr}(\boldsymbol{C}^2))$ are the first two principal invariants of $\boldsymbol{C}$, and $\mathrm{tr}(\boldsymbol{C})$ is the trace of $\boldsymbol{C}$, and c_1 and c_2 are material constants.

4.2.2 Reduction of NP in 1D

In 1D, the deformation gradient tensor $\boldsymbol{F}$, the right Cauchy-Green tensor $\boldsymbol{C}$, and the diffusion tensor $\boldsymbol{D} = \sqrt{C}\boldsymbol{C}^{-1}$ can be written as:

$$\boldsymbol{F} = \begin{bmatrix} F(X) & 0 & 0 \\ 0 & 1 & 0 \\ 0 & 0 & 1 \end{bmatrix}, \qquad \boldsymbol{C} = \begin{bmatrix} F^2(X) & 0 & 0 \\ 0 & 1 & 0 \\ 0 & 0 & 1 \end{bmatrix} \tag{4.8}$$

$$\boldsymbol{D} = \begin{bmatrix} \dfrac{1}{F(X)} & 0 & 0 \\ 0 & F(X) & 0 \\ 0 & 0 & F(X) \end{bmatrix} \tag{4.9}$$

Let $x = X + u$, where x, and X are the material and reference coordinates respectively, and u is the displacement variable, we can write $F(X)$ as:

$$F(X) = \frac{\partial x}{\partial X} = 1 + \frac{\partial u(X)}{\partial X} \tag{4.10}$$

The second Piola-Kirchhoff stress tensor, given in (4.6), is the sum of the passive stress tensor ($\boldsymbol{S_{pass}}$) and the active stress tensor, and is expressed as:

$$\boldsymbol{S} = \boldsymbol{S_{pass}} + T_a \boldsymbol{C}^{-1} \tag{4.11}$$

The second Piola-Kirchhoff passive stress tensor ($\boldsymbol{S_{pass}}$) for the Mooney-Rivlin material is calculated, see [133] for more details, as:

$$\boldsymbol{S_{pass}} = 2\left(c_1 + c_2 \mathrm{tr}(\boldsymbol{C})\right)\boldsymbol{I} - 2c_2\boldsymbol{C}, \tag{4.12}$$

The stress tensor $\boldsymbol{S}$ becomes:

$$\boldsymbol{S} = 2\left(c_1 + c_2 \mathrm{tr}(\boldsymbol{C})\right)\boldsymbol{I} - 2c_2\boldsymbol{C} + T_a\boldsymbol{C}^{-1} \tag{4.13}$$

In 1D the second Piola-Kirchhoff stress S^{11} is expressed as:

$$S^{11} = \tilde{c} + \frac{T_a}{F^2(X)}, \tag{4.14}$$

with $\tilde{c} = 2\left(c_1 + c_2(D-1)\right)$, and D is the dimension of $\boldsymbol{F}(D = 3)$. The Cauchy stress tensor $\boldsymbol{\sigma}$ is given by:

$$\boldsymbol{\sigma} = \frac{1}{J}\boldsymbol{F} \cdot \boldsymbol{S} \cdot \boldsymbol{F}^{\mathrm{T}}, \tag{4.15}$$

where $J = \det(\boldsymbol{F})$, where $\det(\boldsymbol{F})$ is the determinant of $\boldsymbol{F}$. In 1D the Cauchy stress σ^{11} can be calculated using (4.15) as:

$$\sigma^{11} = \sigma^{11}_{pass} + \frac{T_a}{F(X)}, \tag{4.16}$$

where $\sigma^{11}_{pass} = \tilde{c}F(X)$. In the absence of deformation, σ^{11}_{pass} must be zero. Therefore, we need to apply an internal constant pressure p into σ^{11}_{pass} that is given as:

$$\sigma^{11}_{pass} = \tilde{c}F(X) + p \tag{4.17}$$

The pressure p can be determined by requiring $\sigma^{11}_{pass} = 0$ when $F(X) = 1$. This leads to $p = -\tilde{c}$, and σ^{11} becomes:

$$\sigma^{11} = \tilde{c}F(X) - \tilde{c} + \frac{T_a}{F(X)} \tag{4.18}$$

S^{11} can now be written, using $\boldsymbol{S} = J\boldsymbol{F^{-1}}\boldsymbol{\sigma}\boldsymbol{F^{-\mathrm{T}}}$, as:

$$S^{11} = \tilde{c} - \frac{\tilde{c}}{F(X)} + \frac{T_a}{F^2(X)}, \tag{4.19}$$

and the elastic equation (4.4) in 1D is given as:

$$\frac{\partial}{\partial X}\left(\tilde{c}F(X) - \tilde{c} + \frac{T_a}{F(X)}\right) = 0 \tag{4.20}$$

Replacing (4.10) by its value in (4.20), the following is obtained:

$$\tilde{c}\frac{\partial^2 u}{\partial X^2} + \frac{\partial}{\partial X}\left(\frac{T_a}{1 + \dfrac{\partial u(X)}{\partial X}}\right) = 0 \tag{4.21}$$

4.2.3 Reduction of NP in 1D in the limit of small deformations

In the limit of small deformations, $\dfrac{\partial u_k}{\partial X_M} \ll 1$, and the deformation gradient $F(X)$, given in (4.10), is approximated as:

$$F(X) = 1 + u(X) \tag{4.22}$$

Assuming $T_a \ll \tilde{c}$, the elastic equation (4.4) in 1D is reduced into:

$$\tilde{c}\frac{\partial^2 u}{\partial X^2} + \frac{\partial T_a}{\partial X} = 0, \tag{4.23}$$

where $\tilde{c} = 2\left(c_1 + c_2(D-1)\right)$.

Linearized elastic model may be used for strains less than 5% [50, 130, 136].

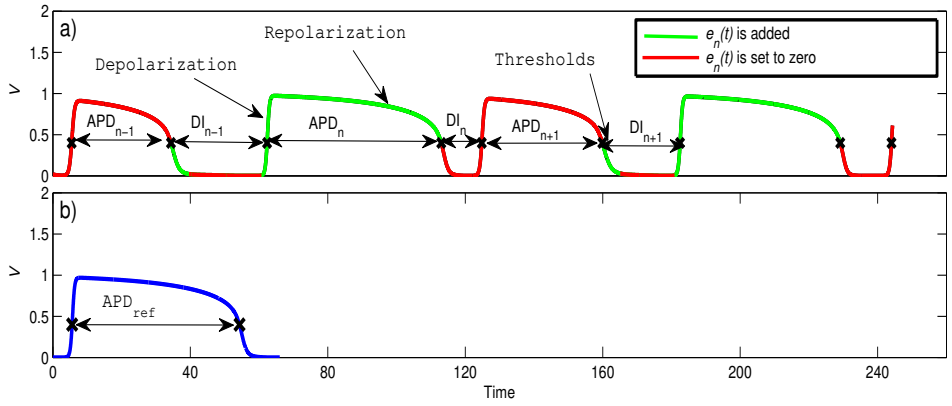

Figure 4.3: Time evolution of transmembrane potential, shown in a), depicting functioning of an error signal when control is on, while b) depicts transmembrane potential reference taken before alternation.

4.3 Control Algorithms

In this section, we describe the control algorithms developed to suppress alternans for the NP model in 1D. Two control algorithms are presented. The first one is provided under small deformation condition and uses spatially distributed mechanical perturbation control, which perturbs the tissue by exerting a force that causes nodal displacement in cardiac tissue. This is reflected in a reaction-diffusion model via the diffusion tensor and MEF, and consequently affects the electrical APD in order to suppress alternans. The second control algorithm provided under large deformation condition is an extension of the one developed for the small deformation condition. It combines spatially distributed mechanical perturbation control with electrical boundary pacing that can be realized by shortening or lengthening the period interval, which has the effect of suppressing cardiac alternans up to 1 cm from the pacing site.

First, we induce alternans by reducing pacing cycle length for the onset of alternans. The tissue is paced at the boundary at a basic pacing cycle length (PCL), named τ^*, such that the APD alternates. Under constant PCL, the amplitude of alternans grows. The APD is measured from the instant when V crosses the threshold value during the depolarization phase, until the instant it falls below this value during the repolarization phase. The threshold value is chosen to be 0.4 (in dimensionless units).

Under small deformation condition, alternans suppression can be achieved by applying spatially distributed mechanical perturbation control which is implemented as follows:

$$\frac{\partial T_a}{\partial t} = \epsilon(V)(k_{T_a}V - T_a) + \beta e_n(\zeta) \tag{4.24}$$

$$e_n(\zeta) = \begin{cases} APD_{\text{ref}}(\zeta = 0, \tau^*) - APD_{n-1}(\zeta), \text{ if } \rho > 0 \\ \\ 0 \qquad \text{otherwise,} \end{cases} \tag{4.25}$$

where β is the controller gain, and $\rho = APD_{\text{ref}}(\zeta = 0, \tau^*) - APD_{n-1}(\zeta)$. The error $e_n(\zeta)$ (defined in (4.25)) is generated from the difference between APD reference ($APD_{\text{ref}}(\zeta = 0, \tau^*)$) at the pacing site, recorded at the time we reach τ^*, and the APDs at the n-th stimulus (APD_n), over the length of the area under spatially distributed control (1-1.5 cm region).

This basic state feedback algorithm takes $e_n(\zeta)$ and provides a control signal which is applied over the region of 1-1.5 cm. The control signal is not null (active) only when $e_n(\zeta) > 0$, meaning that the controller only acts on the short-APD. It is added as a positive quantity to (4.25), when the transmembrane potential crosses the threshold value during the repolarization phase at the n-th stimulus (APD_n), but it is set to zero during the resting time ($V < 0.01$) until the transmembrane potential crosses the threshold value during the repolarization phase at the $n+1$-th stimulus (APD_{n+1}) (see Fig. 4.3).

As seen previously, the governing equations of the electromechanical NP model are composed of three components: equations (4.1) and (4.2) that model the cardiac electrophysiology, equation (4.4) that models cardiac tissue mechanics, and equation (4.3) that models active tension. A simple schematic diagram of the mechanical perturbations control system, as shown in Fig. 4.4, consists of the three above mentioned components, the controller, as defined in equations (4.24) and (4.25), and the sensor. The controller acts on the difference between the desired APD_{ref} and the APDs measured by the sensor. When the difference is not null, it sends a control signal to the active tension model to perturb the active tension variable, which in turn perturbs mechanical properties of the cardiac mechanical model. The perturbation of mechanical properties alters the electrical APD of the cardiac electrophysiological model, via

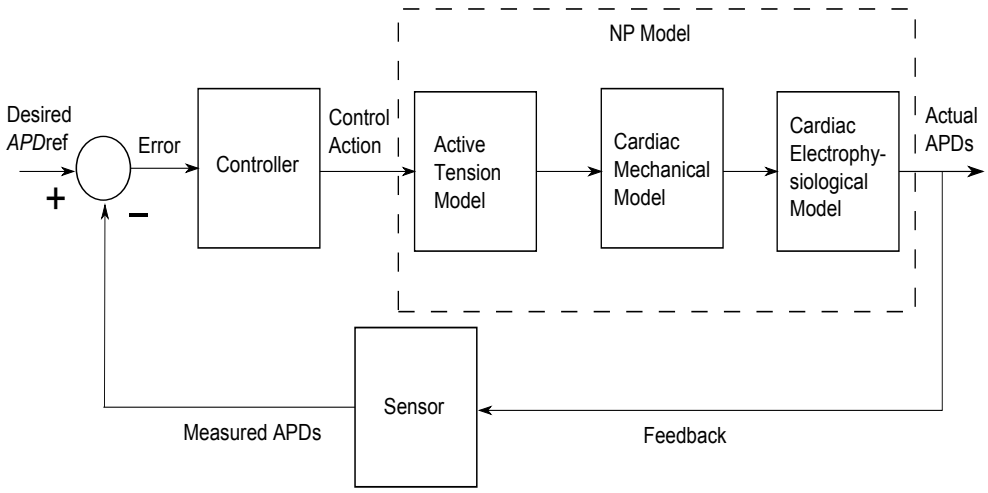

Figure 4.4: A schematic diagram of the mechanical perturbations control system. The difference between the APD reference, and the measured APDs is amplified (gain based controller) and a control action is applied on the active tension model to perturb the active tension variable, which in turn perturbs the mechanical displacement variable of the cardiac mechanical model. This perturbation affects the transmembrane potential, through the diffusion tensor and MEF.

the diffusion tensor and MEF, in order to suppress alternans.

Based on our numerical experiments, using this control strategy for the large deformation case, does not suppress alternans, therefore, we combined it with electrical boundary pacing algorithm.

Boundary pacing control is realized by adjusting the stimulation pacing interval subjected by the cardiac system, and is determined by the dynamic control scheme [19]:

$$T^n = \tau^* + \gamma(APD_n(\zeta = 0) - APD_{n-1}(\zeta = 0)) \tag{4.26}$$

T^n represents the amount of time between the n-th and (n+1)-th stimuli. Here γ is a tunable constant which defines feedback gain of the APD alternation of the basic pacing cycle. For positive γ the second term on the right-hand side of (4.26) has the effect of lengthening T^n if the difference of two consecutive APDs is positive. As a result, the following DI, and hence the next APD at the (n+1)th beat, is larger by using this control scheme.

It has been demonstrated in [19, 21, 24] that this pacing control can suppress alternans for the region from the pacing site up to a finite distance (≤ 1 cm). Beyond that region the instabilities grow along the tissue, and discordant alternans has been

observed. To overcome this limitation in controllability, we added an error based feedback control algorithm that perturbs the tissue cardiac mechanics in a localized region. The spatially distributed mechanical perturbation control, implemented as defined in (4.24) and (4.25), provides a control signal which is applied over the region of 1-2 cm. The controller acts after the electrical boundary feedback controller stabilizes a finite part of the tissue's length (≈ 1 cm). The mathematical model used for the case of small deformation is a simplification (elastic equation is linear) of the one used for the case of large deformation (elastic equation is nonlinear). Therefore, to illustrate the physiological differences in the models' responses to the mechanical perturbation algorithms, a mathematical analysis study, which goes far beyond the scope of the present paper which focuses on numerical exploration, is required.

4.4 Numerical Results and Discussion

In all our simulations, a one dimensional cardiac cable of the length $L = 7$ cm, fixed at the end points (isometric contraction regime) is considered. The excitation characteristics of the medium was solved by a semi-implicit time integration scheme with $\Delta t = 0.02$ (dimensionless) and $\Delta X = 0.1$ (dimensionless), and we determined the deformation mechanics of the tissue using the second order finite difference scheme. As outlined in [30], to determine the scaling factor for the dimensionless time unit, the dimensionless APD obtained from the model must be compared to experimental measurements. Scaling factors ranging from 5 ms to 14 ms have been reported [46, 137, 138]. For the dimensionless space variable, 1 dimensionless unit corresponds to 1 mm [137, 138].

For the given parameters of the cardiac model, APD alternans is induced by pacing the tissue at the boundary at a constant period, starting with a large one, of 81 time unit, until a steady-state APD is reached. This is repeated, but each time the period is reduced by one time unit, until an alternation in the APDs is observed, and the resulting period, named tau^*, is the basic pacing cycle length (PCL).

In order to induce alternans, no initiation of a new action potential, due to effects of SACs [126, 31], should be allowed. Therefore, for a defined maximal local deformation, G_s can be given any value that is less than a certain threshold, which

is determined by numerical experiments, above which a new action potential is initiated.

4.4.1 Control of cardiac alternans using spatially distributed mechanical perturbation

Under condition of small deformation, (4.1) - (4.3), and (4.23) of the NP model are solved. The constant materials c_1 and c_2, together with the parameter k_{T_a} determine local deformations during contraction, so they are chosen to give rise to maximal local deformations $< 5\%$ following excitation. All model parameters used in the simulation are given in Table 4.1. For the given parameters, τ^* is found to be 60 time units. The controller gain β is chosen to be -0.0006 in the simulation.

The amplitude of alternans, $a_n(\zeta)$, is defined as the difference between two consecutive APDs at a given point in space ζ:

$$a_n(\zeta) = (APD_n(\zeta) - APD_{n-1}(\zeta))(-1)^n \tag{4.27}$$

As shown in Fig. 4.5(b), the control action, applied at $t = 6000$, successfully suppress alternans. This control action alters the tissue's transmembrane potential through the diffusion transport tensor and MEF, in which changes in T_a affect the mechanical displacement variable u in the elastic equation (4.4), which then affects the transmembrane potential (4.1), through the tensor $\boldsymbol{D}$ and I_g. As shown in Fig. 4.6, the APD width alternates when the control is not applied, Fig. 4.6(a), and is suppressed, Fig. 4.6(b), after the control is applied.

The presence of electrical alternans induces, through the mechanism of ECC, an alternation in the heart muscle contractile activity, see Fig. 4.7. As can be seen, the displacement variable u for a single cell alternates when APD alternates (Fig. 4.7(b)). As shown in Fig. 4.8, the displacement variable alternates when the control is not applied, Fig. 4.8(b), and is suppressed (Fig. 4.8(c)) after the mechanical perturbation control is applied. It has to be noted that the largest displacements after applying control (Fig. 4.8(c)), with respect to the displacements before applying control (Fig. 4.8 (a) and (b)), occur in the localized region (1-1.5 cm), where the control signal is applied. As shown in Fig. 4.9, the largest changes in I_g after applying control (Fig.

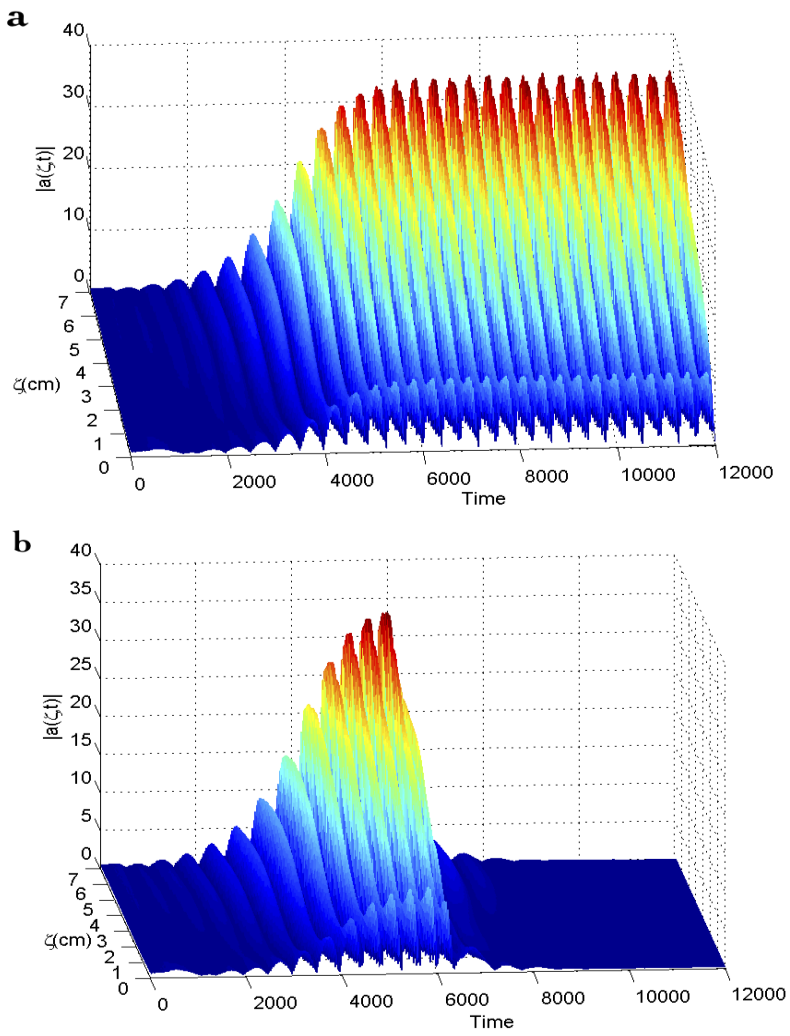

Figure 4.5: Amplitude of alternans of the NP model. The amplitude of alternans grows, shown in (a), when no control is applied, while (b) illustrates the alternans suppression by the mechanical perturbation algorithm when the control action is applied at $t = 6000$.

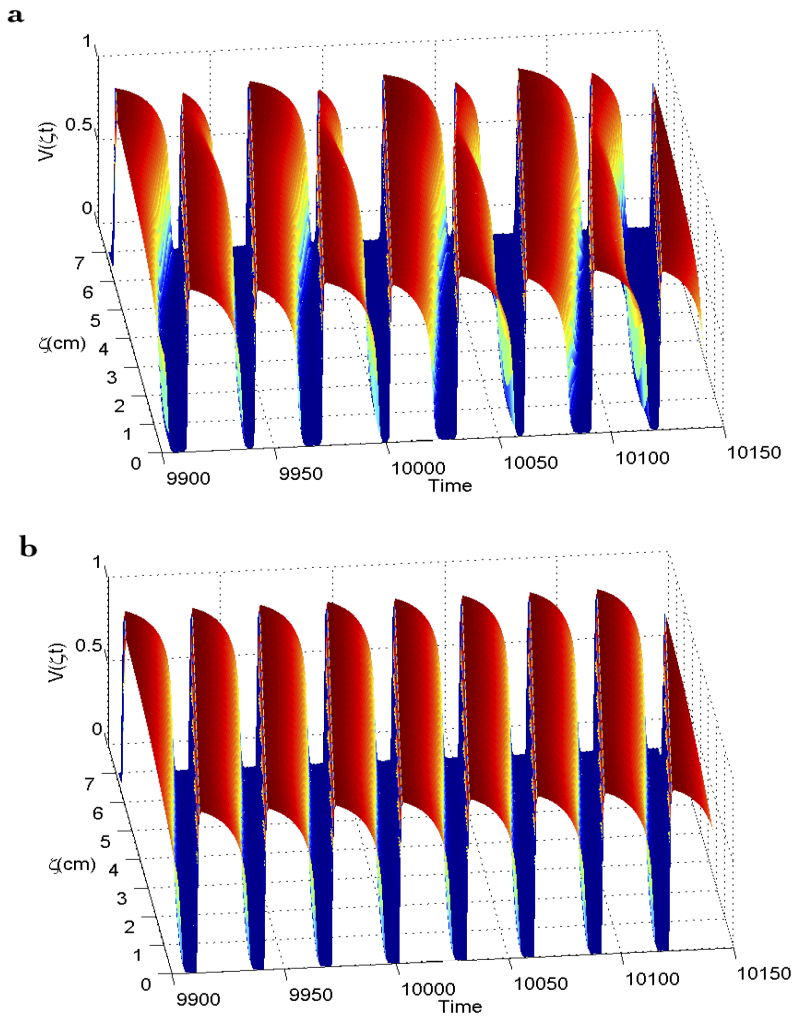

Figure 4.6: Time evolution of transmembrane potential variable before (a), and after (b) the control is applied.

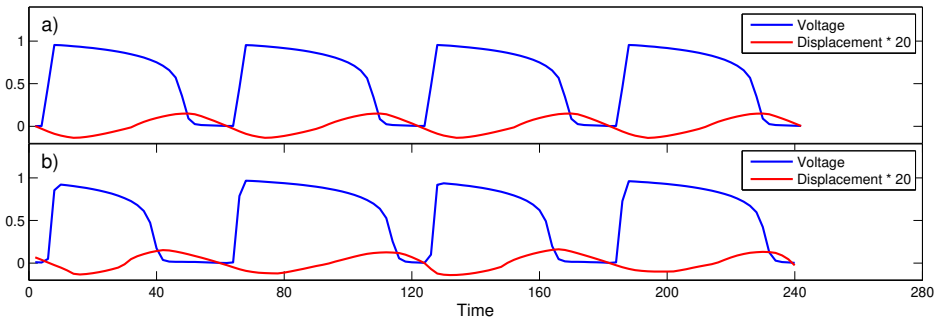

Figure 4.7: Time evolution of transmembrane potential and displacement variables for the center of the medium, shown in (a), when no alternans is present, while (b) illustrates time evolution in the presence of alternans.

4.9(c)), with respect to I_g before applying control (Fig. 4.9(a) and (b)), occur in the localized region (1-1.5 cm) where the control signal is applied.

Although spatially distributed control is only applied over a localized region of the tissue (0.5 cm), it successfully suppress alternans along the tissue. Thus, using a model based on the mechanical properties of cardiac tissue, it is clearly shown that spatially distributed mechanical perturbation control can be used to manipulate the electrical APD in order to suppress alternans.

Moreover, although mechanical perturbation control is applied locally, it perturbs the mechanical displacement u globally in the elastic equation (4.4), since the perturbation occurs along the entire points of the cable but the end points which are fixed, and the largest displacements after applying control, with respect to the displacements before applying control, occur in the localized region (1-1.5 cm) where the control signal is applied. This perturbation affects the transmembrane potential globally in equation (4.1), through the diffusion tensor ($\boldsymbol{D}$) and MEF (I_g), since it is applied along the entire cable length of cardiac cells.

4.4.2 Control of cardiac alternans using electrical boundary pacing and spatially distributed mechanical perturbation

Under condition of large deformations, (4.1) - (4.3), and (4.21) of the NP model are solved. The constant materials c_1 and c_2, together with the parameter k_{T_a} determine

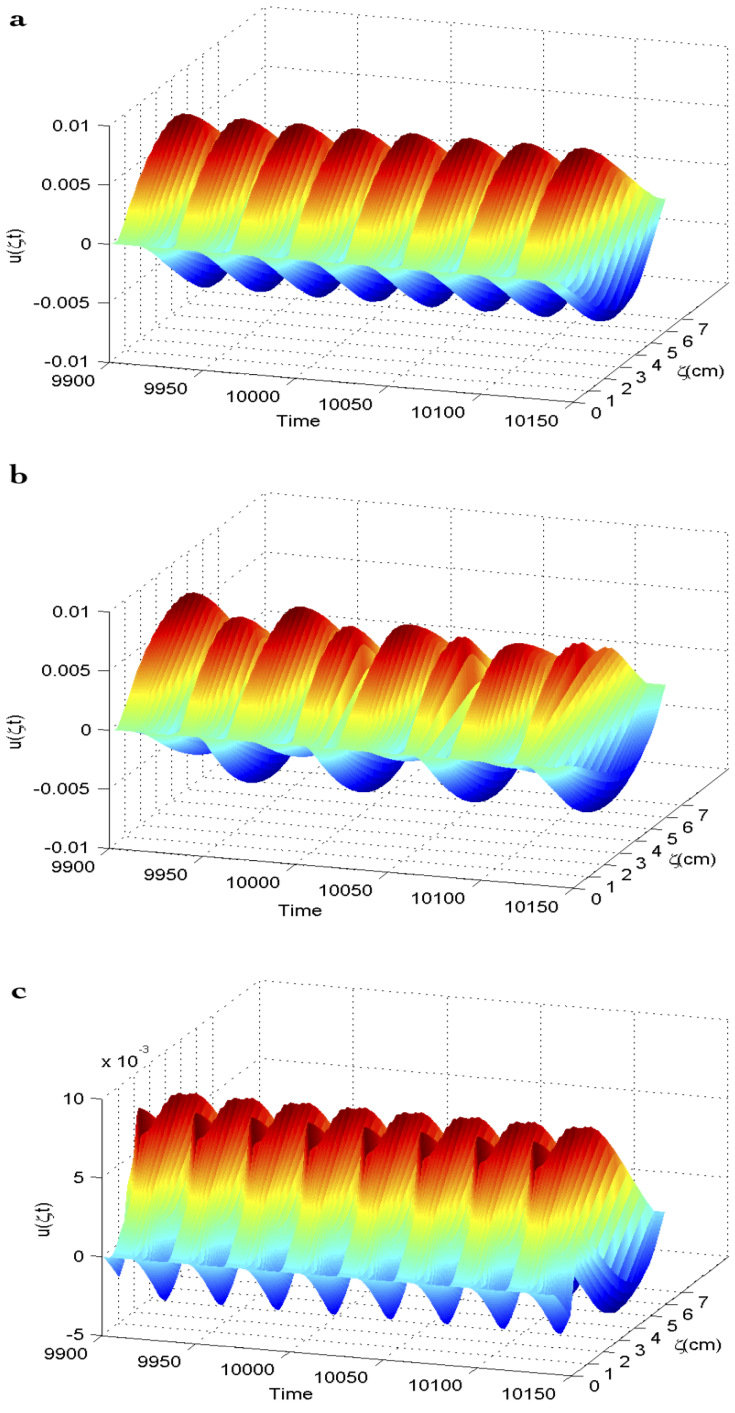

Figure 4.8: Time evolution of displacement variable, shown in (a), when no alternans is present, while (b) illustrates time evolution in the presence of alternans, while (c) illustrates time evolution when the control signal is applied.

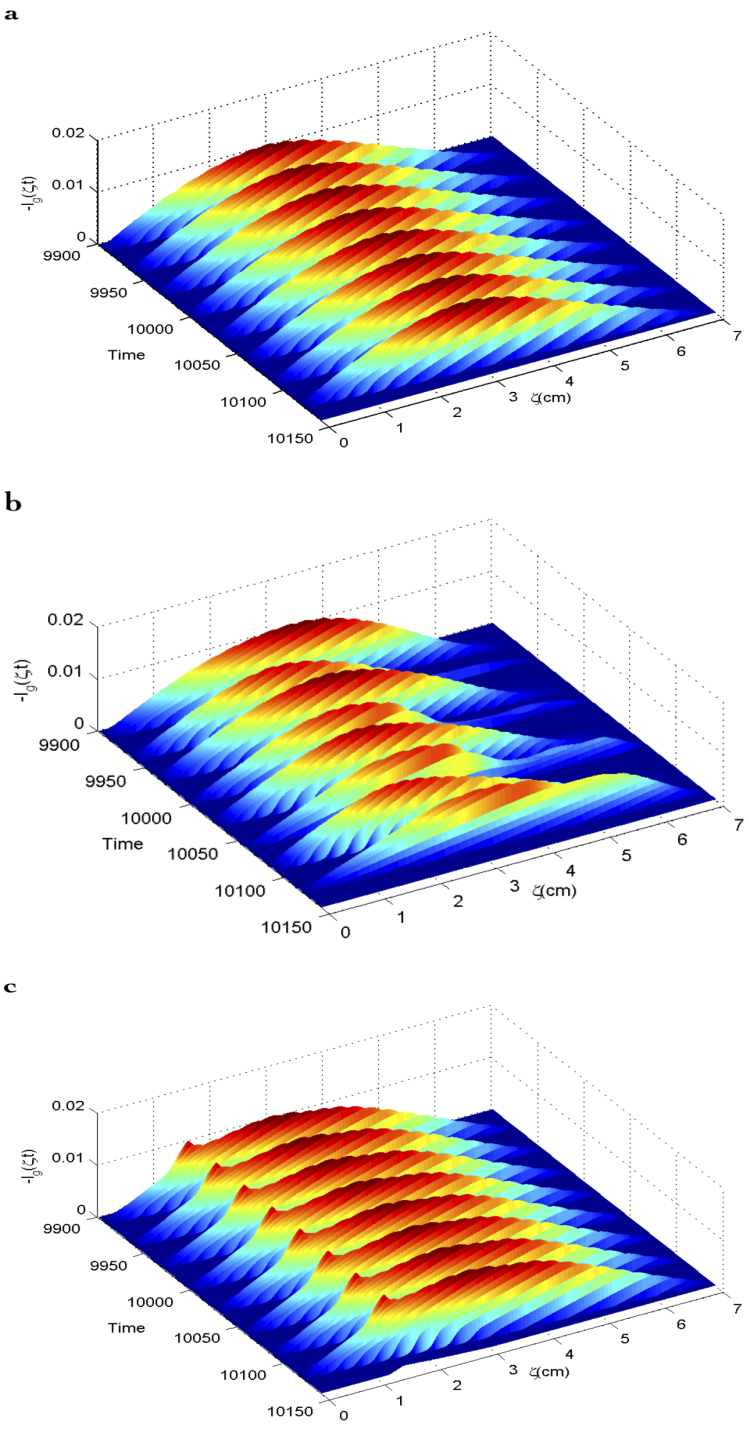

Figure 4.9: Time evolution of the stretch-activated currents $I_g(\zeta, t)$, shown in (a), when no alternans is present, while (b) illustrates time evolution in the presence of alternans, while (c) illustrates time evolution when the control signal is applied. Note that $I_g(\zeta, t)$ is multiplied by -1 for clarity. The largest changes in I_g after applying control (c), with respect to I_g before applying control (a) and (b), occur in the localized region (1-1.5 cm) where the control signal is applied.

local deformations during contraction, so they are chosen to give rise to maximal local deformations between 5% and 20% following the excitation. All model parameters used in the simulation are given in Table 4.2. For the given parameters, τ^* is found to be 53 time units. In the simulation, $\gamma = -0.275$ and $\beta = 0.005$.

It has been demonstrated in [24] that in order to suppress alternans in the cables of the length > 1 cm, a model-based control algorithm, that is realized with a number of measurements used in the feedback realization at least equal to the number of unstable modes, must be used. The electrical pacing algorithm defined in (4.26) uses boundary point measurement of the amplitude of alternans, and therefore it can just stabilize a single mode. This is due to the fact that the tissue characteristic length of ≈ 1 cm has one unstable mode. This algorithm cannot achieve stability for the cables exceeding 1 cm in length due to the presence of unstable modes that start to appear when the length of the tissue size is considerably increased. Inability of electrical pacing algorithms to control alternans in longer cables (> 1 cm) is due to the lack of knowledge of the spatial evolution of alternans.

On the other hand, it is not feasible to have a spatially distributed electrical

Table 4.2: Parameter values for the electromechanical model employed for large deformation

$k = 8$	$a = 0.05$	$\varepsilon = 0.1$	$\mu_1 = 0.12$
$\mu_2 = 0.3$	$k_{Ta} = 1$kPa	$\tilde{c} = 1.78$kPa	$G_s = 0.05$

perturbation for alternans control, since the existence of several pacing centers would change the location of the onset of the propagating excitation wave, which in general cannot take place away from the apex of the heart. Also, simultaneous pacing at two sites cannot be used, since the induced beats, coming from both sides of the cable, collide and annihilate when the two wavefronts meet. In addition, implementing spatially distributed electrical perturbations, by using many electrodes, placed one after another, in a small localized region will not suppress alternans either, because the perturbation input to voltage of a nonlinear cardiac excitable cell model cannot be realized due to strong coupling of ionic currents models. Therefore, using solely perturbation of the pacing control would not work due to the intrinsic nonlinear dynamics of the propagating excitation wave, and its manifestation of alternans

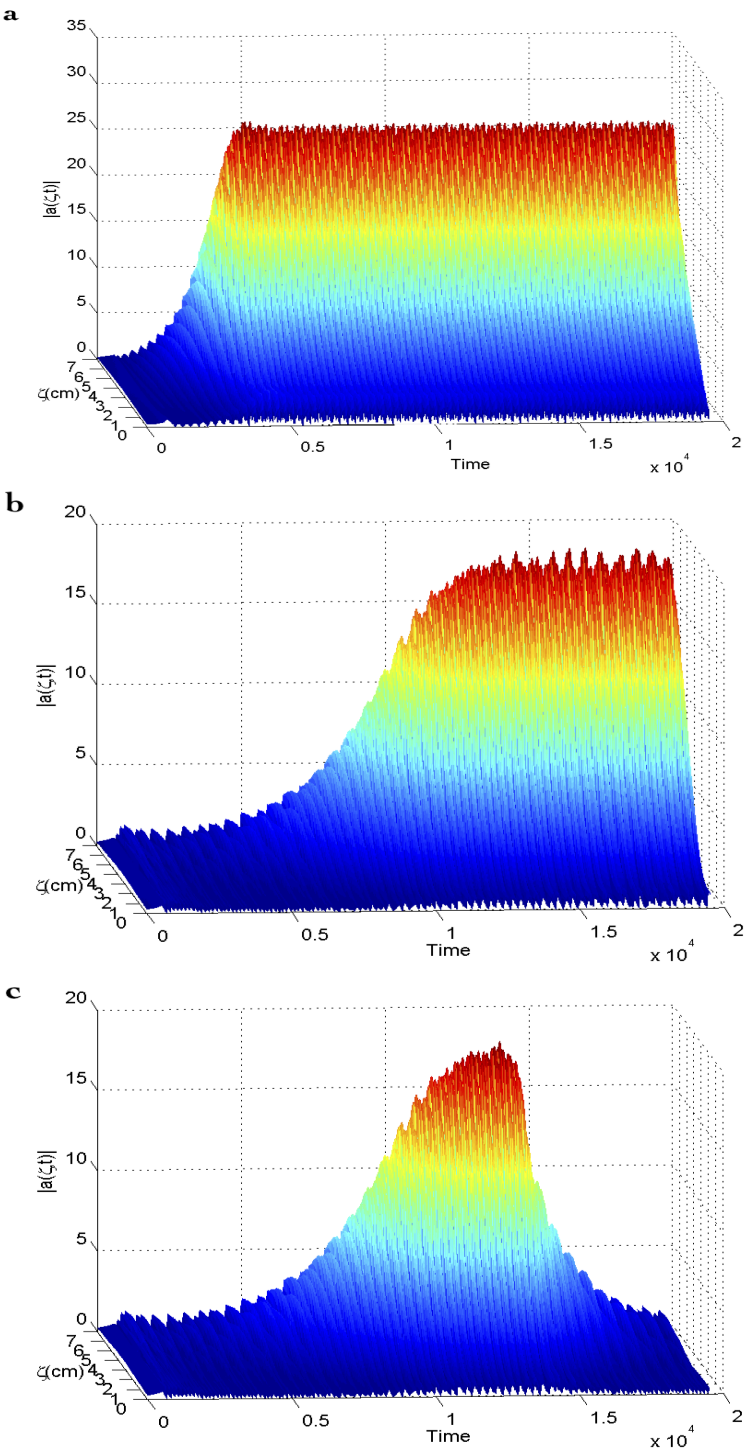

Figure 4.10: Amplitude of alternans of NP model. The amplitude of alternans grows, shown in (a), when no control is applied, while (b) illustrates the alternans suppression by electrical boundary pacing applied when τ^* is reached, while (c) illustrates the alternans suppression by electrical boundary pacing and spatially distributed mechanical perturbation when the control action is applied at $t = 14000$.

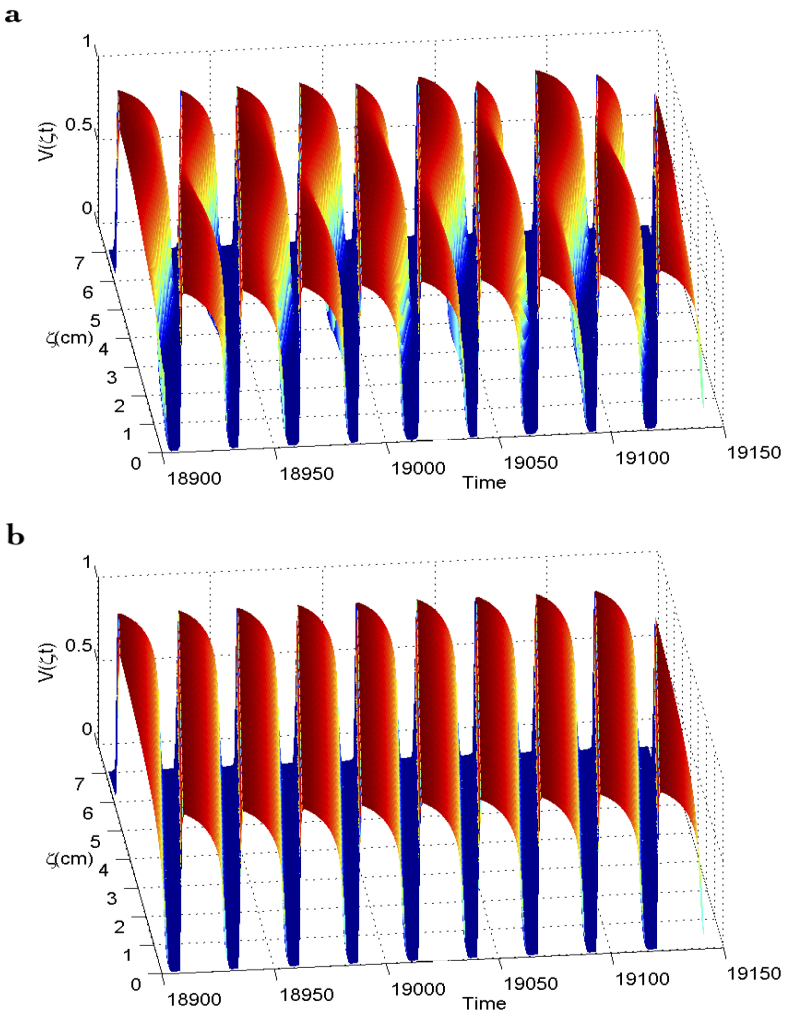

Figure 4.11: Time evolution of transmembrane potential variable before (a), and after (b) the control is applied.

instabilities, which is associated with unidirectional propagation of the electric wave from the pacing center to the external tissue. Hence, an independent type of interaction through the inclusion of mechanical perturbation is added, since this method of interaction is independent of the pacing protocol, and a model-based control algorithm that combines the pacing interval with the spatially distributed mechanical perturbation is used. This model-based control has a full knowledge of the entire state of alternans, since it is realized with sufficient measurements in the feedback.

As shown in Fig. 4.10, the amplitude of alternans grows (Fig. 4.10(a)) when no control is applied, and when the control action is applied at $t = 14000$, it successfully suppress alternans (Fig. 4.10(c)). This control action alters the tissue's transmembrane potential when mechanical perturbation is applied, in which changes in T_a affect the mechanical displacement variable u in the elastic equation (4.4), which then affects the transmembrane potential (4.1), through the tensor $\boldsymbol{D}$ and I_g. Perturbing the diffusion tensor and MEF alter the tissue's electric wave profile, and consequently the APD. As shown in Fig. 4.11, the APD width alternates when the control is not applied, Fig. 4.11(a), and is suppressed, Fig. 4.11(b), after the control is applied.

Although the spatially distributed control is only applied over a localized region of the tissue (1 cm), it successfully suppresses alternans along the tissue. Thus, the control of alternans in large and relevantly sized cardiac tissues can be achieved by the manipulation of the electrical APD using a model based on the mechanical and electrophysiological properties of cardiac tissue.

4.5 Conclusion

Most studies attempted to suppress alternans in cardiac tissue by adjusting the boundary pacing interval by using models that account only for electrophysiological properties of cardiac tissue. This feedback control strategy has failed to suppress alternans completely in tissues exceeding 1 cm [19, 21, 24, 25]. In this study, we utilize an electromechanical model (NP model) for cardiac tissue which couples cardiac excitation and contraction. We consider two aspects of elasticity, linear and nonlinear, for cardiac mechanics depending on the maximal local deformations that can occur in cardiac tissue. Our control algorithms consider electrical pacing and error based

feedback control that is implemented using mechanical perturbation control strategy and employ direct mechanical perturbation in a localized region on the tissue in order to suppress alternans. Perturbing cardiac tissue mechanics in a localized region of the tissue alters the tissue's electric wave profile, and consequently the electrical APD, in order to suppress alternans. We have demonstrated that by the inclusion of spatially distributed mechanical perturbation control, we have overcome the limitation in controllability of the electrical pacing control, and achieved the alternans suppression in relevantly sized cardiac tissues. Numerical simulations were presented demonstrating that a model based on the mechanical and electrophysiological properties of cardiac tissue can be used to successfully suppress alternans, under small and large deformation conditions, along the whole cable of the cardiac tissue cells.

Chapter 5

Mechanical perturbation control of cardiac alternans

5.1 Introduction

Electrical alternans is a beat-to-beat long-short alternation in the cardiac action potential duration (APD) (Fig. 5.1 (a)) [3], and is believed to be linked to the onset of lethal heart rhythm disorders such as ventricular fibrillation (VF) [1, 2]. The diastolic interval (DI) (Fig. 5.1) is the time lapse between the end of the previous action potential and the next one (Fig. 5.1). It has been shown both clinically and experimentally that alternans degenerates quickly into ventricular tachycardia or fibrillation. Clinical manifestations of alternans is reflected in a beat to beat alternation of T-wave amplitude, known as T-wave alternans (TWA), on the electrocardiogram (ECG). The TWA is a marker of vulnerability to VF, and of sudden cardiac death (SCD) [4]. Experimentally, it has been observed that alternans can lead to complex spatiotemporal patterns along the epicardium and endocardium [139], and often precedes the development of more dangerous arrhythmias. Therefore, the suppression of cardiac alternans is potentially an effective strategy in preventing VF and SCD.

In the literature, electrical perturbation control has been the most studied approach to terminate alternans, see [51] for details. With this approach, the pacing cycle length (PCL) is perturbed by an amount proportional to the difference between the last two APDs. This control algorithm has been proven to be effective in controlling alternans in small tissues of up to 1 cm. A one-dimensional (1D) map that relates the DI at one beat to the APD of the subsequent beat via the restitution curve

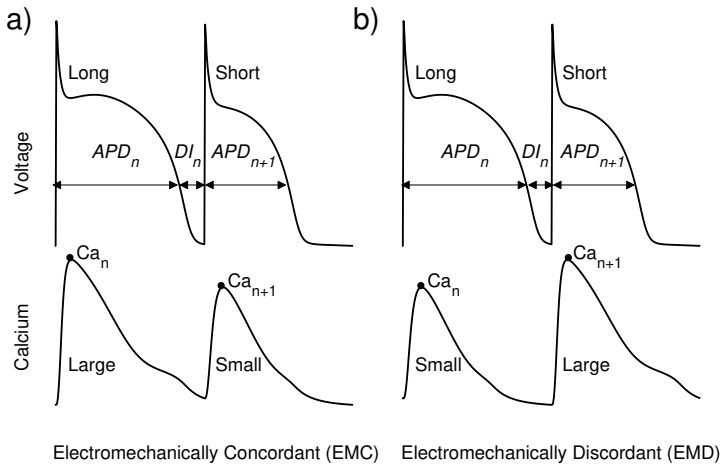

Figure 5.1: Schematic representation of voltage and calcium alternans.

(see Section 4), is used to describe the alternans [69, 70]. Another important factor influencing alternans is the bidirectional coupling between the membrane voltage (V) and intracellular calcium (Ca^{2+}) dynamics, where the APD alternans induces alternation in the amplitude of calcium transients through the $V \rightarrow Ca^{2+}$ coupling (Ca^{2+} alternans) (Fig. 5.1). Iterative maps [16, 140, 141, 75, 77] have been used to perform stability analysis of alternans. In [16], a two-dimensional (2D) discrete map at the single cell level is presented. At the tissue level, the amplitude of equations derived from the maps by taking into account the effect of electrotonic coupling, is used to analyze the stability of the system of coupled maps [140]. Moreover, a theoretical framework of iterative maps describing the coupled dynamics of V and Ca^{2+} has been previously used at the subcellular and cellular levels [141, 75, 77, 76].

Nearly, all the work that has been done on the stability and control of alternans is electric-based. However, recently a novel mechanical perturbation algorithm to suppress alternans was presented in [97, 51]. This perturbation is reflected in cardiac excitation through the mechanisms of mechano-electric feedback (MEF). The main advantage of this approach is that the alternans is suppressed in cardiac tissues of relevant size. In [51], we used a simple phenomenological model of cardiac excitation, while active tension was generated with an oversimplified isotropic active tension

transient.

In this work, we analyze the effects of mechanical perturbation on the dynamics of the map-based model. This model is based on coupling between the membrane voltage and active tension systems at the cellular level, and uses a theoretical framework of 2D iterative maps of the heart beat-to-beat dynamics. To make this possible, a simplified description of MEF is provided, and a coupled map model describing the bidirectional coupling between the membrane voltage and active tension at the cellular level is presented. Also, a discrete form of the proposed control algorithm that can be used in the coupled map model is derived. The stability of the model can be analyzed from the eigenvalues of a Jacobian matrix of the system of coupled maps.

In a second goal of this study, a biophysically detailed model of cardiac electromechanics is employed to investigate the control of alternans. We explore the feasibility of suppressing cardiac alternans in a realistic electromechanical model using the mechanical perturbation strategy. Luo-Rudy [49] and Fox [48] models are used to represent electrical activity in heart tissue, while mechanical properties are described by the Mooney-Rivlin material response [51, 30]. Active tension that couples the electrophysiological model and the cardiac mechanics model is generated using a smooth variant of the Nash-Panfilov [55] model and the Niederer-Hunter-Smith [56] model. Numerical simulations are presented to demonstrate successful suppression of alternans in two realistic electromechanical models of cardiac tissue using the proposed control algorithm.

The paper is organized as follows. In Section II, we describe the cardiac electromechanical model used in this work. The mechanical perturbation control algorithm is presented in Section III. Section IV is devoted to theoretical analysis, and a stability analysis of the derived system of coupled maps at the cellular level is provided. Section V presents numerical simulations demonstrating successful suppression of alternans by the proposed control algorithm, followed by a discussion. The findings are summarized in Section VI and future prospects are proposed.

5.2 Cardiac electromechanical model

In this section, we describe mathematical equations that model the electrical excitation and mechanical contraction.

5.2.1 Cardiac Mechanics

Mechanical analysis is based on the finite deformation elasticity theory, therefore a mathematical model of cardiac deformation is governed by equations of nonlinear elasticity. These equations are derived using Newton's laws of motion [51, 30] and are expressed as:

$$\frac{\partial}{\partial X_M}(S^{MN}F_{jN}) = 0, \tag{5.1}$$

where $F_{jN} = (\partial x_j/\partial X_M)$ is the deformation gradient tensor, X_M are the reference (undeformed) coordinates, x_i are the material (deformed) coordinates, the uppercase subscripts (M and N) and lowercase subscripts (i and j) correspond to the reference and current configurations, respectively, and S^{MN} is the second Piola-Kirchhoff stress tensor.

Two approaches, namely active strain and active stress, have been proposed to model the active mechanical response of the myocardium. For the active strain model, a multiplicative decomposition [52] of the deformation gradient tensor into a passive and an active part is assumed. The second model, which is the most widely used and it is adopted in this work, is based on the concept of active stress [30]. In this approach, S^{MN} is split into a passive and an active stress component [30], and is given by:

$$S^{MN} = \frac{1}{2}\left(\frac{\partial W}{\partial C_{MN}} + \frac{\partial W}{\partial C_{NM}}\right) + T_a C^{-1}_{MN}, \tag{5.2}$$

where $W(I_1, I_2)$ is the strain energy function, $C_{MN} = (\partial x_k/\partial X_M)(\partial x_k/\partial X_N)$ is the right Cauchy-Green deformation tensor, and T_a is active tension generated by the electrical model. The isotropic Mooney-Rivlin constitutive model, which is used to describe passive mechanical properties of the cardiac tissue [51, 30], is adopted in the present study, where the strain energy W is given by:

$$W(I_1, I_2) = c_1(I_1 - 3) + c_2(I_2 - 3), \tag{5.3}$$

with $I_1(\boldsymbol{C}) = \text{tr}(\boldsymbol{C})$ and $I_2(\boldsymbol{C}) = \frac{1}{2}(\text{tr}(\boldsymbol{C}) - \text{tr}(\boldsymbol{C}^2))$ are the first two principal invariants of $\boldsymbol{C}$, and $\text{tr}(\boldsymbol{C})$ is the trace of $\boldsymbol{C}$, and c_1 and c_2 are material constants. The elastic equation (5.1) in one dimension can be written (see [51]) as:

$$\tilde{c}\,\frac{\partial^2 u}{\partial X^2} + \frac{\partial}{\partial X}\left(\frac{T_a}{1+\dfrac{\partial u(X)}{\partial X}}\right) = 0, \tag{5.4}$$

where $u = x - X$ is the displacement variable, x and X are material and reference coordinates respectively, and $\tilde{c} = 2(c_1 + 2c_2)$ is the material stiffness.

It has been shown in [7] that direct physiological influence of contraction on excitation of cardiac muscle cells, which is termed as mechanoelectric feedback, is given by depolarizing stretch-activated current (I_{SAC}) through stretch-activated channels. I_{SAC} can change the shape of the action potential in response to stretch. A linear voltage-current relationship has been found in experimental studies and linear ionic models have been proposed [60] for I_{SAC}. In this work I_{SAC} as described in [67] is adopted, and is given as:

$$I_{SAC} = G_s \frac{(\lambda - 1)}{(\lambda_{max} - 1)}(V - E_s), \tag{5.5}$$

where G_s and E_s are maximal conductance and reversal potential, respectively, and λ is the extension ratio along the fiber direction, which is normalized by maximal stretch (λ_{max}). Following [67], the parameter G_s can take any value between 0 and 100 μS/μF, and E_s in most biophysical models takes the value of $-20\ mV$. As shown in [67], cardiac cells are assumed to be stretched maximally between 5-10% of the resting position. The I_{SAC} (Eq. (5.5)) is active during stretch, i.e. it is only present when $\lambda > 1$, otherwise, $I_{SAC} = 0$, and is added to total ionic membrane current generated by the ionic model discussed under the cardiac excitation. In a 1D cable of heart tissue, we assume that cardiac fibers are parallel to the X-direction of the undeformed body.

5.2.2 Cardiac excitation

A monodomain model is used to represent cardiac excitation, described by the following parabolic partial differential equation [37]:

$$C_m \frac{\partial V}{\partial t} = \frac{\partial}{\partial X_M}\left(D_{MN}\frac{\partial V}{\partial X_N}\right) - (I_{ion}(\mathbf{u}, V) + I_{stim}),$$

$$\frac{d\mathbf{u}}{dt} = \mathbf{f}(\mathbf{u}, V), \tag{5.6}$$

where V is the membrane voltage, D_{MN} is the diffusion tensor that accounts for electrical anisotropy of cardiac tissue, C_m is the membrane capacitance, I_{ion} is the ionic membrane current describing the excitable behavior of cardiac cells, $\mathbf{f}$ a general function representing the choice of a cell model, $\mathbf{u}$ is the vector of dependent states variables containing ionic concentrations and membrane gating variables, and I_{stim} is the externally electrical stimulus applied at the pacing site. Two cardiac ionic models, namely, Fox model given in [48] and Luo-Rudy-1 (LR1) model [49], are employed in the present study to represent electrophysiological properties of the heart. LR1 is a mammalian ventricular cell based model which incorporates interaction between depolarization and repolarization and accounts for the calcium dynamics in cardiac myocyte. In total, the Luo-Rudy model consists of six individual currents, and of a system of 8 ODEs including the intracellular calcium ion concentration. In 2002, Fox *et al.* [48] presented the canine ventricular myocyte, and it was the first model to ensure occurrence of alternans at fast pacing rates. This model uses 13 currents and consists of a system of 13 ODEs. Moreover, compared to LR1 model, the Fox model incorporates a simplified description of intracellular calcium, therefore, it explicitly accounts for bidirectional coupling between the transmembrane potential and the intracellular Ca^{2+} concentration, while the LR1 model does not.

To take into account mechanical deformation of the tissue, neglected in this model, we modify Eq. (5.6) as described in [30, 67] to obtain:

$$\begin{aligned} C_m \frac{\partial V}{\partial t} &= \frac{1}{\sqrt{C}} \frac{\partial}{\partial X_M} \left(\sqrt{C} D_{MN} C^{-1}_{MN} \frac{\partial V}{\partial X_N} \right) \\ &\quad - (I_{ion}(\mathbf{u}, V) + I_{SAC}(\lambda, V) + I_{stim}), \\ \frac{d\mathbf{u}}{dt} &= \mathbf{f}(\mathbf{u}, V), \end{aligned} \tag{5.7}$$

where $C = \det(C_{MN})$. A novel approach based on the concept of stress-assisted diffusion [142] to describe diffusion processes in a deforming excitable medium, such as cardiac tissue, is proposed. The diffusion tensors employed in [142] are directly influenced by the mechanical stress. Important effects of stress-assisted diffusion in the drifting and conduction velocity of excitation waves are revealed in their study.

5.2.3 Generation of active tension

In this study, two models of active tension generated in response to electrical activation and coupled to nonlinear stress equilibrium equations, are considered.

The first model for the active tension generation is a smooth variant of the Nash-Panfilov (SVNP) model [30, 55, 143] which consists of one ODE and takes voltage as an input, and is given as follows:

$$\begin{aligned} \frac{\partial T_a}{\partial t} &= \epsilon(V)(k_{T_a}(V - V_r) - T_a), \\ \epsilon(V) &= \epsilon_0 + (\epsilon_\infty - \epsilon_0)\exp[-\exp(-\xi(V - V_s))], \end{aligned} \tag{5.8}$$

where the parameter k_{T_a} controls the maximum value of T_a for a given potential V and a given resting potential V_r. $\epsilon(V)$ is the smoothly varying form for the switch function proposed in [30], given in terms of the parameters ϵ_0 and ϵ_∞ that represent the two limiting values of the function for $V < V_s$ and $V > V_s$ about the phase shift V_s, respectively, and the parameter ξ that determines the transition rate of ϵ from ϵ_0 to ϵ_∞ about V_s.

The second one is the Niederer-Hunter-Smith (NHS) model [56], which is an advanced model that depends on quantities derived from both the cardiac mechanics and excitation models. The NHS model consists of a system of 5 ODEs and the general form of the system can be written as:

$$\begin{aligned} \frac{d\mathbf{w}}{dt} &= \mathbf{g}(\mathbf{w}, \lambda, \frac{d\lambda}{dt}, [\mathrm{Ca}^{2+}]_\mathrm{i}, T_a), \\ T_a &= h(\mathbf{w}), \end{aligned} \tag{5.9}$$

where $\mathbf{w} = [w_1, w_2, w_3, w_4, w_5]$ is the vector of internal state variables for the contraction model, $\mathbf{g} = [g_1, g_2, g_3, g_4, g_5]$ and h are prescribed nonlinear functions. $[\mathrm{Ca}^{2+}]_\mathrm{i}$ is the intracellular concentration of Ca^{2+} ions generated by the ionic model, and λ is the extension ratio calculated from the mechanics model. The detailed form of equations for this model is given in [56]. In this model, cardiac contraction results from active tension generated by the myofilaments dynamics initiated by an increase in intracellular calcium concentration $[\mathrm{Ca}^{2+}]_\mathrm{i}$, where the concentration of calcium binds to troponin C (TnC), and follows tropomyosin kinetics with actin sites for myosin crossbridges. In this model, the Ca^{2+} binding to TnC is defined by:

$$\frac{d[\mathrm{Ca}^{2+}]_\mathrm{Trpn}}{dt} = k_\mathrm{on}[\mathrm{Ca}^{2+}]_\mathrm{i}([\mathrm{Ca}^{2+}]_\mathrm{TrpnMax} - [\mathrm{Ca}^{2+}]_\mathrm{Trpn})$$

$$- k_{\text{refoff}}(1 - \frac{T_a}{\Gamma\, T_{\text{ref}}})[\text{Ca}^{2+}]_{\text{Trpn}}, \tag{5.10}$$

where k_{on} and k_{refoff} are the binding and unbinding rates of Ca^{2+} binding to TnC, $[Ca^{2+}]_{\text{Trpn}}$ is the concentration of Ca^{2+} bound to TnC, $[Ca^{2+}]_{\text{i}}$ is the cytosolic Ca^{2+} concentration, $[Ca^{2+}]_{\text{TrpnMax}}$ is the maximal concentration of Ca^{2+} that can bind to site (II), T_a is active tension generated by the cell and T_{ref} is maximal isometric tension under zero strain whilst Γ is tension dependent buffering parameter. The values of these parameters are given in [56]. The equation (5.10) can be written as:

$$\frac{dw_1}{dt} = g_1(w_1, \lambda, \frac{d\lambda}{dt}, [\text{Ca}^{2+}]_{\text{i}}, T_a), \tag{5.11}$$

where $w_1 = [Ca^{2+}]_{\text{Trpn}}$, and $g_1(w_1, \lambda, \frac{d\lambda}{dt}, [\text{Ca}^{2+}]_{\text{i}}, T_a)$ is equal the right-hand side of Eq. (5.10).

5.3 Control algorithm

Our control strategy is based on combining spatially distributed mechanical perturbation algorithm [51] with electrical boundary pacing algorithm [140] in order to control alternans. First, the tissue is paced at the boundary at PCL, named τ^*, such that the APD alternates. Under constant PCL, the amplitude of alternans (Eq. (5.26)) grows.

Boundary pacing control is realized by modulating the pacing interval based on the consecutive APDs at the pacing site, and is determined by the dynamic control scheme [140]:

$$T^n = \tau^* + \gamma\ (APD_n(\zeta = 0) - APD_{n-1}(\zeta = 0)) \tag{5.12}$$

T^n represents the amount of time between the $(n-1)$-th and n-th stimuli, and ζ represents space. Here γ is the feedback gain. As described in [51], this feedback control has the effect of lengthening or shortening T^n at the n-th stimulus based on the difference of two consecutive APDs. This approach is capable of suppressing cardiac alternans at the pacing site and up to a finite distance ($\leq$1 cm) [140, 21, 24]. Beyond that region, the instabilities grow along the tissue. To overcome this limitation in controllability, we combined it with a spatially distributed mechanical perturbation algorithm [51].

Depending on the active tension mathematical model employed, two different mathematical implementations are used to implement the mechanical perturbation control strategy.

For the SVNP model, the spatially distributed mechanical perturbation control algorithm is implemented as follows:

$$\begin{aligned} \frac{\partial T_a}{\partial t} &= \epsilon(V)(k_{T_a}(V - V_r) - T_a) + \beta e_n(\zeta), \\ e_n(\zeta) &= \begin{cases} APD_{\text{ref}}(\tau^*) - APD_{n-1}(\zeta), \text{ if } \rho > 0 \\ \\ 0, \text{ if } \rho \leq 0 \end{cases} \end{aligned} \tag{5.13}$$

where β is the controller gain, and $\rho = APD_{\text{ref}}(\tau^*) - APD_{n-1}(\zeta)$. The error $e_n(\zeta)$ is generated from the difference between APDs references ($APD_{\text{ref}}(\tau^*)$) recorded between the time we reach τ^* and the following beat, over local area under control, and the APDs at the $(n-1)$-th stimulus (APD_{n-1}), over the same area length. This means that the mechanical properties of cardiac tissue are perturbed as a result of T_a perturbation (an additional term given by $\beta e_n(\xi)$ is added into T_a) when $e_n(\xi)$ is not null. The reader can refer to [51] for more details.

This basic feedback algorithm takes $e_n(\zeta)$ and provides a control signal which is applied over the region under control. The control signal is not null only when $e_n(\zeta) > 0$, meaning that the controller only acts on the short-APD. It is added as a positive quantity to Eq. (5.13), when the transmembrane potential crosses the threshold value, named V_{th}, during the repolarization phase at the n-th stimulus until the resting potential V_r. In the control algorithm, V_{th} is set to E_s, the reversal potential defined in Eq. (5.5). Therefore we can assume that I_{SAC} has the same sign (inward current) when control is activated. The controller acts after the electrical boundary feedback controller stabilizes a finite part of the tissue length (≈ 1 cm).

For the NHS model, the spatially distributed mechanical perturbation control algorithm is implemented as follows:

$$\frac{dw_1}{dt} = g_1(w_1, \lambda, \frac{d\lambda}{dt}, [\text{Ca}^{2+}]_{\text{i}}, T_a) + \beta_1 e_{1n}(\zeta),$$

$$e_{1n}(\zeta) \;=\; \begin{cases} APD_{\text{ref}}(\tau^*) - APD_{n-1}(\zeta), \text{ if } \rho > 0 \\ \\ 0, \text{ if } \rho \leq 0 \end{cases} \tag{5.14}$$

where β_1 is the controller gain, and $\rho = APD_{\text{ref}}(\tau^*) - APD_{n-1}(\zeta)$. The functionality of $e_{1n}(\zeta)$ is the same as $e_n(\zeta)$. Also, in this model the controller acts after the electrical boundary feedback controller stabilizes approximately 1 cm of the tissue length.

5.4 Theoretical analysis

In this section, we analyze the effects of the mechanical perturbation algorithm on the dynamics of the map model that couples the membrane voltage and active tension systems at the cell level. Therefore, we introduce a 2D iterative maps of the beat-to-beat dynamics, and a discrete form of the proposed control algorithm that can be incorporated in the coupled map model is derived. Then, we perform stability analysis of the system of the coupled maps. This analysis is performed using the SVNP model, which describes qualitatively consistent timing and amplitude of cardiac tissue contraction [144]. While the active cell tension is better represented using the NHS model that accurately describes the relationship between the intracellular calcium transient and tension, the selection of the SVNP model is made due to the simplicity of the governing equations of this model, where a discrete form of the control algorithm can be derived. In addition, in this study, we are investigating the effects of mechanical perturbation (stretch-based control algorithm) on alternans to gain insight into the effectiveness of the control algorithm, that have been confirmed by numerical experiments, using both SVNP and NHS models of active tension. While these two models do not generate the same quantitative results (shape and magnitude) of I_{SAC}, which causes either the lengthening or shortening of the action potential as discussed in the next section, qualitatively similar results of I_{SAC} (approximately proportional increases or decreases of I_{SAC} from beat to beat) are obtained for both models.

5.4.1 Map model development

The electrophysiology of a cell experiences feedback from tissue deformation, which activates stretch sensitive ion channels, is described in Section 2. Therefore, I_{SAC} (Eq. (5.5)), which is a function of two variables λ (Eq. (5.5)) and V (Eq. (5.7)), should be expressed only in terms of V and T_a (Eq. (5.8)), to have direct coupling between voltage and active tension. To this end, an approximation of λ in terms of T_a is given in Appendix A. Thus, λ as given in Eq. (13.S) is a function of T_a only, and the simplified description of I_{SAC}, after replacing the approximate value of λ in Eq. (5.5), becomes a function of V and T_a. Therefore, the simplified fully coupled electromechanical cell (CEC) model is constituted by Eqs. (5.7), (5.8), (5.5), and (13.S).

In the following, we check the effectiveness of mechanical and electrical perturbation controls in suppressing the alternans using the simplified CEC model. For numerical demonstration, a 1D cardiac cable of length L = 1 cm, and fixed at end points is considered. The step sizes and parameters of this model are given in Section 5 and in Tables 5.1 and 5.2. The APD alternans is induced by pacing the cable in the middle with PCL = 200 ms until steady state is reached. Electrical perturbation control is given in Eq. (5.12) with $\gamma = 0.15$, and mechanical perturbation control is given in Eq. (5.13), and $e_n(\zeta)$ takes the form given by Eq. (65) in [97], and therefore we obtain:

$$\begin{aligned} \frac{\partial T_a}{\partial t} &= \epsilon(V)(k_{T_a}(V - V_r) - T_a) + \beta e_n(\zeta), \\ e_n(\zeta) &= \begin{cases} APD_n(\zeta) - APD_{n-1}(\zeta), \text{ if } \rho < 0 \\ \\ 0, \text{ if } \rho \leq 0 \end{cases} \end{aligned} \tag{5.15}$$

where $\epsilon(V)$ is defined in Eq. (5.8). The values of original parameters of $\epsilon(V)$, given in [55], are modified (see Table 5.1), in order to take into account time delay as illustrated in Fig. 2(a) in [30]. The controller gain β is chosen to be -0.002. Therefore, in both control algorithms (electrical and mechanical), we have the same error signal which is generated by the difference between two consecutive APDs. In the case of electrical control, the pacing interval is being perturbed, while in the case of mechan-

ical control, we are perturbing T_a. As shown in Fig. 5.2, the alternans is suppressed

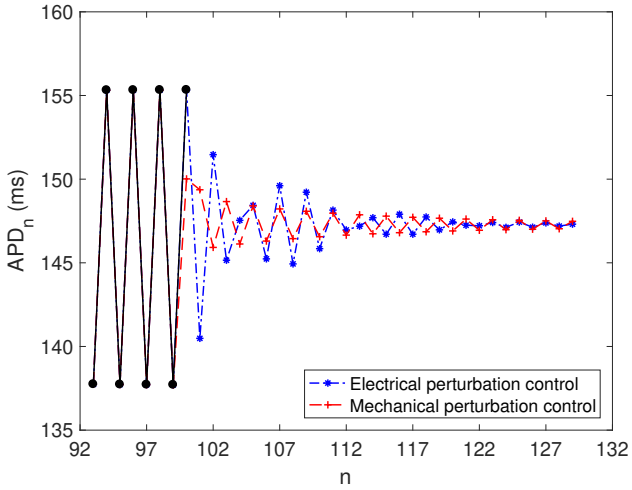

Figure 5.2: Evolution of the APD versus the beat number (n) of a single cardiac cell in the middle of the cable of length L = 1 cm, when it is paced at the center with PCL = 200 ms until steady state is reached (black line), using the CEC model (Eqs. (5.7), (5.8), (5.5), and (13.S)) where FOX model is used to represent electrical activity, with parameters given in Section 5 and in Tables 5.1 and 5.2. Evolution of APD versus n, when mechanical perturbation control (red dashed line), or electrical perturbation control (blue dash-dot line), applied at beat 100, are obtained using the CEC model except that Eq. (5.15) (with $\beta = -0.002$) is used instead of Eq. (5.8) for the case of mechanical control, and Eq. (5.12) (with $\gamma = 0.15$) is added to the CEC model for the case of electrical control.

(no alternation in the APD at steady state), when control (electrical or mechanical) is activated. While both control algorithms have successfully suppressed alternans at a single cardiac cell, their effectiveness at the tissue level is not equal, since, among other things, a spatially extended electrical perturbation algorithm for controlling alternans is not feasible, see [51] for details.

The second step in this development is to introduce a 2D discrete map describing the coupled dynamics of the membrane voltage and the active tension. The APD alternans can be mathematically described using the following discrete map:

$$APD_n = F(DI_{n-1}) \tag{5.16}$$

The relation in Eq. (5.16), known as APD restitution, relates APD at beat n (APD_n) with DI at beat $n-1$ (DI_{n-1}). It dictates that a shortened (prolonged) DI at a given beat will be followed by a shortened (prolonged) APD at the next beat. The interval

T^n (Eq. (5.12)) can be written as $T^n = APD_n + DI_n$. At a constant PCL, where $T^n = \tau$ for all n, prolonging a given APD will shorten the following DI, and therefore the next APD is shortened. APD restitution is usually measured using an S1S2 pacing protocol. In the S1S2 protocol, the cell is paced at a fixed cycle length S1 until steady-state is reached, and then a premature S2 stimulus is applied to elicit an extra beat. This S1S2 stimulus train is repeated and the S2 intervals are shortened each time until conduction block occurs. Theoretical studies have indicated that the periodic fixed point of Eq. (5.16) corresponding to the stable 1:1 rhythm undergoes a period-doubling bifurcation (2:2 rhythm), leading to the APD alternation, when the slope of the APD restitution curve is greater than one. It has to be noted that in large tissues, while most of the tissue may follow a 2:2 response, some regions can develop into higher-order rhythms such as 4:4 and 8:8 during fast pacing. However, several experimental results have shown that this hypothesis (slope > 1) fails to predict the onset of alternans when other factors, such as calcium cycling, have a strong influence on action potential. Therefore, in [75, 77], a 2D iterative maps are used to explore the effects of coupling between voltage and intracellular calcium transients, and is given by:

$$\begin{aligned} APD_n &= Fc_1(APD_{n-1}, \mathrm{Ca_n}), \\ \mathrm{Ca_n} &= Fc_2(APD_{n-1}, \mathrm{Ca_{n-1}}), \end{aligned} \tag{5.17}$$

which relates the APD_n at a given beat to the APD_{n-1} at previous beat, due to the APD restitution (Eq. (5.16)), and the peak $\mathrm{Ca_n}$ (Fig. 5.1) of the same beat, due to the effects of calcium-sensitive membrane currents, and relates the $\mathrm{Ca_n}$ at a given beat to the APD_{n-1} and the peak $\mathrm{Ca_{n-1}}$ at previous one. The Ca^{2+} modulates membrane currents through the $\mathrm{Ca}^{2+} \rightarrow V$ coupling, affecting the APD, and as dictated in Eq. (5.17), the coupling from Ca^{2+} to V occurs during the concurrent beat. The situation where APD and Ca^{2+} alternans are in phase, the case where long and short APD correspond to large and small Ca^{2+} respectively, is referred to as electromechanically concordant (EMC) alternans [75] (Fig. 5.1(a)). The opposite situation is known as electromechanically discordant (EMD) alternans (Fig. 5.1(b)).

To take into account the effects of MEF, and based on numerical experiments of the CEC model (Eqs. (5.7), (5.8), (5.5), and (13.S)) where FOX model is used to

represent electrical activity, with parameters given in Section 5 and in Tables 5.1 and 5.2, we use a semi implicit formulation of 2D maps that relates the APD and the active tension duration (ATD) (Fig. 5.3), and is given by:

$$\begin{aligned} APD_n &= F_1(APD_{n-1}, ATD_n), \\ ATD_n &= F_2(APD_{n-1}, ATD_{n-1}), \end{aligned} \tag{5.18}$$

where ATD_n (lower part of Fig. 5.3) is the T_a width at beat n, measured from the

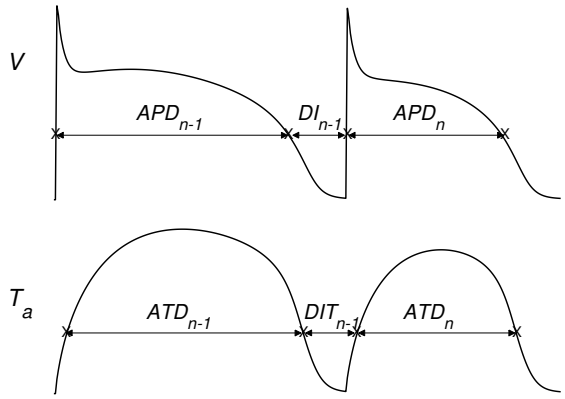

Figure 5.3: Schematic representation of membrane voltage and active tension, illustrating the APD and the ADT, using the CEC model where FOX model is used to represent the electrical activity, in the presence of alternans.

instant when T_a crosses the threshold value on the wave front, until the instant it falls below the threshold value on the wave back, and APD_n (upper part of Fig. 5.3) is the V width at beat n, measured from the instant when V crosses the threshold value on the wave front, until the instant it falls below the threshold value on the wave back. Similarly to the APD in Eq. (5.17), the APD of the current beat (APD_n) (Eq. (5.18)) is a function of both the previous APD (APD_{n-1}) and the concurrent ATD (ATD_n), due to the effects of I_{SAC} that changes the repolarization of membrane voltage. Also in this model, the coupling from active tension to voltage ($T_a \rightarrow V$ coupling) occurs during the concurrent beat. Note that the 2D maps (Eq. (5.18)) is also valid when NHS model is used, but the width of T_a (ATD_n) at beat n needs to be replaced by the T_a transient peak (ATP_n).

5.4.2 Discrete form of the control algorithm

A discrete form of mechanical perturbation control algorithm that can be incorporated in the 2D maps (Eq. (5.18)) is derived in the following manner.

To compute the current value of T_a at a single point in space, we discretize Eq. (5.8) in time k using an explicit forward Euler scheme. The closed-form expression for T_a reads:

$$\begin{aligned} T_a^k &= T_a^{k-1} + \Delta t\ \epsilon(V^{k-1})\ (k_{T_a}(V^{k-1} - V_r) - T_a^{k-1}), \\ \epsilon(V^{k-1}) &= \epsilon_0 + (\epsilon_\infty - \epsilon_0)\ \exp[-\exp(-\xi(V^{k-1} - V_s))] \end{aligned} \tag{5.19}$$

When control is activated, the current value of active tension, named T_a^{pert}, is perturbed, by adding the term $\Delta t\ \beta\ e_n$ ($e_n = APD_{\text{ref}}(\tau^*) - APD_{n-1}$ (Eq. (5.13))), into the right-hand side of Eq. (5.19), and therefore, at beat n, we can equivalently write:

$$ATD_n^{pert} = ATD_n + \alpha\ (APD_{\text{ref}}(\tau^*) - APD_{n-1}), \tag{5.20}$$

where ATD_n^{pert} is the width of T_a^{pert} at beat n, and α is a parameter that depends on β. Note that the discrete form of T_a (Eq. (5.20)), expressed in its ATD form, states that the control signal is delivered in a given beat when control is activated. On the other hand, continuous-time control law is implemented (Eq. (5.13)), which means it is defined over a continuous time interval in a given beat.

5.4.3 Stability analysis

In this section, we present linear stability analysis of the 2D iterative maps describing the coupled dynamics of voltage and active tension and incorporating mechanical perturbation control derived in its discrete form. The system's behavior of the open-loop or controlled coupled maps, close to the alternans bifurcation, can be accessed from the eigenvalues of the Jacobian matrix of the system. First, we linearize the system (Eq. (5.18)) around the period-1 fixed point (APD_*, ATD_*) by letting $APD_{n-1} = APD_* + \delta APD_{n-1}$ and $ATD_{n-1} = ATD_* + \delta ATD_{n-1}$, see Appendix B, and we obtain:

$$\delta X_n \approx J\ \delta X_{n-1}, \tag{5.21}$$

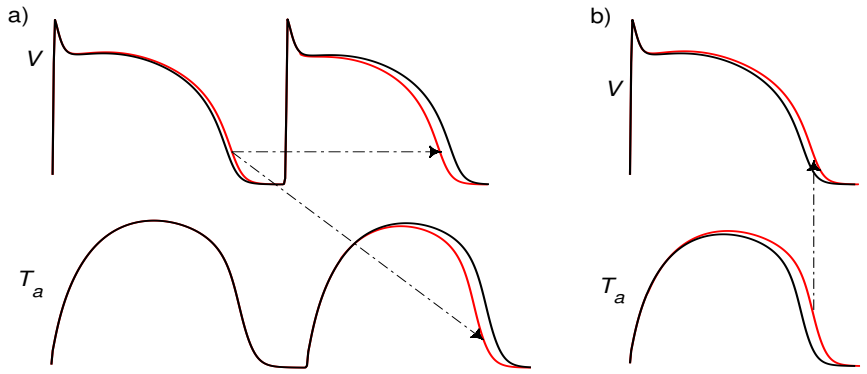

Figure 5.4: (a) Illustration of APD restitution relation and graded release coupling in CEC model. An increase in the APD (red line) at a given beat leads to a decrease in the APD (red line) and ATD (red line) at the next beat (due to a shortening of the DI), and vice versa. (b) Illustration of $T_a \rightarrow V$ coupling in CEC model. An increase in the ATD (red line) at a given beat tends to prolong the APD (red line) of that beat (due to the effects of I_{SAC}). FOX model is used to represent the electrical activity in CEC model.

where $\delta X_n = [\delta APD_n, \delta ATD_n]^T$, and J is the Jacobian of the two-variable map evaluated at the fixed point (APD_*, ATD_*), and is given by:

$$J = \begin{pmatrix} \frac{\partial APD_n}{\partial APD_{n-1}} + \frac{\partial APD_n}{\partial ATD_n}\frac{\partial ATD_n}{\partial APD_{n-1}} & \frac{\partial APD_n}{\partial ATD_n}\frac{\partial ATD_n}{\partial ATD_{n-1}} \\ \\ \frac{\partial ATD_n}{\partial APD_{n-1}} & \frac{\partial ATD_n}{\partial ATD_{n-1}} \end{pmatrix} \tag{5.22}$$

which describes the system's behavior around its fixed point (APD_*, ATD_*). The signs of the elements of J play an important role in the stability of J, hence, descriptions of all the terms of the Jacobian matrix for the case of CEC model, are given below. In all numerical experiments, we assume voltage-driven alternans in which APD alternans is caused by instabilities originating from voltage, and that the width variations of V and T_a occur when V crosses E_s, since control is activated only when V crosses E_s. If only voltage is coupled to tension (one way coupling), it is the case of a cardiac electromechanical model when MEF is neglected ($I_{SAC} = 0$), $-J_{11}$ simply measures the slope of the APD restitution relation (Eq. (5.16)), since when $I_{SAC} = 0$, we have $\partial APD_n/\partial ATD_n = 0$, and consequently $J_{11} = \partial APD_n/\partial APD_{n-1} = -\partial APD_n/\partial DI_{n-1}$. When the slope is larger than unity, which corresponds here to the condition $J_{11} < -1$, APD alternans occurs and induces

ATD alternans, see also discussion in Section 5. In turn, J_{22} measures degree of instability of the tension system in CEC model, and is negative but greater than -1, since in our case ATD-alternans is secondary to APD-alternans. The term $\partial APD_n/\partial ATD_n$ measures dependence of the voltage on the tension, and is positive in CEC model (Fig. 5.4(b)). This is equivalent to the so called positive ($T_a \rightarrow V$ coupling), which states that a prolongation (shortening) in ATD will prolong (shorten) concurrent APD, and means that an increase (decrease) in ATD has a net depolarizing (hyperpolarizing) effect on voltage. Since $\partial ATD_n/\partial ATD_{n-1} = J_{22}$ is negative and $\partial APD_n/\partial ATD_n$ is positive, one can conclude that $J_{12} = (\partial APD_n/\partial ATD_n)(\partial ATD_n/\partial ATD_{n-1})$ is negative. The term $\partial ATD_n/\partial APD_{n-1} = J_{21}$ measures the dependence of each beat's ATD on the preceding APD ($V \rightarrow T_a$ coupling), called graded release, and is negative in CEC model (Fig. 5.4(a)). It states that a prolongation of the preceding APD (APD_{n-1}) will cause a shortening in the subsequent ATD (ATD_n), and vice versa.

The stability of the system of coupled maps (Eq. (5.18)) is governed by the eigenvalues of the Jacobian matrix. The eigenvalues of the matrix J are given by:

$$\lambda_1 = \frac{1}{2}(J_{11} + J_{22} + \sqrt{(J_{11} - J_{22})^2 + 4J_{12}J_{21}}),$$
$$\lambda_2 = \frac{1}{2}(J_{11} + J_{22} - \sqrt{(J_{11} - J_{22})^2 + 4J_{12}J_{21}}). \tag{5.23}$$

The period-1 fixed point is stable provided that the absolute value of the largest eigenvalue of J, which is λ_2, is smaller than one. If $\lambda_2 < -1$, the fixed point goes unstable and a period-doubling bifurcation occurs, corresponding to the onset of alternans.

To analyze the effect of the mechanical perturbation control on the system of coupled maps, we model the effects of mechanical control on the elements of J (Eq. 5.22), by incorporating its discrete form (Eq. (5.20)) in J. The new Jacobian matrix called J^c is given as:

$$J^c = \begin{pmatrix} J_{11} - \alpha \frac{\partial APD_n}{\partial ATD_n} & J_{12} \\ \\ J_{21} - \alpha & J_{22} \end{pmatrix} \tag{5.24}$$

where α is not null when control is activated, otherwise it is set to zero. Mechanical perturbation control will thus affect two elements in J^c ($J^c_{11} = J_{11} - \alpha\,(\partial APD_n/\partial ATD_n)$ and $J^c_{21} = J_{21} - \alpha$). Therefore, we analyze the effect of these two elements on the

stability of the system. Let us assume that at the beat n the control is activated, the APD dynamics manifested by $\partial APD_n/\partial APD_{n-1}$ can be stabilized with negative α, since $\partial APD_n/\partial ATD_n$ is positive (discussed above). Likewise, the $V \rightarrow T_a$ coupling manifested by $\partial ATD_n/\partial APD_{n-1}$ will become weaker with negative α and $\partial ATD_n/\partial APD_{n-1} - \alpha$ remains negative. We can illustrate this by calculating the eigenvalues of J^c, which are given by:

$$\lambda_1^c = \frac{1}{2}(J_{11}^c + J_{22} + \sqrt{(J_{11}^c - J_{22})^2 + 4J_{12}J_{21}^c}),$$
$$\lambda_2^c = \frac{1}{2}(J_{11}^c + J_{22} - \sqrt{(J_{11}^c - J_{22})^2 + 4J_{12}J_{21}^c}), \tag{5.25}$$

where (J_{12},J_{22}) are elements of J, (they are used in Eq. (5.25), since they do not

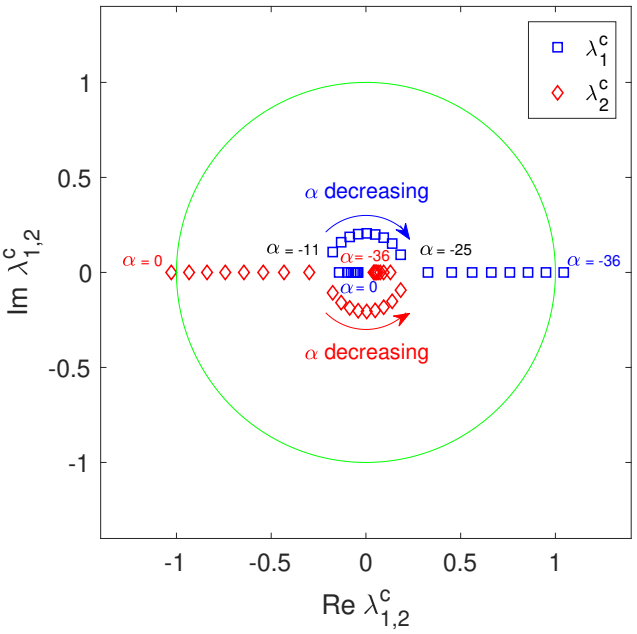

Figure 5.5: Diagram of the two eigenvalues (the imaginary and real parts of $\lambda_{1,2}^c$) of the Jacobian matrix J^c for various values of α. $\lambda_{1,2}^c$ are calculated using the model (Eqs. (5.7), (5.8), (5.5), and (13.S)) where FOX model is used to represent the electrical activity, with parameters given in Section 5 and in Tables 5.1 and 5.2. The 1D tissue is paced at the center with PCL = 207 ms, and the terms that constitute the elements of J are evaluated at the period-1 fixed point. For $\alpha = 0$ (no control is applied), the absolute value of the largest eigenvalue of J^c ($|\lambda_2^c|$), which is a measure of the stability of the fixed point, is greater than 1. When $\alpha < 0$, the absolute value of λ_2^c is decreased and λ_1^c is increased. For $\alpha <= -36$, λ_1^c , which becomes the largest eigenvalue of J^c when $\alpha < -25$, is greater than one. Both eigenvalues become complex when $\alpha < -11$ and $\alpha > -25$.

depend on α). For certain values of α, as shown in Fig. (5.5), the absolute value of the largest eigenvalue is smaller than one. The properties of the 2D discrete maps determine the range of α, and consequently the controller gain β (defined in Eq. (5.13)), which provides effective control. As demonstrated above, the mechanical perturbation control is effective in controlling alternans at the cellular level. In the next section, the suppression of alternans at the tissue level will be numerically demonstrated.

Table 5.1: Parameter values used in SVNP model

Active tension	$k_{T_a} = 0.34 \times 10^{-3}$ MPa mV^{-1}
Switch function	$\epsilon_0 = 1$ ms^{-1}, $\epsilon_\infty = 0.1$ ms^{-1},
	$\xi = 0.3$ mV^{-1}, $V_s = -70$ mV

5.5 Numerical Results and Discussion

We have simulated the control algorithms and successfully suppressed alternans using either SVNP or NHS models for the active tension generation with either Fox or LR1 models for the cardiac excitation described in Section 2. Therefore, for brevity, only numerical simulations obtained with NHS model and with either Fox or LR1 models, are presented and discussed in this section. The NHS model is chosen since the relationship between Ca^{2+} and T_a is more accurately described in this model. Thus, Eqs. (5.4),(5.5),(5.7), and (5.9) are used to constitute the two electromechanical models in this section. In all our simulations, a 1D cardiac cable of length $L = 6.25$ cm, fixed at end points is considered, which is consistent with an isometric contraction regime. In one dimension, the upper case indices (M, N) presented in Eq. (5.7) are set to one, and $D_{11} = \bar{D} = 0.001$ cm^2/ms is the diffusion constant, and $C_m = 1$ μF/cm^2 is the membrane capacitance. The electrical stimulus is applied as square wave pulses with a magnitude of 80 μA/μF and a duration of 1 ms. The same numerical schemes were applied in all simulations, where Eq. (5.7) was solved by a semi-implicit time integration scheme, and the Hodgkin-Huxley type equations for the gating variables in the ionic models (LR1, Fox) were integrated using the Rush and Larsen integration scheme [145]. The active tension generation (Eq. (5.9)) was solved using standard Euler scheme, and we determined the tissue deformation mechanics (Eq. (5.4)) using finite difference scheme. The step time $\Delta t = 0.005$ ms and step size $\Delta X = 0.0125$

cm are used in all simulations, and no-flux boundary conditions were imposed for Eq. (5.7). The parameters for all models, including cardiac mechanics, used in the simulation are given in Table 5.2.

Table 5.2: Values of the material parameters used for the models

Stretched-activated current	$G_s = 10\ \mu\text{S}\ \mu\text{F}^{-1}$, $E_s = -20$ mV, $\lambda_{max} = 1.1$
Mooney-Rivlin	$\tilde{c} = 0.4$ MPa.

Model 1: Using LR1 and NHS models

In the first electromechanical model, LR1 and NHS models are used to represent electrophysiological properties and active tension generation respectively. The LR1 [49] model, where the resting potential is about $V_r = -83.4$ mV, is used with modifications of the maximum conductances of the sodium current ($\overline{\text{G}}_{\text{Na}} = 16.0$ instead of 23.0), of the slow inward current ($\overline{\text{G}}_{\text{si}} = 0.06$ instead of 0.09), and of the time-dependent potassium current ($\overline{\text{G}}_{\text{K}} = 0.432$ instead of 0.282), so that the model is capable of showing alternans at a shorter cycle length. In this model, the gains $\gamma = 0.23$, $\beta_1 = -4.2 \times 10^{-4}$ are chosen.

The amplitude of alternans, $a_n(\zeta)$, is defined as the difference between two consecutive APDs at a given point in space ζ:

$$a_n(\zeta) = (APD_n(\zeta) - APD_{n-1}(\zeta))(-1)^n \tag{5.26}$$

To induce alternans, we pace the first 10 cells of the cable, located at one end from the pacing site ($\boldsymbol{P}$), at $\tau = 300$ ms, until a steady-state APD is reached, and gradually decreased τ from 300 to $\tau^* = 255$ ms. The pacing period was shortened in steps of 5 ms for $\tau > 260$ ms and in steps of 1 ms for $\tau < 260$ ms. When pacing with period $\tau^* = 255$ ms, the alternans (Fig. 5.6(a)) grows, and when the control action is applied at $t = 33000$ ms, over localized region under control (3.25 - 5 cm), it successfully suppresses alternans (Fig. 5.6(c)). The controller acts after the electrical boundary feedback controller stabilizes the area up to 1 cm from $\boldsymbol{P}$ (Fig. 5.6(b)). As seen in this figure, the electrical pacing control cannot achieve stability for the cables exceeding 1 cm, and hence the need for a model-based control algorithm that

combines the boundary pacing with the spatially distributed mechanical perturbation. As shown in Fig. 5.7, APDs alternate in a repeating long-short pattern when control is not applied (Fig. 5.7(a)) and are restored (normal APDs), in the area up to 1 cm from $\boldsymbol{P}$ (Fig. 5.7(b)), after the electrical control is applied at $\boldsymbol{P}$, and along the cable when both the electrical and mechanical perturbation controls are applied (Fig. 5.7(c)).

After applying the spatially-distributed mechanical perturbation control at $t =$ 33000 ms, the largest changes in I_{SAC} (Fig. 5.8(b)) with respect to I_{SAC}, when only the electrical boundary pacing control is applied (Fig. 5.8(a)), occur in the localized region (3.25 - 5 cm) where the control signal is applied. The mechanical perturbation control perturbs the tissue by exerting a force that causes deformation in the region under control, and as a result, the stretch distribution along the tissue changes, it increases in the region under control and decreases in other regions. This is because, since the sum of the length of all the line segments, when stretched (increased) or contracted (decreased), of the 1D cable, remains constant when both ends of the cable are fixed, see Appendix A, some segments are stretched, while others are contracted. Consequently, the magnitude of I_{SAC}, which is a function of stretch and voltage (Eq. (5.5)), when mechanical perturbation control is applied, increases in the localized region under control (3.25 to 5 cm from $\boldsymbol{P}$), and decreases elsewhere. As it can be seen in Fig. 5.8(d), the short APDs during one beat (the odd beats in Fig. 5.8(d)), in the area under control, are prolonged due to the I_{SAC}, which causes, according to the restitution relation (Eq. (5.16)), the shortening of APDs on the following beat (the even beats in Fig. 5.8(d)). It has to be noted that when control signal is applied, I_{SAC} is defined as an inward current, as discussed in Section 3.

The presence of electrical alternans induces, through the mechanism of the so-called excitation-contraction coupling, an alternation in the heart muscle contractile activity, see Fig. 5.9. The amplitude of tension alternates (Fig. 5.9(b)) when the APD alternates (Fig. 5.9(a)).

As shown in Fig. 5.10, the error signal decreases from around 20 ms when control is turned on to less than 3 ms at steady state, and the percentage variation in the magnitude of T_a perturbation, where T_a perturbation occurs as a result of $[Ca^{2+}]_{\text{Trpn}}$ perturbation, varies from around 10% when control is turned on, to less than 2%

at steady state (see Fig. 5.11). Note that, in real time experiment, perturbing $[Ca^{2+}]_{Trpn}$ by an amount equal to $\beta_1 e_{1n}(\xi)$, as described in Eq. (5.14), can be difficult to realize, since measurements of the $[Ca^{2+}]_{Trpn}$concentration may not be readily available, and therefore other means such as magnitude of applied force can be used to reconstruct amount of concentration of $[Ca^{2+}]_{Trpn}$ that needs to be applied. For example, massaging cardiac tissue can perturb $[Ca^{2+}]_{Trpn}$ (change its magnitude) since mechanical perturbation modifies $[Ca^{2+}]_i$ [146], which in its turn modifies the $[Ca^{2+}]_{Trpn}$ (Eq. (11)).

In summary, the control signal alters the tissue's transmembrane potential when mechanical perturbation is applied, in which changes in T_a affect the mechanical deformation term (displacement variable u in the elastic equation (5.4)), which then affects the transmembrane potential (Eq. (5.7)), through the conductivity tensor and stretch-activated current (Eq. (5.5)). Perturbing MEF alter the tissue's electric wave profile, and consequently the APD. Thus, the control of alternans in cardiac tissues of relevant size can be achieved by the manipulation of the electrical APD using a model based on the mechanical and electrophysiological properties of cardiac tissue.

Model 2: Using FOX and NHS models

FOX and NHS models are used in the second electromechanical model to represent electrophysiological properties and active tension generation respectively. The resting potential for FOX [48] model is about $V_r = -94.7$ mV, and the gains $\gamma = 0.19$, $\beta_1 = -7.4 \times 10^{-4}$ are chosen in Model 2.

The alternans is induced by pacing the first 10 cells from $\boldsymbol{P}$ of the cable, at $\tau = 300$ ms, until a steady-state APD is reached, and gradually decreased τ from 300 to $\tau^* = 192$ ms. The pacing period was shortened in steps of 5 ms for $\tau > 200$ ms and in steps of 1 ms for $\tau < 200$ ms. As shown in Fig. 5.12, the amplitude of alternans grows (Fig. 5.12(a)) when no control is applied, and when the control action is applied at $t = 25000$ ms, over localized region under control (3.25 - 5 cm), it successfully suppress alternans (Fig. 5.12(c)). The controller acts after the electrical boundary feedback controller stabilizes a small area (around 1 cm) from $\boldsymbol{P}$ (Fig. 5.12(b)). As can be seen in (Fig. 5.12(b)), $|a_n(\zeta, t)|$ exhibits ripples at the pacing boundary before

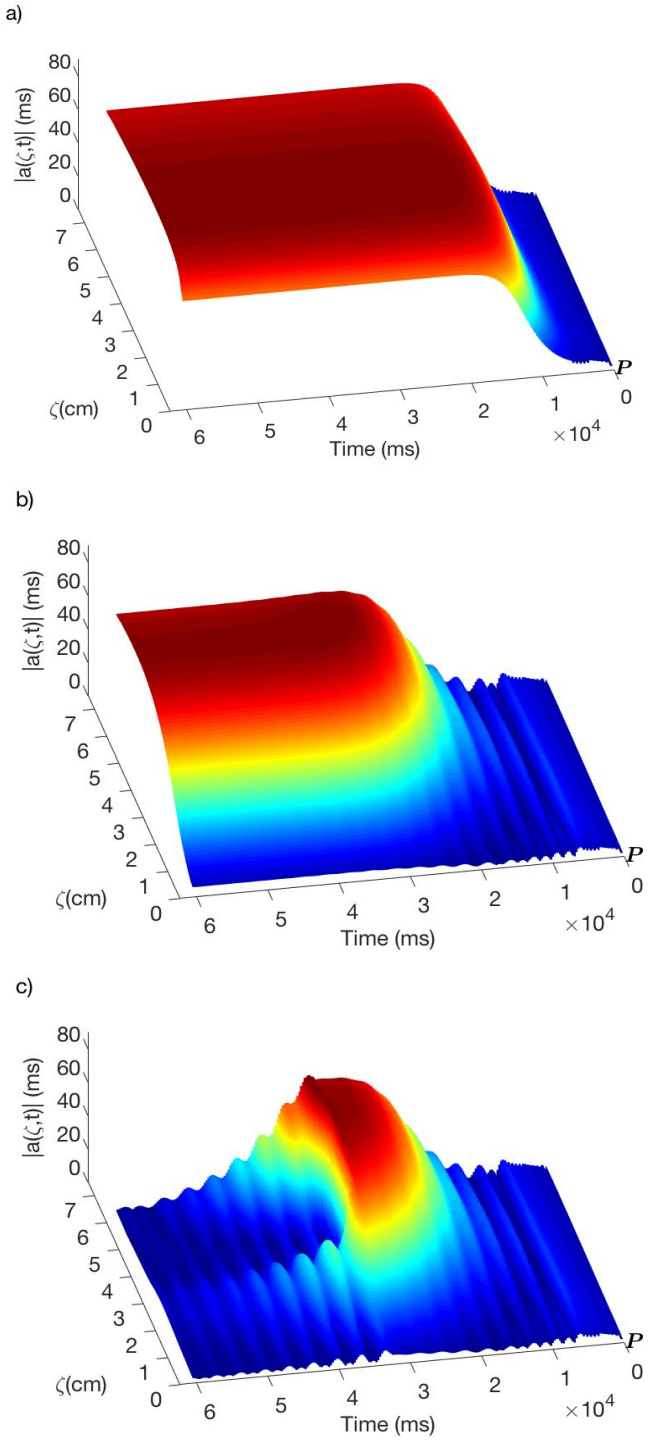

Figure 5.6: Magnitude of the amplitude of alternans for Model 1 when a 6.25 cm cable of cardiac cells, the first 10 cells to pacing site $\boldsymbol{P}$ (which corresponds to $\zeta = 0$), is paced at 255 ms, starting with period = 300 ms, and decreased gradually to period = 255 ms. The amplitude of alternans grows, shown in (a), when no control is applied, while (b) illustrates the alternans suppression by electrical pacing control applied at $\boldsymbol{P}$ when $\tau^* = 255$ ms is reached, while (c) illustrates the alternans suppression by electrical pacing control and spatially distributed mechanical perturbation control when the control action is applied at $t = 33000$ ms over localized region under control (3.25 to 5 cm from $\boldsymbol{P}$).

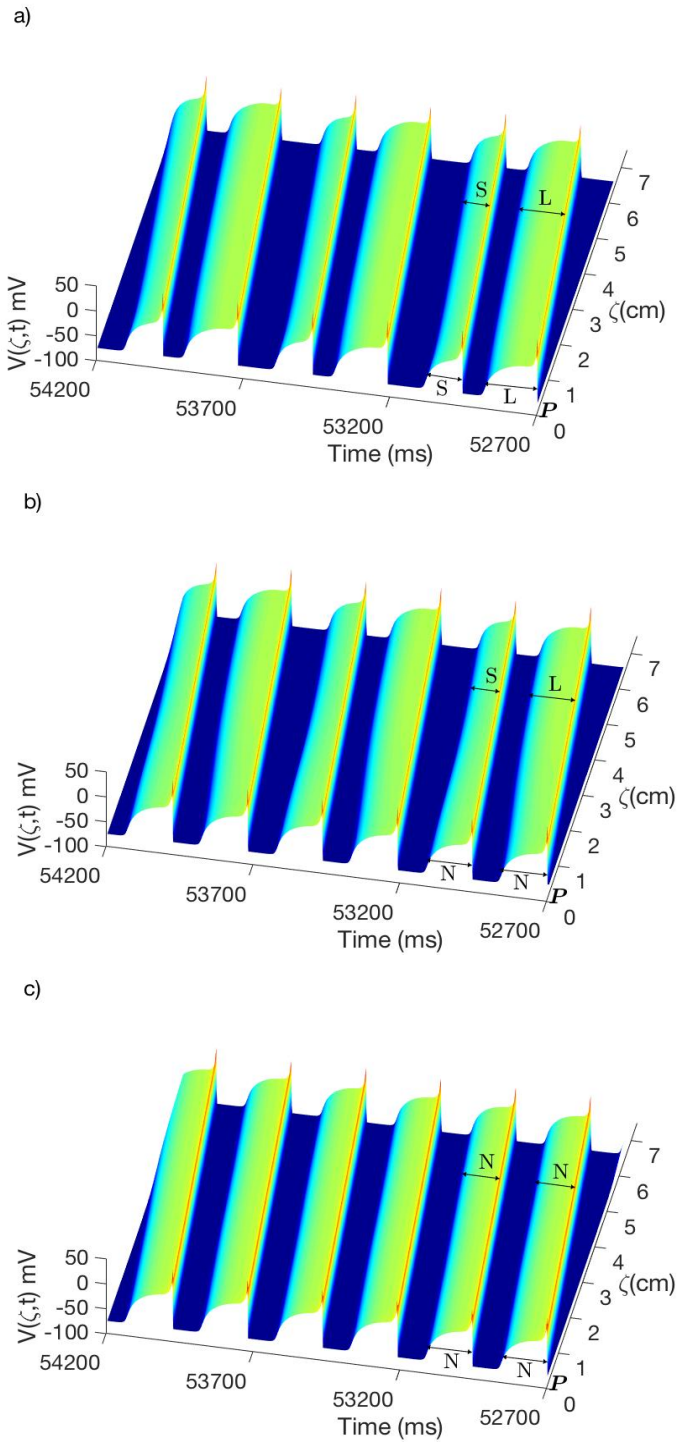

Figure 5.7: Time evolution of transmembrane potential for Model 1 before control is applied (a), APDs alternate in a repeating long-short (L-S) pattern, and after (b) electrical pacing control is applied at pacing site ($\boldsymbol{P}$), normal (N) APDs that are closed to $\boldsymbol{P}$ are restored, while (c) illustrates the restoration of normal APDs along the cable when electrical and mechanical perturbation controls are applied respectively at $\boldsymbol{P}$ and over localized region under control (3.25 to 5 cm from $\boldsymbol{P}$).

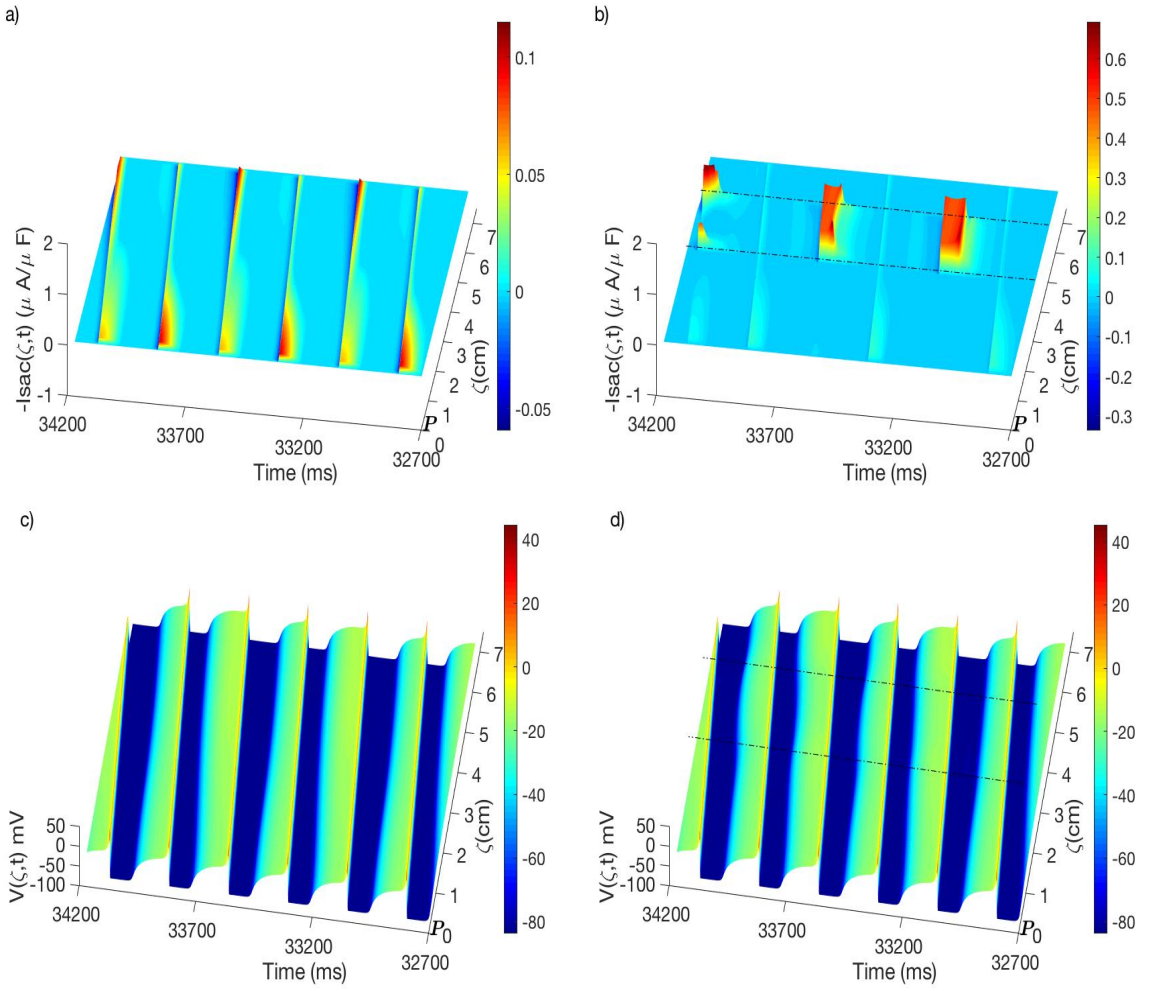

Figure 5.8: (a) and (c) are the time evolution of stretch-activated current (I_{SAC}) and membrane potential for Model 1, respectively, when only the electrical control is applied, and after (b,d) the mechanical perturbation control is also applied, at $t = 33000$ ms, over localized region under control (3.25 to 5 cm from $\boldsymbol{P}$). As seen in this figure, the largest changes in I_{SAC} (b) with respect to I_{SAC} (a), occur in the region (the region between the two dash-dot lines) where mechanical control is applied.

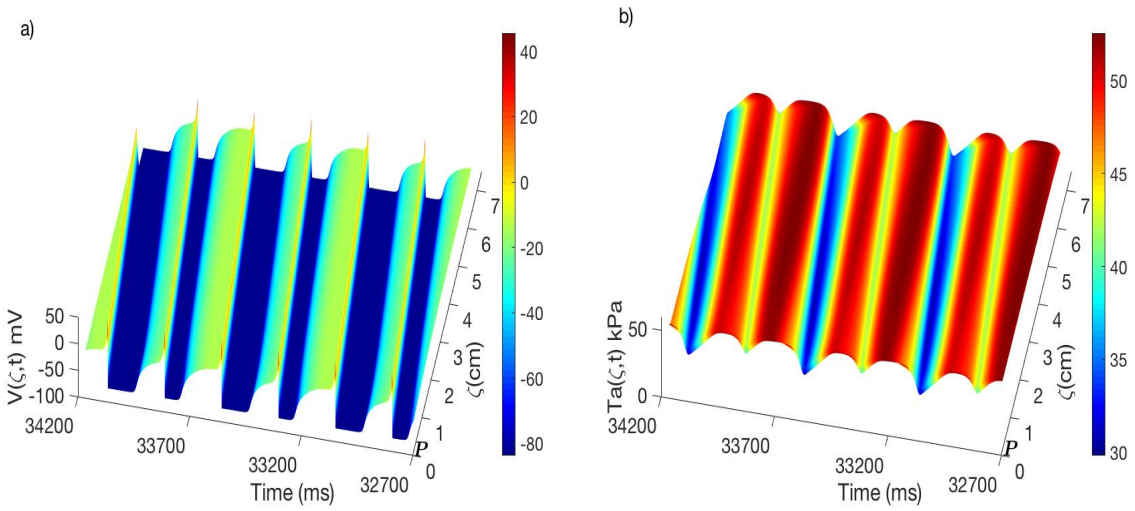

Figure 5.9: Time evolution of transmembrane potential variable (a), and active tension variable (b) for Model 1 in the presence of alternans. As seen above, the alternation in the APDs induces an alternation in the amplitude of tension through the mechanism of the so-called excitation-contraction coupling.

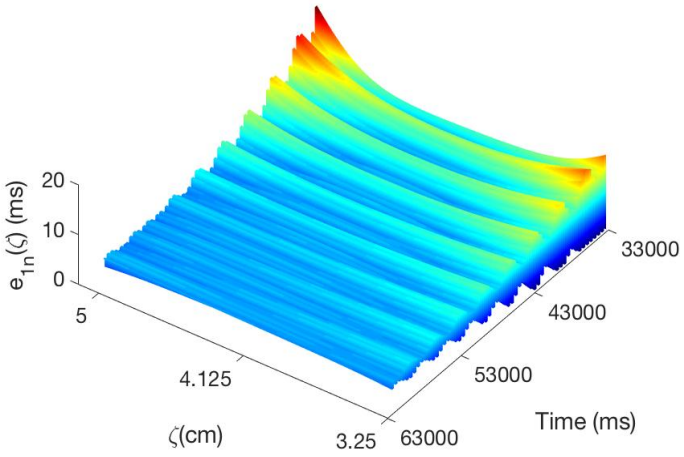

Figure 5.10: Time evolution of error signal (e_{1n}), defined in Eq. (14), for Model 1, when a spatially distributed mechanical control is applied over localized region under control (3.25 - 5 cm).

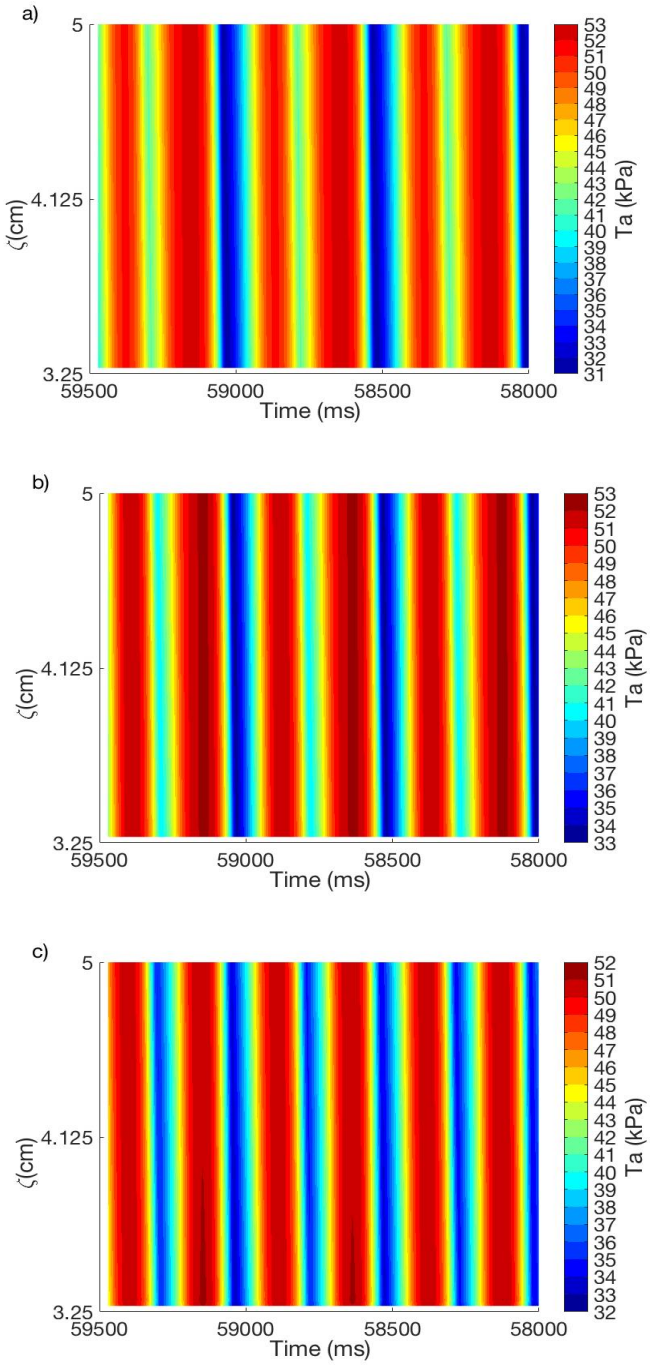

Figure 5.11: Time evolution of active tension variable (T_a) (Eq. (9)) in localized region under control (3.25 - 5 cm) for Model 1 when no control is applied (a), while (b) illustrates T_a evolution when only electrical pacing control is applied at pacing site when $\tau^* = 255$ ms is reached, while (c) illustrates the T_a evolution when electrical pacing control and spatially distributed mechanical perturbation control after the control is turned on at $t = 33000$ ms over localized region under control.

a steady state is reached, which is then transmitted along the cable. This is due to the pacing period of the dynamic feedback control (Eq. (5.12)) which varies over many different values depending upon the difference between the last two APDs recorded. The range of variation can be large, especially at the early stages after the control is applied, but when γ (the feedback gain in Eq. (5.12)) is better tuned, while satisfying the stability requirement [140], the oscillations decay faster. Also, in this model, it is demonstrated the need to combine the boundary pacing with the spatially distributed mechanical perturbation to successfully suppress alternans.

Similar results to Model 1 regarding the changes in stretch-activated current. As shown in Fig. 5.13, the largest changes in I_{SAC}, after the mechanical control is applied (Fig. 5.13(b)), with respect to I_{SAC}, when only the electrical control is applied (Fig. 5.13(a)), occur in the region under control. As can be seen in this figure, when mechanical control is turned on at $t = 25000$ ms, the magnitude of I_{SAC}, increases in the region under control for the odd and even beats, which differs from the I_{SAC} given in Model 1, where the magnitude of I_{SAC} (Fig. 5.8) increases only for the odd beats. This is because, although the APDs of the even beats remain longer than APDs of the odd beats in the region under control in Model 2, they are shorter than $APD_{\text{ref}}(\tau^*)$.

5.6 Summary and future works

The development of methods to suppress cardiac alternans has important clinical implications, due to the finding that TWA often precedes lethal arrhythmias, and is risk factor for SCD. We introduce a theoretical framework of 2D iterative maps that describe the cardiac excitation-contraction coupling. To this end, the stretch-activated current through the stretch-activated ion channels that mediate MEF is approximated in terms of the membrane voltage and the active tension. This allows us to study the effects of mechanical perturbation algorithm on the dynamics of a developed map model that couples the membrane voltage and active tension at the cellular level. A stability analysis of the system of coupled maps is performed by incorporating a discrete form of the control algorithm. We show that when the mechanical control is turned on, both the stability of APD dynamics and $V \rightarrow T_a$ coupling are affected.

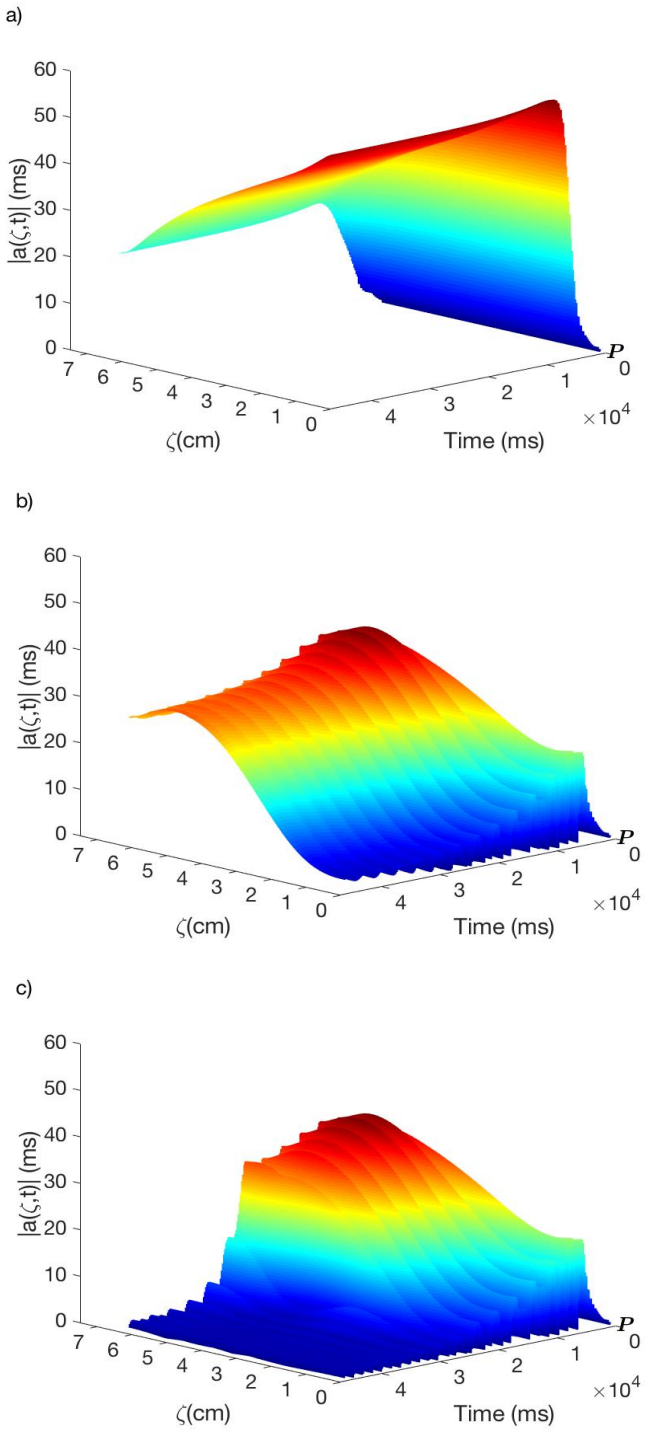

Figure 5.12: Magnitude of the amplitude of alternans for Model 2 when a 6.25 cm cable of cardiac cells, the first 10 cells to $\boldsymbol{P}$,is paced at 192 ms, starting with period = 300 ms, and decreased gradually to period = 192 ms. The amplitude of alternans grows, shown in (a), when no control is applied, while (b) illustrates the alternans suppression by electrical pacing control applied at $\boldsymbol{P}$ when $\tau^* = 192$ ms is reached, while (c) illustrates the alternans suppression by electrical pacing control and spatially distributed mechanical perturbation control when the control action is applied at $t = 25000$ ms over localized region under control (3.25 to 5 cm from $\boldsymbol{P}$).

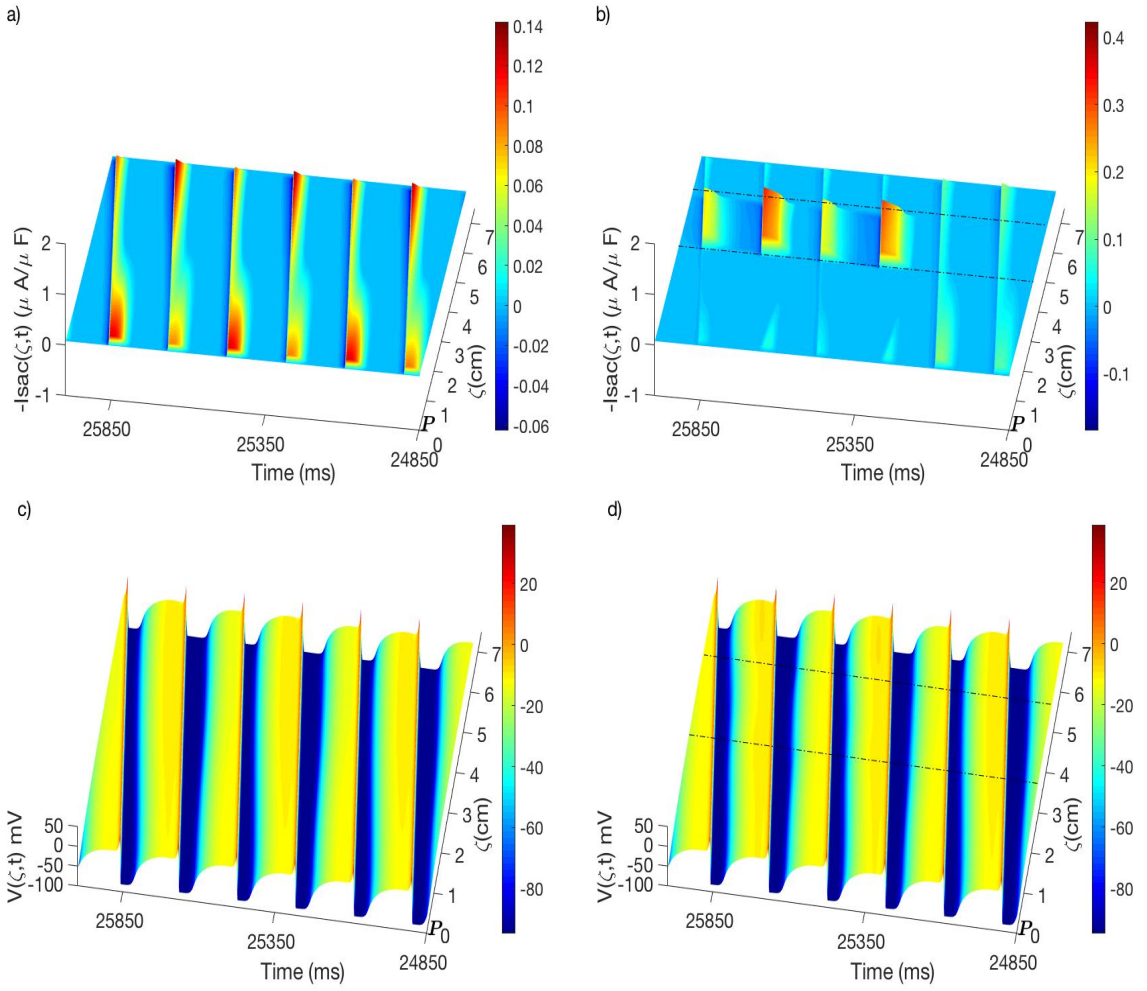

Figure 5.13: (a) and (c) are the time evolution of stretch-activated current (I_{SAC}) and membrane potential for Model 2, respectively, when only the electrical control is applied, and after (b,d) the mechanical perturbation control is also applied, at $t = 25000$ ms, over localized region under control (3.25 to 5 cm from $\boldsymbol{P}$). As seen in this figure, the largest changes in I_{SAC} (b) with respect to I_{SAC} (a), occur in the region (the region between the two dash-dot lines) where mechanical control is applied.

That is, the mechanical controller gain affects the eigenvalues of the Jacobian matrix of the system, and thus its stability. Therefore, with an appropriate choice of the gain, the system can be stabilized, and the alternans is suppressed.

The effectiveness of the mechanical perturbation algorithm is verified by employing a model of cardiac electromechanics. Two detailed ionic models of cardiac cell electrophysiology, namely Luo-Rudy 1 and Fox models, are used, and passive mechanical properties of cardiac muscle are described using the Mooney-Rivlin passive elasticity model. Active tension that couples the cardiac mechanics with excitation is generated using a smooth variant of the Nash-Panfilov model and the Niederer-Hunter-Smith model. The control algorithm is demonstrated to successfully suppress aternans in a 1D cable of cardiac cells using numerical simulations. If the mechanical perturbation algorithm is incorporated into a mechanical-based device that can be equipped with mechanical patch, such as [134], alternans rhythms can be suppressed before they become fatal rhythm disorders.

When I_{SAC} is applied over a localized region of tissue (chosen by trial and error in our experiments), the spatially distributed mechanical perturbation algorithm successfully suppresses alternans along the tissue. The remaining questions are: what is the minimum mechanical patch size necessary and where should the patch be positioned to control alternans? These questions will be addressed in future studies. In addition, tissue anisotropy and fiber orientation will be taken into account when higher-dimensional computational heart models are considered. These factors will affect the distribution of fiber stretch along the tissue, and consequently the magnitude of I_{SAC}, which depends on the amount of stretch generated. We expect the size and position of the adhesive patch will influence the magnitude of the mechanical perturbation applied. The majority of studies have neglected the time-dependent inertial term in the equations governing cardiac mechanics (see [147] for a demonstration), therefore, in this work, the inertia term was neglected. But recently [148], it has been shown that the deformations due to inertia may alter the dynamics of excitation waves via the MEF, therefore, this term may be incorporated in future studies.

Chapter 6

Conclusions and Future Directions

In the thesis, we studied the effects of mechano-electrical feedback on the dynamics of alternans using electromechanical models of cardiac tissue, and we developed a model-based control algorithm combining an electrical boundary pacing and a spatially distributed mechanical perturbation.

6.1 Conclusions

The effects of mechano-electrical feedback (MEF) on the onset of alternans, also known as period-doubling bifurcation, in a 7 cm cable were studied in Chapter 2. A 1D biophysically detailed electromechanical model of cardiac tissue was employed where the phase one of the Luo-Rudy model was used to represent the electrophysiological properties, while the mechanical properties of passive myocardium are described using the Mooney-Rivlin material model. The active tension that couples the electrophysiological model to the cardiac mechanics model is generated using the Niederer-Hunter-Smith model. We showed that the distribution of stretching along the cable is not uniform and that the stretch behavior, which varies with pacing period, along with the stretch-activated current (I_{sac}) model parameters, determine the effect of I_{sac} on the APD. In addition, a theoretical framework of 2D iterative maps that incorporate the effects of I_{sac} was used to demonstrate the MEF effects on the period-doubling bifurcation, corresponding to the onset of alternans in a single cardiac cell. In particular, we showed that critical pacing period, that corresponds to the onset of alternans when MEF is not present, can be shifted to lower values, where the degree of this shift depends on the strength of I_{sac}. In this work, only a certain

range of pacing periods, that are closed to the critical pacing period, were considered, and a restriction was put on the value of the I_{sac} conductance parameter so that the effects of MEF on the conduction velocity (CV) restitution can be neglected.

In Chapter 3, we studied the effects of MEF on the dynamics of alternans when no restrictions were imposed on the model conductance value. The whole range of pacing periods that correspond to alternans was considered. The same electromechanical model used in Chapter 2, was employed in this work, with the exception that the electrophysiological properties in the heart were represented by FOX model. We presented the effect of MEF on the APD and CV restitution curves, and showed that while its effect on the APD restitution is insignificant, it can modify the slope of CV restitution curve when large values of I_{sac} conductance parameters are used. The changes in CV along the cable, due to I_{sac}, has a role in converting spatially concordant alternans into discordant alternans. We also showed that, when alternans is discordant, the spatial dispersion of refractoriness is increased in the presence of MEF, by forming a second nodal point in the cable of cardiac cells. We also have found that MEF may lead to a conduction block for some values of I_{sac} model parameters.

In Chapter 4, we presented a model-based algorithm for alternans control using the Nash-Panfilov electromechanical model. Our control strategy is based on combining the electrical boundary pacing with the spatially distributed mechanical perturbation algorithms. A novel mechanical perturbation algorithm to control alternans was presented in this study. The mechanical perturbation algorithm manipulates the cardiac tissue mechanics in order to suppress alternans. The proposed algorithm suppresses alternans in relevantly sized cardiac tissues. Numerical simulations were presented to demonstrate successful suppression of alternans in a cable of length equal to 6.25 cm using the proposed control algorithm.

The control algorithm proposed in Chapter 4, was implemented and tested using two realistic electromechanical models of cardiac tissue in Chapter 5. The APD was altered by perturbing cardiac tissue mechanics. Perturbing cardiac tissue mechanics in a small region of the tissue alters the tissue's electric wave profile, and consequently the APD, via MEF in order to suppress alternans. The inclusion of spatially distributed mechanical perturbation control, have overcome the limitation in controllability of the electrical pacing control to suppress alternans in relevantly

sized cardiac tissues. In addition, we analyzed the effects of mechanical perturbation algorithm on the dynamics of the map model that couples the membrane voltage and active tension systems at the cell level using a 2D iterative map of the beat-to-beat dynamics, and a discrete form of the proposed control algorithm. It was demonstrated to successfully suppress alternans in a one-dimensional cable of cardiac cells using numerical simulations.

6.2 Future Directions

A natural extension of the work presented in this thesis is to apply the control algorithms to two- or three-dimensional cardiac tissue. The location(s) and size of patch(s) that can be placed in 2D or 3D tissue, so that mechanical perturbation algorithm can be applied, need to be investigated by means of numerical simulations. The proposed control algorithm is a promising approach that can be possibly incorporated into mechanical-based devices to suppress alternans.

In this work, we showed that MEF can convert concordant alternans into discordant in one-dimensional tissue, however, in higher dimensions, the discordant alternans has been shown to induce the formation of reentrant spiral waves, which cannot be formed in one dimension, and this may break down further leading to multiple wavelets, corresponding to the onset of lethal arrhythmias such as VF. Therefore, studying the mechanisms underlying the transition from discordant alternans at the 2D or 3D tissue, due to MEF, into a reentry wave, and how this further evolves into lethal cardiac arrhythmias is of great interest in research fields dealing with cardiac mechano-electric feedback and arrhythmias.

The formation and destabilization of spiral waves initiate VF. Therefore, terminating reentrant spiral waves is of great interest to cardiac disease researchers. We studied the effects of MEF on spiral wave dynamics using mechanical perturbation approach. We showed that MEF leads to spiral wave drift when the tip of the spiral wave hits any of the boundaries of the perturbed region where the mechanical perturbation is applied. Therefore, MEF, in the localized region under mechanical perturbation, can induce drift of spiral tip which is responsible for certain lethal cardiac arrhythmias. This was shown in our preliminary results presented in Biomedical Engineering

Society annual meeting (Effects of Mechanical Perturbations Approach on the Spiral Wave Dynamics, BMES 2015 Annual Meeting). The results were generated using the Nash-Panfilov electromechanical model and therefore need to be confirmed in a realistic electromechanical model of cardiac tissue. Furthermore, developing methods for terminating spiral waves, by combining mechanical perturbation approach with other algorithms for detection and termination of spiral-waves, can be pursued in future studies. For instance, it has been shown that hypothermia affect the cardiac arrhythmias [149, 150]. Therefore, coupling heat with MEF to terminate spiral-waves can be the subject of a future work."

Treatment of cardiac fibrillation via MEF using the mechanical perturbation strategy can also be pursued. Using this strategy, we developed an algorithm for the termination of VF via MEF in a realistic electromechanical model of cardiac tissue, where the phase one Luo-Rudy model was used to represent the electrophysiological properties. The turbulence was suppressed by applying mechanical perturbation sequentially in subregions of tissue. Perturbing the mechanical properties in the localized region under control increases the magnitude of the depolarizing I_{sac} that excites all cells in the region under control and has the effect of stopping any propagation of the impulse and suppressing turbulence in this region. We presented our preliminary results in American Institute of Chemical Engineers annual meeting (Mechanical Perturbation Approach for Treating Cardiac Arrhythmias, AICHE 2018 Annual Meeting). On the other hand, electrical defibrillation, by means of providing strong electrical shocks to the heart to reset the heartbeat back to its normal beat, have remained the most reliable approach to terminate VF. However, the electrical treatment may cause damage to the heart due to delivery of high electrical current. Although the I_{sac}, which depends on stretch and voltage, delivered using the mechanical perturbation strategy is not high enough to cause any damage. However, this method needs further improvements so as to make it applicable in the treatment of VF.

Bibliography

[1] Leonid Makarov and Vera Komoliatova. Microvolt t-wave alternans during holter monitoring in children and adolescents. *ANN Noninvas Electro.*, 15(2):138–144, 2010.

[2] Sanjiv M. Narayan. T-wave alternans and human ventricular arrhythmias: What is the link? *J. Am. Coll. Cardiol.*, 49(3):347–349, 2007.

[3] George R. Mines. On dynamic equilibrium of the heart. *J. Physiol.*, 46(4-5):349–383, 1913.

[4] David S. Rosenbaum, Lance E. Jackson, Joseph M. Smith, Hasan Garan, Jeremy N. Ruskin, and Richard J. Cohen. Electrical alternans and vulnerability to ventricular arrhythmias. *New Engl. J. Med.*, 330(4):235–241, 1994.

[5] Donald M. Bers. *Excitation-Contraction Coupling and Cardiac Contractile Force*. Kluwer Academic, Dordrecht, Germany, 2001.

[6] M. J. Lab. Mechanoelectric feedback (transduction) in heart: concepts and implications. *Cardiovasc. Res.*, 32(1):3–14, 1996.

[7] P. Kohl, P. J. Hunter, and D. Noble. Stretch-induced changes in heart rate and rhythm: clinical observations, experiments and mathematical models. *Prog. Biophys. Mol. Biol.*, 71:91–138, 1999.

[8] P. Kohl and U. Ravens. Cardiac mechano-electric feedback: past, present, and prospect. *Prog. Biophys. Mol. Biol.*, 82(1-3):3–9, 2003.

[9] T. A. Quinn, P. Kohl, and U. Ravens. Cardiac mechano-electric coupling research: fifty years of progress and scientific innovation. *Prog. Biophys. Mol. Biol.*, 115(2-3):71–75, 2014.

[10] P. Kohl, A.D. Nesbitt, P.J. Cooper, and M. Lei. Sudden cardiac death by commotio cordis: Role of mechano-electric feedback. *Cardiovasc. Res.*, 50:280–289, 2001.

[11] Weihui Li, Peter Kohl, and Natalia Trayanova. Induction of ventricular arrhythmias following mechanical impact: A simulation study in 3d. *J. Mol. Histol.*, 35(7):679–686, 2004.

[12] Richard Klabunde. *Cardiovascular Physiology Concepts*. Lippincott Williams and Wilkins, New York, 2012.

[13] Peter Kohl, Frederick Sachs, and Michael R. Franz. *Cardiac Mechano-Electric Coupling and Arrhythmias*. Oxford University Press, Oxford, 2011.

[14] J. M. Pastore et al. Mechanism linking t-wave alternans to the genesis of cardiac fibrillation. *Circulation*, 99:1385–1394, 1999.

[15] Zhilin Qu, Alan Garfinkel, Peng-Sheng Chen, and James N. Weiss. Mechanisms of discordant alternans and induction of reentry in simulated cardiac tissue. *Circulation*, 102(14):1664–1670, 2000.

[16] Kevin Hall, David J Christini, Maurice Tremblay, James J Collins, Leon Glass, and Jacques Billette. Dynamic control of cardiac alternans. *Phys. Rev. Letts.*, 78(23):4518–4520, 1997.

[17] Wouter-Jan Rappel, Flavio Fenton, and Alain Karma. Spatiotemporal control of wave instabilities in cardiac tissue. *Phys. Rev. Letts.*, 83(2):456–459, 1999.

[18] David J Christini, Kenneth M Stein, Steven M Markowitz, Suneet Mittal, David J Slotwiner, Marc A Scheiner, Sei Iwai, and Bruce B Lerman. Nonlinear-dynamical arrhythmia control in humans. *Proc. Natl. Acad. Sci.*, 98(10):5827–5832, 2001.

[19] Blas Echebarria and Alain Karma. Spatiotemporal control of cardiac alternans. *Chaos*, 12(3):923–930, 2002.

[20] G. Martin Hall and Daniel J Gauthier. Experimental control of cardiac muscle alternans. *Phys. Rev. Letts.*, 88(19):198102–198105, 2002.

[21] David J Christini, Mark L Riccio, Calin A Culianu, Jeffrey J Fox, Alain Karma, and Robert F Gilmour Jr. Control of electrical alternans in canine cardiac purkinje fibers. *Phys. Rev. Lett.*, 96(10):104101, 2006.

[22] Kestutis Pyragas. Continuous control of chaos by self-controlling feedback. *Phys. Lett. A*, 170(6):421–428, 1992.

[23] Joshua E S Socolar, David W Sukow, and Daniel J Gauthier. Stabilizing unstable periodic orbits in fast dynamical systems. *Phys. Rev. E*, 50(4):3245–3248, 1994.

[24] Stevan Dubljevic, Shien-Fong Lin, and Panagiotis D Christofides. Studies on feedback control of cardiac alternans. *Comput. Chem. Eng.*, 32(9):2086–2098, 2008.

[25] Jeffrey J Fox, Mark L Riccio, Fei Hua, Eberhard Bodenschatz, and Robert F Gilmour Jr. Spatiotemporal transition to conduction block in canine ventricle. *Circ. Res.*, 90(3):289–296, 2002.

[26] Julius M Guccione, Kevin D Costa, and Andrew D McCulloch. Finite element stress analysis of left ventricular mechanics in the beating dog heart. *J. Biomech.*, 28(10):1167–1177, 1995.

[27] Peter J Hunter and Martyn P Nash. Computational mechanics of the heart: from tissue structure to ventricular function. *J. Elasticity*, 61(1-3):113–141, 2000.

[28] Taras P Usyk, Ian J LeGrice, and Andrew D McCulloch. Computational model of three-dimensional cardiac electromechanics. *Comput. Visual. Sci.*, 4:249–257, 2002.

[29] Roy C P Kerckhoffs, Peter H M Bovendeerd, Jiska C S Kotte, Frits W Prinzen, K Smits, and Theo Arts. Homogeneity of cardiac contraction despite physiological asynchrony of depolarization: a model study. *Ann. Biomed. Eng.*, 31(5):536–547, 2003.

[30] Martyn P. Nash and Alexander V. Panfilov. Electromechanical model of excitable tissue to study reentrant cardiac arrhythmias. *Prog. Biophys. Mol. Biol.*, 85(2-3):501–522, 2004.

[31] Alexander V Panfilov, Rik Huber Keldermann, and Martyn P Nash. Self-organized pacemakers in a coupled reaction-diffusion-mechanics system. *Phys. Rev. Lett*, 95(25):528104, 2005.

[32] David Nickerson, Nicolas Smith, and Peter Hunter. New developments in a strongly coupled cardiac electromechanical model. *Europace*, 7:S118–S127, 2005.

[33] Nico H L Kuijpers, Huub M M ten Eikelder, Peter H M Bovendeerd, Sander Verheule, Theo Arts, and Peter A J Hilbers. Mechanoelectric feedback leads to conduction slowing and block in acutely dilated atria: a modeling study of cardiac electromechanics. *Am. J. Physiol.*, 292(6):H2832–H2853, 2007.

[34] Steven A Niederer and Nicolas P Smith. An improved numerical method for strong coupling of excitation and contraction models in the heart. *Prog. Biophys. Mol. Biol.*, 96(1-3):90–111, 2008.

[35] Roy C P Kerckhoffs, Sarah N Healy, Taras P Usyk, and Andrew D McCulloch. Computational methods for cardiac electromechanics. *Proceedings of the IEEE*, 94(4):769–783, 2006.

[36] Natalia A Trayanova, Jason Constantino, and Viatcheslav Gurev. Electromechanical models of the ventricles. *Am. J. Physiol.*, 301(2):H279–H286, 2011.

[37] J. Keener and J. Sneyd. *Mathematical Physiology*. Springer-Verlag, New York, 1998.

[38] W. Ying and C.S. Henriquez. Adaptive mesh refinement and adaptive time integration for electrical wave propagation on the purkinje system. *BioMed Research International*, 2015:1–14, 2015.

[39] J. Southern, G.J. Gorman, M.D. Piggott, P.E. Farrell, M.O. Bernabeu, and J. Pitt-Francis. Simulating cardiac electrophysiology using anisotropic mesh adaptivity. *Journal of Computational Science*, 1(2):82 – 88, 2010.

[40] Youssef Belhamadia, André Fortin, and Yves Bourgault. On the performance of anisotropic mesh adaptation for scroll wave turbulence dynamics in reaction–diffusion systems. *Journal of Computational and Applied Mathematics*, 271:233–246, 2014.

[41] Youssef Belhamadia, André Fortin, and Yves Bourgault. Towards accurate numerical method for monodomain models using a realistic heart geometry. *Mathematical Biosciences*, 220(2):89–101, 2009.

[42] Youssef Belhamadia. A time-dependent adaptive remeshing for electrical waves of the heart. *IEEE Transactions on Biomedical Engineering*, 55(2):443–452, 2008.

[43] S. Linge, J. Sundnes, M. Hanslien, G.T. Lines, and A. Tveito. Numerical solution of the bidomain equations. *Phil. Trans. R. Soc. A*, 367(1895):1931–1950, 2009.

[44] H. J. Schroll, G.T. Lines, and A. Tveito. On the accuracy of operator splitting for the monodomain model of electrophysiology. *International Journal of Computer Mathematics*, 84(6):871–885, 2007.

[45] M. Potse, B. Dube, J. Richer, A. Vinet, and R. M. Gulrajani. A comparison of monodomain and bidomain reaction-diffusion models for action potential propagation in the human heart. *IEEE Transactions on Biomedical Engineering*, 53(12):2425–2435, 2006.

[46] Rubin R Aliev and Alexander V Panfilov. A simple two-variable model of cardiac excitation. *Chaos, Solitons and Fractals*, 7(3):293–301, 1996.

[47] A. L. Hodgkin and A. F. Huxley. A quantitative description of membrane current and its application to conduction and excitation in nerve. *J. Physiol.*, 177:500–544, 1952.

[48] J. J. Fox, J. L. McHarg, and R. F. Gilmour Jr. Ionic mechanism of electrical alternans. *Am. J. Physiol. Heart Circ. Physiol.*, 282(2):H516, 2002.

[49] C. Luo and Y. Rudy. A model of the ventricular cardiac action potential. depolarization, repolarization, and their interaction. *Circ. Res.*, 68:1501–1526, 1991.

[50] L. E. Malvern. *Introduction to the Mechanics of a Continuous Medium*. Prentice-Hall, Inc., Englewood Cliffs, NJ, 1969.

[51] Azzam Hazim, Youssef Belhamadia, and Stevan Dubljevic. Control of cardiac alternans in an electromechanical model of cardiac tissue. *Comput. Biol. Med.*, 63:108–117, 2015.

[52] D. Ambrosi and S. Pezzuto. Active stress vs. active strain in mechanobiology: Constitutive issues. *J. Elast.*, 107:199–212, 2012.

[53] K. D. Costa, J. W. Holmes, and A. D. McCulloch. Modeling cardiac mechanical properties in three dimensions. *Phil. Trans. R. Soc. Lond. Ser. A-Math. Phys. Eng. Sci.*, 359(1783):1233–1250, 2001.

[54] Azzam Hazim, Youssef Belhamadia, and Stevan Dubljevic. Mechanical perturbation control of cardiac alternans. *Phys. Rev. E*, 97:052407, May 2018.

[55] Ellen Kuhl and Serdar Göktepe. Electromechanics of the heart: a unified approach to the strongly coupled excitation–contraction problem. *Comput. Mech.*, 45(2):227–243, 2010.

[56] S. A. Niederer, P. J. Hunter, and N. P. Smith. A quantitative analysis of cardiac myocyte relaxation: a simulation study. *Biophys. J.*, 90:1697–1722, 2006.

[57] T. Zeng, G.C. Bett, and F. Sachs. Stretch-activated whole cell currents in adult rat cardiac myocytes. *Am. J. Physiol. Heart Circ. Physiol.*, 278(2):H548–H557, 2000.

[58] H. Hu and F. Sachs. Stretch-activated ion channels in the heart. *J. Mol. Cell. Cardiol.*, 29:1511–1523, 1997.

[59] Y. Zhang, J. Youm, S. Lee, S. Ryu, W. Ho, and Y. Earm. Stretch-activated and background nonselective cation channels in rat atrial myocytes. *J. Mol. Cell. Cardiol.*, 523:607–619, 2000.

[60] F. J. Vetter and A. D. McCulloch. Mechanoelectric feedback in a model of the passively inflated left ventricle. *Ann. Biomed. Eng.*, 29(5):414–426, 2001.

[61] N. Trayanova, W. Li, J. Eason, and P. Kohl. Effect of stretch activated channels on defibrillation efficacy. *Heart Rhythm*, 1:67–77, 2004.

[62] T. L. Riemer, E. A. Sobie, and L. Tung. Stretch-induced changes in arrhythmogenesis and excitability in experimentally based heart cell models. *Am J Physiol*, 275:H431–442, 1998.

[63] W. Li, V. Gurev, A. D. McCulloch, and N. A. Trayanova. The role of mechanoelectric feedback in vulnerability to electric shock. *Prog Biophys Mol Biol*, 97:461–478, 2008.

[64] W. Li, P. Kohl, and N. A. Trayanova. Myocardial ischemia lowers precordial thump efficacy: an inquiry into mechanisms using three-dimensional simulations. *Heart Rhythm*, 3(2):179–186, 2006.

[65] A. V. Panfilov, R. H. Keldermann, and M. P. Nash. Drift and breakup of spiral waves in reaction-diffusion-mechanics systems. *Proc Natl Acad Sci*, 104(19):7922–7926, 2007.

[66] T. L. Riemer and L. Tung. Stretch-induced excitation and action potential changes of single cardiac cells. *Prog Biophys Mol Biol*, 82:97–110, 2003.

[67] R. H. Keldermann, M. P. Nash, H. Gelderblom, V. Y. Wang, and A. V. Panfilov. Electromechanical wavebreak in a model of the human left ventricle. *Am. J. Physiol. Heart Circ. Physiol.*, 299:H134–H143, 2010.

[68] P. Kohl, K. Day, and D. Noble. Cellular mechanisms of cardiac mechano-electric feedback in a mathematical model. *Can. J. Cardiol.*, 14:111–119, 1998.

[69] J. B. Nolasco and Roger. W. Dahlen. A graphic method for the study of alternation in cardiac action potentials. *J. Appl. Physiol.*, 25(2):191–196, 1968.

[70] M. R. Guevara, G. Ward, A. Shrier, and L. Glass. Electrical alternans and period doubling bifurcations. *IEEE Comp. Cardiol.*, 562:167–170, 1984.

[71] Dante R. Chialvo, Robert F. Gilmour Jr, and Jose Jalife. Low dimensional chaos in cardiac tissue. *Nature*, 343:653–657, 1990.

[72] G. Martin Hall, Sonya Bahar, and Daniel J. Gauthier. Prevalence of rate-dependent behaviors in cardiac muscle. *Phys. Rev. Lett.*, 82:2995–2998, Apr 1999.

[73] S. G. Dilly and M. J. Lab. Electrophysiological alternans and restitution during acute regional ischaemia in myocardium of anaesthetized pig. *J. Physiol.*, 402:315–333, 1988.

[74] Y. Shiferaw, D. Sato, and A. Karma. Coupled dynamics of voltage and calcium in paced cardiac cells. *Phys. Rev. E*, 71:021903, 2005.

[75] Y. Shiferaw and A. Karma. Turing instability mediated by voltage and calcium diffusion in paced cardiac cells. *Proc. Natl. Acad. Sci. USA*, 103:5670–5675, 2006.

[76] D. Sato, Y. Shiferaw, A. Garfinkel, J. N. Weiss, Z. Qu, and A. Karma. Spatially discordant alternans in cardiac tissue : Role of calcium cycling. *Circ. Res.*, 99:520–527, 2006.

[77] Zhilin Qu, Yohannes Shiferaw, and James N. Weiss. Nonlinear dynamics of cardiac excitation-contraction coupling: An iterated map study. *Phys. Rev. E*, 75:011927, 2007.

[78] Dante R. Chialvo, D C Michaels, and Jose Jalife. Supernormal excitability as a mechanism of chaotic dynamics of activation in cardiac purkinje fibers. *Circ. Res.*, 66:525–545, 1990.

[79] N. F. Otani and Jr. R. F. Gilmour. Memory models for the electrical properties of local cardiac systems. *J. Theor. Biol*, 187:409–436, 1997.

[80] Jr. R. F. Gilmour, N. F. Otani, and M. A. Watanabe. Memory and complex dynamics in cardiac purkinje fibers. *Am. J. Physiol. Heart Circ. Physiol.*, 272:H1826, 1997.

[81] Flavio H. Fenton, Steven J. Evans, and Harold M. Hastings. Memory in an excitable medium: A mechanism for spiral wave breakup in the low-excitability limit. *Phys. Rev. Lett.*, 83:3964–3967, Nov 1999.

[82] MARI A. Watanabe and MARCUS L. Koller. Mathematical analysis of dynamics of cardiac memory and accommodation: theory and experiment. *Am. J. Physiol. Heart Circ. Physiol.*, 282:H1534, 2002.

[83] M. R. Franz, R. Cima, D. Wang, D. Profitt, and R. Kurz. Electrophysiological effects of myocardial stretch and mechanical determinants of stretch-activated arrhythmias. *Circulation*, 86(3):968–978, 1992.

[84] M. Zabel, B. S. Koller, F. Sachs, and M. R. Franz. Stretch-induced voltage changes in the isolated beating heart: importance of the timing of stretch and implications for stretch-activated ion channels. *Cardiovasc. Res.*, 32:120–130, 1996.

[85] F. Ravelli. Mechano-electric feedback and atrial fibrillation. *Prog. Biophys. Mol. Biol.*, 82(1-3):137–149, 2003.

[86] M. R. Franz and F. Bode. Mechano-electrical feedback underlying arrhythmias: the atrial fibrillation case. *Prog Biophys Mol Biol.*, 82(1-3):163–174, 2003.

[87] R. L. Chen, D. J. Penny, G. Greve, and M. J. Lab. Stretch-induced regional mecha-noelectric dispersion and arrhythmia in the right ventricle of anesthetized lambs. *Am. J. Physiol. Heart Circ. Physiol.*, 286(3):H1008–H1014, 2004.

[88] N. H. L. Kuijpers, R. H. Keldermann, H. M. M. ten Eikelder, T. Arts, and P. A. J. Hilbers. The role of the hyperpolarization-activated inward current if in arrhythmogenesis: a computer model study. *Am. J. Physiol.*, 53(8):1499–1511, 2006.

[89] K. Seo, M. Inagaki, S. Nishimura, I. Hidaka, M. Sugimachi, T. Hisada, and S. Sugiura. Structural heterogeneity in the ventricular wall plays a significant role in the initiation of stretch-induced arrhythmias in perfused rabbit right ventricular tissues and whole heart preparations. *Circ. Res.*, 106(1):176–184, 2010.

[90] S. C. Eijsbouts, M. Majidi, M. van Zandvoort, and M. A. Allessie. Effects of acute atrial dilation on heterogeneity in conduction in the isolated rabbit heart. *J Cardiovasc Electrophysiol.*, 14(3):269–278, 2003.

[91] Y. Hu, V. Gurev, J. Constantino, J. D. Bayer, and N. A. Trayanova. Effects of mechano-electric feedback on scroll wave stability in human ventricular fibrillation. *PLoS One*, 8(4):e60287, 2013.

[92] U. Ravens. Mechano-electric feedback and arrhythmias. *Prog. Biophys. Mol. Biol.*, 82(1-3):255–266, 2003.

[93] T. A. Quinn. The importance of non-uniformities in mechano-electric coupling for ventricular arrhythmias. *J Interv Card Electrophysiol*, 39(1):25–35, 2014.

[94] I. R. Cantalapiedra, A. Peñaranda, L. Mont, J. Brugada, and B. Echebarria B. Reexcitation mechanisms in epicardial tissue: Role of I_{to} density heterogeneities and i_{Na} inactivation kinetics. *J. Theor. Biol.*, 259(4):850–859, 2009.

[95] Inma R. Cantalapiedra, Angelina Peñaranda, Blas Echebarria, and Jean Bragard. Phase-2 reentry in cardiac tissue: Role of the slow calcium pulse. *Phys. Rev. E*, 82:011907, Jul 2010.

[96] T. Opthof, V. M. F. Meijborg, C. N. W. Belterman, and R. Coronel. Synchronization of repolarization by mechano-electrical coupling in the porcine heart. *Cardiovasc. Res.*, 108(1):181–187, 2015.

[97] Felicia Yapari, Dipen Deshpande, Youssef Belhamadia, and Stevan Dubljevic. Control of cardiac alternans by mechanical and electrical feedback. *Phys. Rev. E*, 90:012706, 2014.

[98] A. V. Panfilov, R. H. Keldermann, and M. P. Nash. Self-organized pacemakers in a coupled reaction-diffusion-mechanics system. *Phys. Rev. Lett.*, 95:258104, Dec 2005.

[99] P. Kohl, C. Bollensdorff, and A. Garny. Effects of mechanosensitive ion channels on ventricular electrophysiology: Experimental and theoretical models. *Exp. Physiol.*, 91(2):307–321, 2006.

[100] E. White, J-Y. Le. Guennec, J. M. Nigretto, F. Gannier, J. A. Argibay, and D. Garnier. The effects of increasing cell length on auxotonic contractions; membrane potential and intracellular calcium transients in single guinea-pig ventricular myocytes. *Exp. Physiol.*, 78:65–78, 1993.

[101] D. Kelly, L. Mackenzie, P. Hunter, B. Smaill, and D.A. Saint. Gene expression of stretch-activated channels and mechanoelectric feedback in the heart. *Clin. Exp. Pharmacol. Physiol.*, 33(7):642–648, 2006.

[102] A. Garny and P. Kohl. Mechanical induction of arrhythmias during ventricular repolarization: Modeling cellular mechanisms and their interaction in two dimensions. *Ann. N. Y. Acad. Sci.*, 1015(1):133–143, 2004.

[103] S. M. Horner, D. J. Dick, C. F. Murphy, and M. J. Lab. Cycle length dependence of the electrophysiological effects of increased load on the myocardium. *Circulation*, 94:1131–1136, 1996.

[104] P. Taggart and M. Lab. Cardiac mechano-electric feedback and electrical restitution in humans. *Prog. Biophys. Mol. Biol.*, 97:452–460, 2008.

[105] Zhilin QU, James. N. Weiss, and Alan Garfinkel. Cardiac electrical restitution properties and stability of reentrant spiral waves: a simulation study. *Am. J. Physiol. Heart Circ. Physiol.*, 276(1):H269–283, 1999.

[106] Fagen Xie, Zhilin Qu, Yang Junzhong, Baher Ali, James. N. Weiss, and Alan Garfinkel. A simulation study of the effects of cardiac anatomy in ventricular fibrillation. *J. Clin. Invest.*, 113(5):686–693, 2004.

[107] K. Skouibine, N. Trayanova, and P. Moore. A numerically efficient model for simulation of defibrillation in an active bidomain sheet of myocardium. *Math. Biosci.*, 166:85–100, 2000.

[108] T. G. McNary, K. Sohn, B. Taccardi, and F. B. Sachse. Experimental and computational studies of strain-conduction velocity relationships in cardiac tissue. *Prog. Biophys. Mol. Biol.*, 97(2-3):383–400, 2008.

[109] F. G. Akar, K. R. Laurita, and D. S. Rosenbaum. Cellular basis for dispersion of repolarization underlying reentrant arrhythmias. *J. Electrocardiology*, 33(8):23–31, 2000.

[110] C. S. Kuo, K. Munakata, C. P. Reddy, and B. Surawicz. Characteristics and possible mechanism of ventricular arrhythmia dependent on the dispersion of action potential durations. *Circulation*, 67:1356–1367, 1983.

[111] Michael C.Giudici and Michael P.Savage. Transient pulsus alternans during acute myocardial ischemia and its resolution following beta-adrenergic blockade. *Am Heart J.*, 119(4):960–962, 1990.

[112] C. R. Kroll and L. S. Gettes. T wave alternans and torsades de pointes after the use of intravenous pentamidine. *J Cardiovasc Electrophysiol.*, 13(9):960–962, 2003.

[113] M. R. Boyett and Jewell B. R. Jewell. A study of the factors responsible for rate-dependent shortening of the action potential in mammalian ventricular muscle. *J Physiol.*, 285:359–380, 1978.

[114] Marcus L. Koller, Mark L. Riccio, and Robert F. Gilmour Jr. Dynamic restitution of action potential duration during electrical alternans and ventricular fibrillation. *Am J Physiol Heart Circ Physiol*, 275:H1635–H1642, 1998.

[115] Azzam Hazim, Youssef Belhamadia, and Stevan Dubljevic. Effects of mechano-electrical feedback on the onset of alternans: A computational study. *Chaos: An Interdisciplinary Journal of Nonlinear Science*, 29(6):063126, 2019.

[116] D. S. Rubenstein and S. L. Lipsius. Premature beats elicit a phase reversal of mechanoelectrical alternans in cat ventricular myocytes: a possible mechanism for reentrant arrhythmias. *Circulation*, 91:201–214, 1995.

[117] M.A. Watanabe, F.H. Fenton, S.J. Evans, H.M. Hastings, and A. Karma. Mechanisms of discordant alternans. *J. Cardiovasc. Electrophys.*, 12(2):196–206, 2001.

[118] Gary Tse, Sheung Ting Wong, Vivian Tse, Yee Ting Lee, Hiu Yu Lin, and Jie Ming Yeo. Cardiac dynamics: Alternans and arrhythmogenesis. *J Arrhythm.*, 32(5):411–417, 2016.

[119] J. L. Bierfeld, V. Rodriguez-Viera, J. M. Aranda, A. J. Castellanos, R. Lazzara, and B. Befeler. Terminating ventricular fibrillation by chest thump. *Angiology*, 30:703–707, 1979.

[120] Elizabeth M. Cherry and Flavio H. Fenton. Effects of boundaries and geometry on the spatial distribution of action potential duration in cardiac tissue. *J Theor Biol.*, 285(1):164–176, 2011.

[121] Allen Kelly, Iffath A. Ghouri, Ole J. Kemi, Martin J. Bishop, Olivier Bernus, Flavio H. Fenton, Rachel C. Myles, Francis L. Burton, , and Godfrey L. Smith. Subepicardial action potential characteristics are a function of depth and activation sequence in isolated rabbit hearts. *Circ Arrhythm Electrophysiol*, 6:809–817, 2013.

[122] Leonid Makarov and Vera Komoliatova. Microvolt t-wave alternans during holter monitoring in children and adolescents. *Ann.Noninvasive Electrocardiol.*, 15(2):138–144, 2010.

[123] Marcus L Koller, Mark L Riccio, and Robert F Gilmour Jr. Dynamic restitution of action potential duration during electrical alternans and ventricular fibrillation. *Am. J. Physiol.*, 275(5):H1635–H1642, 1998.

[124] Max J Lab. Contraction-excitation feedback in myocardium. physiological basis and clinical relevance. *Circ. Res.*, 50(6):757–766, 1982.

[125] Irina Kiseleva, Andre Kamkin, Kay-Dietrich Wagner, Heinz Theres, Axel Ladhoff, Holger Scholz, Joachim Günther, and Max J Lab. Mechano-electric feedback after left ventricular infarction in rats. *Cardiovasc. Res.*, 45(2):370–378, 2000.

[126] Peter Kohl, Alex D Nesbitt, Patricia J Cooper, and Ming Lei. Sudden cardiac death by commotio cordis: Role of mechano-electric feedback. *Cardiovasc. Res.*, 50(2):280–289, 2001.

[127] Christopher Madias, Maron Barry J, Jonathan Weinstock, NA 3rd Estes, and Mark S Link. Commotio cordis–sudden cardiac death with chest wall impact. *J. Cardiovasc. Electrophysiol.*, 18(1):115–122, 2007.

[128] Weihui Li, Peter Kohl, and Natalia Trayanova. Induction of ventricular arrhythmias following mechanical impact: a simulation study in 3d. *J. Mol. Histol.*, 35(7):679–686, 2004.

[129] Weihui Li, Peter Kohl, and Natalia Trayanova. Myocardial ischemia lowers precordial thump efficacy: An inquiry into mechanisms using three-dimensional simulations. *Heart Rhythm*, 3(2):179–186, 2006.

[130] Junuthula N Reddy. *An Introduction to Continuum Mechanics*. Cambridge University Press, New York, 2008.

[131] Rik Huber Keldermann, Martyn P Nash, Hanneke Gelderblom, Vicky Y Wang, and Alexander V Panfilov. Electromechanical wavebreak in a model of the human left ventricle. *Am. J. Physiol.*, 299(1):H134–H143, 2010.

[132] Enrique Alvarez-Lacalle and Blas Echebarria. Global coupling in excitable media provides a simplified description of mechanoelectrical feedback in cardiac tissue. *Phys. Rev. E*, 79:031921, 2009.

[133] Gerhard A HolzapfeL. *Nonlinear Solid Mechanics: A Continuum Approach for Engineering*. John Wiley & Sons, Baffins Lane, Chichester, England, 2000.

[134] L. Xu, S. R. Gutbrod, A. P. Bonifas, Y. Su, M. S. Sulkin, N. Lu, H. J. Chung, K. I. Jang, Z. Liu, M. Ying, C. Lu, R. C. Webb, J. S. Kim, J. I. Laughner, H. Cheng, Y. Liu, A. Ameen, J. W. Jeong, G. T. Kim, Y. Huang, I. R. Efimov, and J. A. Rogers. 3d multifunctional integumentary membranes for spatiotemporal cardiac measurements and stimulation across the entire epicardium. *Nat. Commun.*, 5:3329, 2014.

[135] Shaphan Rees Jernigan, Gregory D Buckner, Jeffrey W Eischen, and Denis R Cormier. Finite element modeling of the left atrium to facilitate the design of an endoscopic atrial retractor. *J Biomech Eng.*, 129(6):825–837, 2007.

[136] Kumbakonam R Rajagopal. On the nonlinear elastic response of bodies in the small strain range. *Acta Mechanica*, 255(6):1545–1553, 2014.

[137] Alexander V Panfilov. Spiral breakup as a model of ventricular fibrillation. *Chaos*, 8(1):57–64, 1998.

[138] Alexander V Panfilov and James P Keener. Re-entry in an anatomical model of the heart. *Chaos, Solitons and Fractals*, 5(3-5):681–689, 1995.

[139] A. Gizzi, E. M. Cherry, R. F. Gilmour Jr., S. Luther, S. Filippi, and F. H. Fenton. Effects of pacing site and stimulation history on alternans dynamics and the development of complex spatiotemporal patterns in cardiac tissue. *Front. Physiol.*, 4:71, 2013.

[140] Blas Echebarria and Alain Karma. Spatiotemporal control of cardiac alternans. *Chaos*, 12:923, 2002.

[141] Y. Shiferaw, D. Sato, and A. Karma. Coupled dynamics of voltage and calcium in paced cardiac cells. *Phys. Rev. E*, 71:021903, 2005.

[142] C. Cherubinia, S. Filippia, A. Gizzia, and R. Ruiz-Baierc. A note on stress-driven anisotropic diffusion and its role in active deformable media. *J. Theor. Biol.*, 430:221–228, 2017.

[143] HGüsGün Dal, Serdar Göktepe, Michael Kaliske, and Ellen Kuhl. A fully implicit finite element method for bidomain models of cardiac electromechanics. *Comput. Meth. Appl. Mech. Eng.*, 253:323–336, 2013.

[144] R. H. Keldermann, M. P. Nash, and A. V. Panfilov. Modeling cardiac mechano-electrical feedback using reaction-diffusion-mechanics systems. *Physica D*, 238:1000–1007, 2009.

[145] Stanley Rush and Hugh Larsen. A practical algorithm for solving dynamic membrane equations. *IEEE Trans. Biomed. Eng.*, 25:389–392, 1978.

[146] E. R. Pfeiffer, J. R. Tangney, J. H. Omens, and A. D. McCulloch. Biomechanics of cardiac electromechanical coupling and mechanoelectric feedback. *J. Biomech. Eng.*, 136:021007, 2014.

[147] J. P. Whiteley, M. J. Bishop, and D. J. Gavaghan. Soft tissue modelling of cardiac fibres for use in coupled mechano-electric simulations. *Bull. Math. Biol.*, 69:2199–2225, 2007.

[148] F. Sahli Costabal, F. A. Concha, D. E. Hurtado, and E. Kuhl. The importance of mechano-electrical feedback and inertia in cardiac electromechanics. *Comput. Meth. Appl. Mech. Eng.*, 320:352–368, 2017.

[149] D. Bini, C. Cherubini, and S. Filippi. On vortices heating biological excitable media. *Chaos, Solitons & Fractals*, 42(4):2057 – 2066, 2009.

[150] Youssef Belhamadia and Justin Grenier. Modeling and simulation of hypothermia effects on cardiac electrical dynamics. *PloS one*, 14(5):1–23, 2019.

Supplementary Materials

Effects of mechano-electrical feedback on the onset of alternans: a computational study

NHS model

The ordinary differential equations (ODEs), vector of state variables ($\mathbf{w}$), and prescribed functions ($\mathbf{g}$ and h) of the NHS model described by Niederer et al. (2006) are given in (a), (b), and (c), respectively.

–ODEs:

$$\frac{d[\mathrm{Ca}^{2+}]_{\mathrm{Trpn}}}{dt} = k_{\mathrm{on}}[\mathrm{Ca}^{2+}]_{\mathrm{i}}([\mathrm{Ca}^{2+}]_{\mathrm{TrpnMax}} - [\mathrm{Ca}^{2+}]_{\mathrm{Trpn}}) - k_{\mathrm{refoff}}\left(1 - \frac{T_a}{\gamma\, T_{\mathrm{ref}}}\right)[\mathrm{Ca}^{2+}]_{\mathrm{Trpn}}, \tag{1.S}$$

$$\frac{dz}{dt} = \alpha_0 \left(\frac{[\mathrm{Ca}^{2+}]_{\mathrm{Trpn}}}{[\mathrm{Ca}^{2+}]_{\mathrm{Trpn50}}}\right)^n (1-z) - \alpha_{r_1} z - \alpha_{r_2}\, \frac{z^{n_r}}{z^{n_r} + K_z^{n_r}}, \tag{2.S}$$

$$\frac{dQ_1}{dt} = A_1 \frac{d\lambda}{dt} - \alpha_1\, Q_1, \tag{3.S}$$

$$\frac{dQ_2}{dt} = A_2 \frac{d\lambda}{dt} - \alpha_2\, Q_2, \tag{4.S}$$

$$\frac{dQ_3}{dt} = A_3 \frac{d\lambda}{dt} - \alpha_3\, Q_3, \tag{5.S}$$

$$T_a = \begin{cases} T_0 \dfrac{1 + (2+a)\, Q}{1+Q} & Q > 0, \\ T_0 \dfrac{1 + a\, Q}{1-Q} & Q \le 0, \end{cases} \tag{6.S}$$

$$[\mathrm{Ca}^{2+}]_{\mathrm{Trpn50}} = \frac{[\mathrm{Ca}^{2+}]_{\mathrm{TrpnMax}}[\mathrm{Ca}^{2+}]_{\mathrm{50ref}}(1+\beta_1(\lambda-1))}{[\mathrm{Ca}^{2+}]_{\mathrm{50ref}} 1 + \beta_1(\lambda-1)) + \dfrac{k_{\mathrm{refoff}}}{k_{\mathrm{on}}}\left(1 - \dfrac{1+\beta_0(\lambda-1)}{2\gamma}\right)},$$

$$K_1 = \frac{\alpha_{r_2} z_p^{n_r-1} n_r K_z^{n_r}}{(z_p^{n_r} + K_z^{n_r})^2},$$

$$K_2 = \frac{\alpha_{r_2} z_p^{n_r}}{z_p^{n_r} + K_z^{n_r}}\left(1 - \frac{n_r K_z^{n_r}}{z_p^{n_r} + K_z^{n_r}}\right),$$

$$z_{max} = \frac{\alpha_0 - K_2[\mathrm{Ca}^{2+}]_{\mathrm{Trpn50}}}{\alpha_0 + (\alpha_{r_1} + K_1)[\mathrm{Ca}^{2+}]_{\mathrm{Trpn50}}},$$

$$T_0 = \frac{z T_{\mathrm{ref}}(1+\beta_0(\lambda-1))}{z_{max}},$$

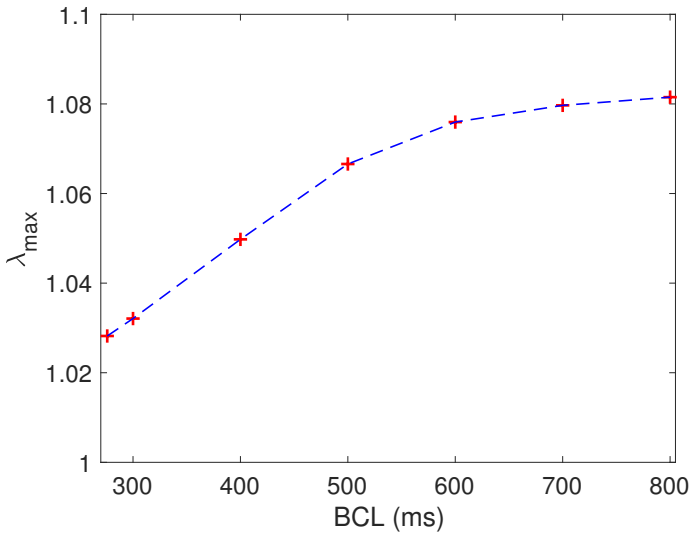

Figure S.1: Plot showing the variation of the maximal values of stretch developed in the cable versus the corresponding values of BCL (red plus sign). A 7 cm cable of cardiac cells is paced at the boundary with BCL = 276 ms until a steady state is reached. This procedure was repeated for different BCLs starting at BCL = 300 ms and increasing each time by 100 ms till BCL = 800 ms.

$$Q = Q_1 + Q_2 + Q_3,$$

The reader is referred to Niederer et al. (2006) for the parameters values and the initial conditions of the system (1.S-5.S).

–$\mathbf{w} = ([\mathrm{Ca}^{2+}]_{\mathrm{Trpn}},\ z,\ Q_1,\ Q_2,\ Q_3)$, where $[\mathrm{Ca}^{2+}]_{\mathrm{Trpn}}$, z, Q_1, Q_2, and Q_3 are the state variables of the system (1.S-5.S).

–$\mathbf{g} = (g_1,\ g_2,\ g_3,\ g_4,\ g_5)$, where g_1, g_2, g_3, g_4, and g_5 are the right-hand sides of Eqs. (1.S) through (5.S), and h is the right-hand side of Eq. (6.S)

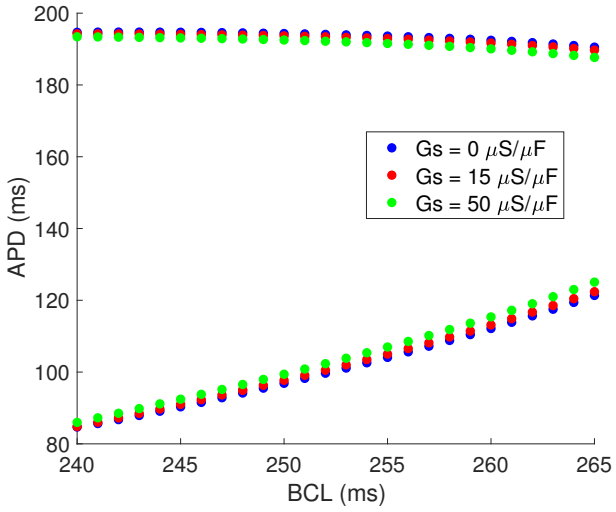

Figure S.2: Bifurcation diagrams showing APD versus BCL for different values of G_s of LR1NHS model (left panel), and a zoomed-in version of it (right panel). The cell in the middle of a 7 cm cable is paced for different BCLs, starting at BCL = 350 ms and decreasing by 1 ms, after a steady state is reached for each BCL, until BCL is equal to BCL = 240 ms. This procedure was repeated for three values of G_s and the simulation values of the APD at steady state are plotted versus BCL when it varies between 240 ms and 265 ms. APD at 90% repolarization was adopted as a measure of APD.

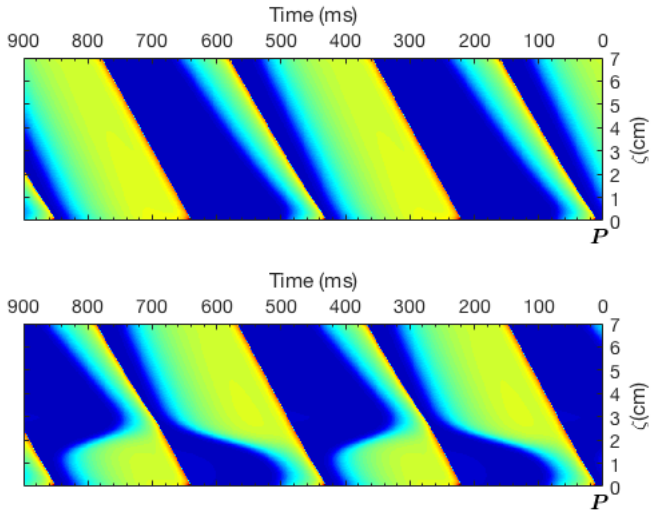

Figure S.3: Spatiotemporal evolution of V in LR1NHS model with $G_s = 0$ μS/μF (top), and with $G_s = 51$ μS/μF and $E_s =$ -20 mV (bottom), when a 7 cm cable of cardiac cells is paced at the boundary (he first five cells, that are close to $\boldsymbol{P}$, were paced) at BCL = 210 ms, and a steady state is reached.

Appendix A

Approximation of the extension ratio

In one dimension, the extension ratio in the direction of the fiber is calculated from the soft tissue mechanics model, and is given by [51, 67]

$$\lambda = \sqrt{C_{11}} = F(X) = 1 + \frac{\partial u(X)}{\partial X} \tag{7.S}$$

If we assume that the maximal stretch of cells, from the resting position, is 5%, we may approximate the inverse of $F(X)$ as

$$F(X)^{-1} = \left(1 + \frac{\partial u(X)}{\partial X}\right)^{-1} \approx 1 - \frac{\partial u(X)}{\partial X} \tag{8.S}$$

The elastic equation (5.4) can be rewritten as

$$\tilde{c}\,\frac{\partial\left(1 + \dfrac{\partial u(X)}{\partial X}\right)}{\partial X} + \frac{\partial}{\partial X}\left(\frac{T_a(X)}{1 + \dfrac{\partial u(X)}{\partial X}}\right) = 0 \tag{9.S}$$

By integrating Eq. (9.S), we obtain

$$\tilde{c}\left(1 + \frac{\partial u(X)}{\partial X}\right) + \frac{T_a(X)}{1 + \dfrac{\partial u(X)}{\partial X}} = C \tag{10.S}$$

The integration constant C is determined by applying boundary conditions. Since a 1D cable fixed at both ends is considered, and thus $\partial u(X)/\partial X = 0$ ($F(X) = 1$) at the boundaries, we have $C = T_b + \tilde{c}$, where T_b is the active tension at the boundary, which satisfies the following condition.

$$\int_0^L F(X)dX = L \tag{11.S}$$

Replacing C and the approximation of $F(X)^{-1}$ (Eq. (8.S)) by their values in Eq. (10.S) and solving for $\partial u(X)/\partial X$, we obtain

$$\frac{\partial u(X)}{\partial X} \approx \frac{T_b - T_a(X)}{\tilde{c} - T_a(X)} \tag{12.S}$$

Replacing $\partial u(X)/\partial X$ by its value in Eq. (7.S), we obtain

$$F(X) \approx 1 + \frac{T_b - T_a(X)}{\tilde{c} - T_a(X)},$$

$$\text{with } T_b \approx \frac{\int_0^L \frac{T_a(X)}{\tilde{c} - T_a(X)} dX}{\int_0^L \frac{1}{\tilde{c} - T_a(X)} dX}, \tag{13.S}$$

where T_b is determined by replacing $F(X)$ (Eq. (13.S)) by its value in Eq. (11.S). Therefore, when $1 < \lambda <= 1.05$, an approximation of λ, given in Eqs. (7.S) and (13.S), is directly related to T_a, and thus I_{SAC}, which is not zero only when the cell is stretched (i.e., when $\lambda > 1$), becomes a function of V and T_a. If we assume that the maximal stretch is 10% (i.e., $\lambda <= 1.1$), the same approximation of λ (Eqs. (7.S) and (13.S)) can be used to calculate I_{SAC}, since the maximum error calculated in the case of Model 2, between the exact instantaneous stretch, found by solving the elastic equation (5.4), and the approximate stretch obtained from Eq. (13.S), during one cycle, is less than 1%. This work is not concerned with the complex dynamics of either V or T_a at the cellular level, which would require a more rigorous computation of I_{sac}.

Jacobian of the 2D map

The heart beat-to-beat dynamics using a 2D discrete map between the APD and the ATD is given as

$$\begin{aligned} APD_n &= F_1(APD_{n-1}, ATD_n), \\ ATD_n &= F_2(APD_{n-1}, ATD_{n-1}) \end{aligned} \tag{14.S}$$

Let $F = [F_1, F_2]^T$, and $X_n = [x_n, y_n]^T = [APD_n, ATD_n]^T$, then the map (Eq. (14.S)) can be written in the matrix form as

$$X_n = F(X_{n-1}) \tag{15.S}$$

At the period-1 fixed point $X_* = [APD_*, ATD_*]^T$, we have $X_n = F(X_{n-1}) = X_{n-1} = X_* = F(X_*)$. Let $\delta X_n = [\delta APD_{n-1}, \delta ATD_{n-1}]^T$ be a small displacement from the point X_*, we can then write

$$X_* + \delta X_n = F(X_* + \delta X_{n-1}) \tag{16.S}$$

Using the Taylor expansion, we can linearize the system of coupled maps around the point X_* as follows

$$F(X_* + \delta X_{n-1}) \approx F(X_*) + J\ \delta X_{n-1}, \tag{17.S}$$

where

$$J = \begin{bmatrix} \dfrac{\partial F_1}{\partial x_{n-1}} & \dfrac{\partial F_1}{\partial y_{n-1}} \\ \dfrac{\partial F_2}{\partial x_{n-1}} & \dfrac{\partial F_2}{\partial y_{n-1}} \end{bmatrix}, \tag{18.S}$$

where $J_{11} = \dfrac{\partial F_1}{\partial APD_{n-1}}$, $J_{12} = \dfrac{\partial F_1}{\partial ATD_{n-1}}$, $J_{21} = \dfrac{\partial F_2}{\partial APD_{n-1}}$, and $J_{22} = \dfrac{\partial F_2}{\partial ATD_{n-1}}$ are the elements of the Jacobian J evaluated at the fixed point (APD_*, ATD_*) of the map. From Eqs. (16.S) and (17.S) we can write

$$\delta X_n \approx J\ \delta X_{n-1}. \tag{19.S}$$